LONG-TERM ENERGY YIELD ESTIMATION OF A SOLAR PHOTOVOLTAIC POWER PLANT IN METU NCC

A THESIS SUBMITTED TO
THE BOARD OF GRADUATE PROGRAMS
OF
MIDDLE EAST TECHNICAL UNIVERSITY, NORTHERN CYPRUS CAMPUS

BY

DENİZ GÖREN

IN PARTIAL FULFILLMENT OF THE REQUIREMENTS
FOR
THE DEGREE OF MASTER OF SCIENCE
IN SUSTAINABLE ENVIRONMENT AND ENERGY SYSTEMS PROGRAM

JANUARY 2021

Approval of the Board of Graduate Programs

Prof. Dr. Oğuz Solyalı

Chairperson

I certify that this thesis satisfies all the requirements as a thesis for the degree of Master of Science

Assoc. Prof. Dr.

Ceren İnce Derogar

Program Coordinator

This is to certify that we have read this thesis and that in our opinion it is fully adequate, in scope and quality, as a thesis for the degree of Master of Science.

Assoc. Prof. Dr.	Assoc. Prof. Dr.
Onur Taylan	Murat Fahrioğlu
Co-Supervisor	Supervisor

Examining Committee Members

Asst. Prof. Dr. Neyre Tekbıyık Ersoy	Cyprus International University, Energy Systems Engineering	
Assoc. Prof. Dr. Murat Fahrioğlu	METU NCC, Electrical and Electronics Engineering	
Asst. Prof. Dr. Bertuğ Akıntuğ	METU NCC, Civil Engineering	

I hereby declare that all information in this document has been obtained and presented in accordance with academic rules and ethical conduct. I also declare that, as required by these rules and conduct, I have fully cited and referenced all material and results that are not original to this work.

Name, Last name : Deniz, Gören

Signature :

ABSTRACT

LONG-TERM ENERGY YIELD ESTIMATION OF A SOLAR PHOTOVOLTAIC POWER PLANT IN METU NCC

Gören, Deniz
Master of Science, Sustainable Environment and Energy Systems Program
Supervisor: Assoc. Prof. Dr. Murat Fahrioğlu
Co-Supervisor: Assoc. Prof. Dr. Onur Taylan

January 2021, 99 pages

Installing large scales of solar energy introduces some financial risks for the investors since the solar resource is variable. Thus, a long-term energy yield estimation is needed to see the variability of the solar resource. This study aims to see the relation between long-term trends of global horizontal irradiation (GHI) with the energy yield and the levelized cost of electricity (LCOE). Probability of exceedance (POE) values were found to assess the bankability of installing a solar PV power plant. Different datasets, such as typical meteorological year (TMY), satellite-based and ground-measured data, were used. Quality assessment was done to check the accuracy of ground-measured data using quality control tests. Erroneous GHI data was estimated using the Erbs model. Global tilted irradiation (GTI) was also estimated using the isotropic sky-diffuse model, and it was compared with measured GTI. The interannual variability of GHI was found as 5.94% and 2.21% for ground-measured and satellite-based data, respectively. The comparison of TMY and P50 values showed that TMY datasets underpredicted the annual GHI by about 5.15% and the energy yield by about 6.83% on average. When Normal distribution was compared with the empirical method, the P50 value was underpredicted by 0.93% for energy yield, whereas, Normal cumulative distribution function (CDF) overpredicted P90 value than the empirical CDF 3.93%. Doing stochastic

simulations resulted in the highest POE values: P50 and P90 values increased by 3.30% and 6.10%, respectively, compared to the empirical method. Moreover, while the range of energy yield increased to about 1500-2000 kWh/kWp, LCOE range increased to 0.05-0.19 $/kWh in stochastic simulations. As the overall uncertainty of energy yield was found as about 7.08%, it can be further reduced by searching for other sources of error such as temperature and soiling.

Keywords: Energy Yield, Interannual Variability, Probability of Exceedance, Uncertainty Analysis, Levelized Cost of Electricity

ÖZ

ODTÜ KKK'DEKİ GÜNEŞ FOTOVOLTAİK SANTRALİNİN UZUN VADELİ ENERJİ VERİMİ TAHMİNİ

Gören, Deniz
Yüksek Lisans, Sürdürülebilir Çevre ve Enerji Sistemleri
Tez Yöneticisi: Doç. Dr. Murat Fahrioğlu
Ortak Tez Yöneticisi: Doç. Dr. Onur Taylan

Ocak 2021, 99 sayfa

Güneş kaynağı değişken olduğundan büyük ölçekli güneş enerjisi kurulumu yatırımcılar için bazı finansal riskler ortaya çıkarmaktadır. Bu nedenle, güneş kaynağının değişkenliğini görmek için uzun vadeli bir enerji verimi tahminine ihtiyaç vardır. Bu çalışmanın amacı, küresel yatay ışınımın (GHI) uzun vadeli eğilimleri ile enerji verimi ve seviyelendirilmiş elektrik maliyeti (LCOE) arasındaki ilişkiyi görmektir. Bu çalışma kapsamında bir PV temelli enerji santrali kurmanın güvenilirliğini görmek için aşılma olasılığı (POE) değerleri bulunmuştur. Tipik meteorolojik yıl (TMY), uydu tabanlı ve yerden ölçülen veriler gibi farklı veri kümeleri kullanılmış ve kalite kontrol testleri kullanılarak zeminde ölçülen verilerin doğruluğunu kontrol etmek için kalite değerlendirmesi yapılmıştır. Hatalı GHI verileri, Erbs modeli kullanılarak ve küresel eğimli ışınım (GTI) da izotropik gökyüzü difüzör modeli kullanılarak tahmin edilmiştir. Bu değerler, ölçülen GTI ile karşılaştırılmıştır. GHI'nin yıllar arası değişkenliği yer ölçülü ve uydu tabanlı veriler için sırasıyla %5.94 ve %2.21 olarak bulunmuştur. TMY ve P50 değerlerinin karşılaştırılmasına göre, TMY veri setlerinin yıllık GHI'yi yaklaşık %5.15, enerji verimini ise ortalama %6.83 oranında düşük öngördüğü bulunmuştur. Normal dağılım ampirik yöntemle karşılaştırıldığında P50 değeri enerji verimi için %0.93 ile

düşük tahmin edilirken, Normal kümülatif dağılım fonksiyonu (CDF) P90 değerini ampirik CDF'ye göre %3.93 oranında fazla tahmin edilmiştir. Stokastik benzetimlerde bulunan P50 ve P90 değerleri, ampirik yönteme göre sırasıyla %3.30 ve %6.10 fazla çıkmıştır. Ayrıca, stokastik benzetimlerde kurulu güç başına üretilen enerji aralığı yaklaşık 1500-2000 kWh/kWp'ye yükseldiğinde LCOE aralığı 0.05-0.19 $/kWh'ye yükselmiştir. Enerji üretiminin genel belirsizliği yaklaşık %7.08 olarak bulunmuştur, fakat sıcaklık ve kirlenme gibi diğer hata kaynakları araştırılarak bu belirsizlik daha da azaltılabilecektir.

Anahtar Kelimeler: Enerji Verimi, Yıllar-arası Değişkenlik, Aşma Olasılığı, Belirsizlik Analizi, Seviyelendirilmiş Elektrik Maliyeti

To My Lovely Nephews, Sarp and Kaya

ACKNOWLEDGMENTS

I would like to express my deepest gratitude to Assoc. Prof. Dr. Onur Taylan, who has been my advisor throughout my thesis studies. His continuous guidance and valuable knowledge served as the driving force behind this thesis. I would also like to thank Assoc. Prof. Dr. Murat Fahrioğlu for his supports and I was privileged to take his courses during masters. Besides, I would like to express my sincere thanks to Asst. Prof. Dr. Anna Prach and Asst. Prof. Dr. Ceren İnce Derogar for giving me the chance of becoming a teaching assistant at the Aerospace Engineering Program. Furthermore, I would like to thank my counselor Nazan Tekgüç, for giving me the psychological support during the pandemic at METU NCC.

Indeed, I would like to thank my family for their endless supports – my beloved sister Güneş, mom, dad, grandma and grandpa. They always had absolute confidence in me and cared for me. I would also like to thank my love, Enes, who was always by my side to get over the difficulties in life and for believing in me. My biggest thank goes to my nephews – Sarp and Kaya – who gave me the biggest motivation to leave a sustainable world to future generations, and this thesis is dedicated to them.

Finally, I would like to thank my special friends in METU NCC. I feel lucky to meet and form a strong friendship with Sana Khan, Mahnoor Yaqoob and Gözde Taylan. I would also like to thank my friends for sharing good times and having fun in Cyprus: Arman, Aslıhan, Ayça, Erfan, Haroon, Irmak, Melis, Nazlıcan, Nilay, Safa, Shima and Yashfeen. A very special thanks goes to my old friends, who have supported me unconditionally; Aybeniz, İpek and Sıla. This study would not have been possible without them.

TABLE OF CONTENTS

ABSTRACT v

ÖZ vii

ACKNOWLEDGMENTS x

TABLE OF CONTENTS xi

LIST OF TABLES xiv

LIST OF FIGURES xvi

LIST OF ABBREVIATIONS xx

LIST OF SYMBOLS xxiii

CHAPTERS

1 INTRODUCTION 1

1.1 Motivation 2

1.2 Research Objectives 3

1.3 Organization of Thesis 4

2 LITERATURE REVIEW 7

2.1 Variability of the Solar Radiation 7

2.2 Probability of Exceedance of Energy Yield 8

2.3 Uncertainty Components of Solar PV Energy Yield 12

2.3.1 Data Uncertainty 12

2.3.2 Energy Modelling Uncertainty 13

2.3.3 Statistical Uncertainty 15

2.4 Quality Assessment of Ground Measurements 15

2.5 Economic Analysis of a Solar PV Power Plant 16

3 THEORY AND METHODOLOGY 19
3.1 Data Analysis 20
3.1.1 Datasets 20
3.1.2 Quality Assessment of Ground-Measured Data 22
3.2 Solar PV Energy Yield Estimation 30
3.3 P50/P90 Analysis 35
3.4 Stochastic Simulation 38
3.5 Uncertainty Analysis 41
3.6 Economic Analysis 42
4 RESULTS AND DISCUSSION 47
4.1 Data Analysis and Quality Assessment 47
4.1.1 Validation of Ground Measurements 55
4.1.2 Variability of Global Horizontal Irradiation 61
4.1.3 Global Tilted Irradiation Results 63
4.2 Energy and Economic Yield Estimations 67
4.2.1 TMY, Empirical and Normal Distribution 69
4.2.2 Stochastic Simulations 75
4.2.3 Effects of GHI and Temperature on Energy Yield 80
4.2.4 Overall Uncertainty 83
4.2.5 Levelized Cost of Electricity 84
5 CONCLUSIONS AND FUTURE WORK 87
5.1 Conclusions 87
5.2 Future Work 89
REFERENCES 91

APPENDICES

A. SAM simulation results of temperature, GHI, POA, AEP and LCOE using different TMY and satellite-based datasets with different transposition models used (Isotropic, HDKR, Perez). Statistical indices are also shown. 97

B. Computing sample example of stochastic simulation in SAM software. 98

LIST OF TABLES

TABLES

Table 2.1 Selected studies from the literature about the POE estimation of solar PV energy yield. 11
Table 3.1 Climatic conditions of the region and type of datasets used in the study. . 21
Table 3.2 Measured data and equipment details. 22
Table 3.3 Days with missing GHI and DNI measurements. Missing hours were replaced by satellite-data. 28
Table 3.4 Input parameters of the solar PV module [60]. 34
Table 3.5 Solar PV system inputs used in SAM software. 37
Table 3.6 Solar PV system losses used in SAM software. 38
Table 3.7 The input variables with their assumed distributions in the simulations with no financial model. Mean and standard deviations are shown in percentage. 40
Table 3.8 The input variables with their assumed distributions in the simulations with the financial model, PV LCOE Calculator. 41
Table 3.9 Financial assumptions and parameters used in the LCOE formula of solar PV. 43
Table 4.1 Relative root mean square error (rRMSE) of measured GHI, measured DNI, estimated GHI and constructed GHI with respect to satellite-based GHI and DNI data, obtained from daily total & monthly mean daily total DNI and GHI (kWh/m^2/day) for each year. DNI is available after June 2013. 54
Table 4.2 Relative RMSE values of estimated, constructed and satellite-based GHI with respect to measured GHI, for selected time periods in 2013 and 2015. 57
Table 4.3 Constructed ground-measured data results of monthly and annual mean daily total GHI (kWh/m2/day). 62
Table 4.4 Satellite-based data results of monthly and annual mean daily total GHI (kWh/m2/day). 63
Table 4.5 RMSE (%) with respect to measured GTI in 2016, excluding January and February. 64

Table 4.6 Energy yield (kWh/kWp) estimations using different datasets with isotropic sky-diffuse model. System Advisor Model (SAM) results were also shown for satellite-based data..... 68
Table 4.7 Simulation results of three different TMY data sets and satellite-based data for the 1 MW solar PV plant in METU NCC. POA, AEP and LCOE values were averaged according to different transposition models used in SAM software (Isotropic, HDKR and Perez). Detailed results are available in Appendix A..... 71
Table 4.8 Probability of exceedance values of annual GHI and energy yield according to Normal and Empirical CDFs. Deviation of Normal CDF from empirical CDF values are shown in the last column as percentages..... 74
Table 4.9 Empirical cumulative distribution results of stochastic simulation for satellite-based and TMY datasets. Deviation of the mean TMY results from mean satellite-based data are also given in percentages. 76
Table 4.10 P50, P90 and P90/P50 comparisons of energy yield using different methods. 80
Table 4.11 Sources of uncertainties in percentages and the overall uncertainty of the energy yield. 83

LIST OF FIGURES

FIGURES

Figure 2.1. The interannual variability of global horizontal irradiation between the years 1985 and 2004, shown in percentages (%) [20]. 8
Figure 3.1. Flowchart of the thesis. 19
Figure 3.2. Default solar radiation database for different regions of the world, available in PVGIS [53]. 20
Figure 3.3. Time series of uncorrected ground-measured data with 10-minute time steps and extra-terrestrial irradiation between 2010 and 2017. 23
Figure 3.4. Heat map of 10-minute measured GHI for time period 2010-2016. 23
Figure 3.5. Heat map of 10-minute measured DNI from the second half of 2013 to 2016. 24
Figure 3.6. A flowchart of detecting erroneous GHI, filling missing data, and estimating GHI when it is needed. 29
Figure 3.7. Time series of 10-minute measured ambient temperature between 2013 and 2017. 30
Figure 3.8. Summary of the procedure to find energy yield estimations using ground-measured data. 34
Figure 3.9. Stochastic simulation tools in SAM software. 40
Figure 3.10. Historical and projection data trends for the overnight capital cost of solar photovoltaics. Adapted from [64]. 44
Figure 3.11. Historical and projection data trends for the fixed operating cost of solar photovoltaics. Adapted from [64]. 44
Figure 4.1. kn-kt quality envelopes for measured and estimated data with upper and lower boundary layers in 2013. 47
Figure 4.2. kn-kt quality envelopes for measured and estimated data with upper and lower boundary layers in 2014. 48
Figure 4.3. kn-kt quality envelopes for measured and estimated data with upper and lower boundary layers in 2015. 48

Figure 4.4. kn-kt quality envelopes for measured and estimated data with upper and lower boundary layers in 2016. 49
Figure 4.5. A comparison of daily total E.T., satellite-based GHI (SARAH) and ground-measured GHI before the adjustment done to selected time period shown in rectangle, in 2011. 50
Figure 4.6. A comparison of daily total E.T., satellite-based GHI (SARAH), constructed GHI and ground-measured GHI after the adjustment, in 2011. 50
Figure 4.7. A comparison of daily total E.T., satellite-based GHI (SARAH) and ground-measured GHI before the adjustment done to selected time period shown in rectangle, in 2014. 51
Figure 4.8. A comparison of daily total E.T., satellite-based GHI (SARAH), constructed GHI and ground-measured GHI after the adjustment, in 2014. 51
Figure 4.9. A comparison of daily total E.T., satellite-based GHI (SARAH) and ground-measured GHI before the adjustment done to selected time period shown in rectangle, in 2015. 52
Figure 4.10. A comparison of daily total E.T., satellite-based GHI (SARAH), constructed GHI and ground-measured GHI after the adjustment, in 2015. 52
Figure 4.11. A comparison of daily total E.T., satellite-based GHI (SARAH) and ground-measured GHI before the adjustment done to selected time period shown in rectangle, in 2016. 53
Figure 4.12. A comparison of daily total E.T., satellite-based GHI (SARAH), constructed GHI and ground-measured GHI after the adjustment, in 2016. 53
Figure 4.13. Heat map of hourly measured GHI between 2010 and 2016. 56
Figure 4.14. Heat map of hourly constructed GHI between 2010 and 2016. 56
Figure 4.15. Comparison of constructed and measured GHI with satellite-based data in selected periods of 2013, for the validation of the method. 58
Figure 4.16. Comparison of constructed and measured GHI with satellite-based data in selected periods of 2015, for the validation of the method. 58
Figure 4.17. Comparison of ground-measured and satellite-based daily total DNI with rRMSE value, in 2014. 59

Figure 4.18. Comparison of ground-measured and satellite-based daily total DNI with rRMSE value, in 2015. 60
Figure 4.19. Comparison of ground-measured and satellite-based daily total DNI with rRMSE value, in 2016. 60
Figure 4.20. Monthly average daily total GHI at METU NCC, between 2005 and 2016 (PVGIS-SARAH), in comparison with PVGIS-TMY. 61
Figure 4.21. Monthly and annual COV values of ground-measured (constructed) and satellite-based GHI data. 63
Figure 4.22. A comparison of daily total global tilted irradiation (GTI) of satellite-based, measured and estimated data in 2016. 65
Figure 4.23. Comparison of GTI, GHI, beam and diffuse irradiation in 2014. 65
Figure 4.24. Comparison of GTI, GHI, beam and diffuse irradiation in 2015. 66
Figure 4.25. Comparison of GTI, GHI, beam and diffuse irradiation in 2016. 66
Figure 4.26. A comparison of satellite-based, ground-measured, TMY and actual energy yield results obtained from calculations and SAM simulations using isotropic sky-diffuse model. 68
Figure 4.27. Empirical cumulative distribution function of annual GHI according to satellite-based data between time period 2005-2016. 69
Figure 4.28. Empirical cumulative distribution functions of the energy yield (kWh/kWp) using Isotropic, HDKR and Perez models. Double arrows show the difference between the average TMY and P50 values. 72
Figure 4.29. Comparison of empirical and normal CDFs with average TMY result of the annual GHI, for time period 2005-2016. 73
Figure 4.30. Comparison of empirical and normal CDFs with TMY results of the energy yield, for time period 2005-2016. 74
Figure 4.31. CDF of energy yields generated by stochastic simulation, using all uncertainty distributions given in Table 3.7. 76
Figure 4.32. A comparison of empirical and stochastic CDF results, when only sky-diffuse model is changed. 78

Figure 4.33. A comparison of scenarios of different input variables used in stochastic simulation. 78
Figure 4.34. Comparison of stochastic simulations. Black lines were obtained by only changing sky-diffuse model, colored lines were obtained using the input variables in Table 3.7. 79
Figure 4.35. Correlation between the energy yield and annual GHI for time period 2005-2016. 81
Figure 4.36. Correlation between the energy yield and annual average daily mean temperature for time period 2005-2016. 82
Figure 4.37. Correlation between annual GHI and annual average daily mean temperature between 2005-2016. 82
Figure 4.38. Exceedance and non-exceedance probabilities of AEP and LCOE with error bands, respectively. Actual energy yield data of 2016 and 2017 are shown at closest points to the mean energy yield line. Average results for different TMY datasets are represented in filled pointers, upper and lower bounds are obtained from specific TMY datasets (PVGIS-TMY, TMYx.2004-2018, TMY2-Meteonorm). 85
Figure 4.39. Probability of exceedance values of energy yield and LCOE, obtained from stochastic simulations. 86

LIST OF ABBREVIATIONS

ABBREVIATIONS

AC	Alternating Current
AEP	Annual Energy Production
BSRN	Baseline Surface Radiation Network
CDF	Cumulative Distribution Function
COV	Coefficient of Vvariation
CSP	Concentrating Solar Power
DC	Direct Current
DHI	Diffuse Horizontal Irradiation
DNI	Direct Normal Irradiation
DSCR	Debt-Size Coverage Ratio
ECDF	Empirical Cumulative Distribution Function
ET	Extra Terrestrial
FCR	Fixed Charge Rate
FOC	Fixed Operating Cost
GHI	Global Horizontal Irradiation
GTI	Global Tilted Irradiation
HDKR	Hay, Davies, Klucher, Reindl
IEA	International Energy Agency
IRENA	International Renewable Energy Agency

kW	Kilowatts
LCOE	Levelized Cost of Electricity
LHS	Latin Hypercube Sampling
MATLAB	Matrix Laboratory
MCP	Measure-Correlate-Predict
MCS	Monte Carlo Simulation
MPPT	Maximum Power Point Tracking
MWp	Mega Watt peak
NOCT	Nominal Operating Cell Temperature
NREL	National Renewable Energy Laboratory
O&M	Operation & Maintenance
PDF	Probability Density Function
POA	Plane-of-Array Irradiance
POE	Probability of Exceedance
PV	Photovoltaics
PVGIS	Photovoltaic Geographical Information System
RMSE	Root Mean Square Error
rRMSE	Relative Root Mean Square Error
SAM	System Advisor Model
SARAH	Surface Solar Radiation Data Set Heliosat
SDR	System Degradation Rate
STC	Standard Test Conditions

TCC	Total Capital Cost
TMY	Typical Meteorological Year
TZ	Time Zone
VOC	Variable Operating Cost

LIST OF SYMBOLS

SYMBOLS

σ	Standard deviation
s	Standard deviation of a sample
μ	Mean
x_i	Individual value of a sample
$\bar{x}$	Mean value of a sample
R^2	Coefficient of determination
θ_z	Zenith angle
h	Solar elevation angle
β	Surface tilt angle
ρ	Surface albedo
G_o	Extra-terrestrial radiation on a horizontal surface
$G_{o,daily}$	Daily total extra-terrestrial radiation
G_{sc}	Solar constant
$G_{cs,daily}$	Daily total clear-sky radiation
GHI_{daily}	Daily total global horizontal irradiation
$GHI_{measured}$	Measured global horizontal irradiation
$GHI_{estimated}$	Estimated global horizontal irradiation
n	Day number of a year
N	Number of years in a time period

k_t	Clearness index
k_n	Beam transmittance
$\mu(k_t)$	Mean of clearness index during a day
$\sigma(k_t)$	Standard deviation of clearness index during a day
E_{PV}	Annual energy production from solar PV power plant
$\eta_{PV,i}$	PV module efficiency at i^{th} hour
$\eta_{PV,ref}$	Reference PV module efficiency under standard test conditions
$T_{ref,STC}$	Reference PV module temperature under standard test conditions
A_{PV}	PV module area
N_{PV}	Number of PV modules in a solar PV power plant
T_{PV}	PV module temperature
β_t	Temperature coefficient
T_{ref}	Reference temperature under normal operating conditions
G_{ref}	Reference irradiation under normal operating conditions
$T_{ambient}$	Ambient air temperature
T_{NOCT}	Nominal operating cell temperature
$\sigma_{overall}$	Overall uncertainty of annual energy production
σ_{data}	Data uncertainty
σ_{POA}	Transposition model uncertainty
$\sigma_{interannual}$	Interannual variability of global horizontal irradiation
σ_{dirt}	Dirt and soiling uncertainty

σ_{other}	Other sources of uncertainty
C_0	Initial investment cost
M_i	Annual total operation and maintenance cost
r	Annual discount rate
t	Project lifetime
t_s	Solar time
t_{std}	Local time
L_{st}	Standard meridian
L_{loc}	Longitude of location
E	Equation of time
ω	Hour angle
γ	Surface azimuth angle
γ_s	Solar azimuth angle
δ	Declination angle
ϕ	Latitude

CHAPTER 1

INTRODUCTION

Transformation to carbon-neutral energy systems is needed to limit the global temperature rise below 2ºC above pre-industrial levels, therefore, the share of renewable energy systems should increase to 86% globally by 2050, according to the International Renewable Energy Agency (IRENA) [1]. However, penetration of renewables into electricity grids faces some challenges such as technical and financial risks since their energy production is variable and nonsynchronous [2]. Moreover, while project developers can overpredict the expected energy yield of a renewable energy project to attract investors and ensure financing, investors are more interested in whether the project will meet the energy production and financial targets [3]. Thus, investors and financial institutions require the probability of exceedance (POE) values of the predicted energy yields of solar and wind energy systems throughout their operational lifetime to ensure the bankability of projects [4], [5]. A long-term dataset of the solar resource is needed to calculate POE values of the energy yield of a solar energy project since the variability of solar radiation primarily affects the amount of solar energy production, which in turn, the economic risk associated with the level of energy output and revenues can be determined [6]. Additionally, knowing POE values gives information about "stress cases" of the solar resource and the energy output of a project, which is important for debt providers to see whether a project is feasible in debt repayment and cash flow [7]. Specifically, the P90 value refers to the annual energy generation that will be met or exceeded in 90% of any given year during a power plant's operational life. Therefore, a P50 value is used for a median or representative year, whereas P10 and

P90 values are used for high and low resource years, respectively [8]. P95 and P99 values can also be requested to see the worst-case energy yield values.

Generally, a typical meteorological year (TMY) data is used for the preliminary design of renewable energy projects, representing the most typical weather conditions of a site, and it is a statistically constructed 1-year data set [9]. However, TMY data sets do not include outlier weather events and the interannual variability of the solar resource such as sunspot cycles, global dimming and brightening, change of aerosol particles, cloud cover due to volcanic eruptions and wildfires, also, possible effects of climate change that can affect the atmospheric turbidity, water vapor content and precipitation [10]. The incoming solar radiation changes because of the outliers; thus, TMY data is not recommended to be used in resource risk assessments, although it enables faster energy simulations, requires much less computational memory and is suitable for rough modeling [11]–[14]. Long-term ground measurements are recommended to predict the solar irradiation best; however, they are not available in every part of the world for long periods. Thus, satellite-based data sets can provide historical time series data in most of the regions [4], [11], [15]. Site-adaptation techniques such as measure-correlate-predict are recommended to remove the bias from satellite-based data if short-term ground-measured data also exist [3], [16].

By virtue of this study, it aims to enable more solar PV projects by showing that there is a huge potential of solar energy in this region and prove that solar PV electricity is feasible.

1.1 Motivation

Lower-than-expected solar resource leads to lower energy yields in an energy project which can cause financial risks in power-purchase agreements (PPAs) and in off-take agreements when the time-of-day pricing is important [15]. Thus, investors require to simulate a power plant's energy performance during its operational life to ensure whether it is a bankable project [5]. Moreover, debt providers require to know

the quality of data, long-term estimate of the energy output and POE values of the expected energy output [8], [15].

If POE values do not exist, uncertainties of input parameters can be assumed by a sensitivity analysis for a more reliable energy performance estimate [5]. A sensitivity analysis was done previously in METU NCC for a PV-wind-battery hybrid system using both TMY and short-term measured data for GHI and wind speed, and wind resource was found to have higher uncertainties compared to solar radiation [17]. However, solar PV energy has not been studied in terms of uncertainty, and POE values have not been found for a renewable energy system. Thus, a more detailed analysis of solar PV's long-term energy yield is needed for this region to make new solar PV plant installations with improved confidence levels in terms of energy and economic yields.

Knowing that the current electricity grid in Northern Cyprus is heavily dependent on fossil fuel-burning power plants, it is urgent to decarbonize the electricity supply system and increase the share of renewable energy to reduce the effects of global warming and climate crisis. In this way, we can contribute to sustainability by having access to "affordable, reliable, sustainable and modern energy," which is the seventh goal of the Sustainable Development Goals of the United Nations [18]. The results of this study aims to reduce the uncertainties related to solar PV energy output, show the bankability of installing large-scale solar PV power plants, as a result, to fasten the clean energy transition by using solar energy in the current electricity system. Therefore, we can pave the way for a sustainable energy supply.

1.2 Research Objectives

The objective of this study is to find the long-term energy yield estimations for 1 MWp solar PV plant in METU NCC as a case study, which in turn, energy exceedance probabilities such as P50 and P90 values can be found. Thus, the uncertainty related to solar PV energy output can be obtained and reduced, which

can help to make better investment decisions of commercial-scale solar PV plants in the studied region with improved confidence levels. Also, both intra-annual and inter-annual variabilities of the solar resource are to be found to see the variations of seasonal and annual energy yields. Research objectives can be summarized as follows:

- Checking the quality of ground measurements
- Comparing different weather datasets such as TMY, satellite-based and ground-measured data to see their effects on energy yield
- Obtaining long-term trends of the solar resource
- Analyzing the uncertainty components of solar PV energy yield, and estimating the overall uncertainty
- Estimating the energy yield and its POE values using different methods such as empirical method, Normal distribution assumption and stochastic simulations
- Obtaining a range for the levelized cost of electricity (LCOE)

1.3 Organization of Thesis

This thesis is organized as follows: Chapter 1 introduces the problem statement and research objectives. In Chapter 2, literature review of the variability of the solar radiation, the probability of exceedance of energy yield, the uncertainty components of solar PV energy yield (data, energy modeling and statistical uncertainty), the quality assessment of ground measurements and the economic assessment of a solar PV power plant were done. In Chapter 3, the theory and methodology are described for data analysis, solar PV energy yield estimation, P50/P90 analysis, stochastic simulation, uncertainty analysis and calculating the LCOE. Chapter 4 presents the results and discussions of data analysis, energy and economic yield estimations. Under the energy and economic yield estimation results, probability of exceedance, effects of GHI and temperature, overall uncertainty and the LCOE are discussed. Conclusions and future work are given in Chapter 5.

CHAPTER 2

LITERATURE REVIEW

In this chapter, previous studies about the variability of the solar resource, the POE of energy yield, uncertainty components of solar PV energy yield, quality assessment of ground measurements, and the economic assessment of a solar PV power plant are presented.

2.1 Variability of the Solar Radiation

The Sun emits radiation continuously, and it is called the extra-terrestrial (ET) radiation above the atmosphere of Earth [19]. Due to the variations in the sunspot activities, solar cycles are observed every 11 years; however, it has a negligible effect on the solar constant, which is estimated as 1367 W/m^2 by the World Radiation Center [19]. On the other hand, the distance between Earth and Sun changes during a year because of the eccentricity of the Earth's orbit, which introduces about 3.3% variation on ET radiation [19]. In addition, the tilt of the Earth's axis and its rotation cause seasonal and daily variations in the amount of solar radiation. These variations are well known, and the solar geometry is predicted using angles, such as solar elevation, zenith, azimuth and declination [19]. However, solar radiation reaches the surface by passing through the Earth's atmosphere, and three components of solar radiation on a horizontal surface are formed: direct, diffuse and reflected irradiation. While diffuse irradiation results from the scattering of clouds, aerosols and other particles, the direct (beam) component reaches the surface without scattering, and reflected irradiation reaches the surface with the reflectivity of the ground [19]. The variability introduced by weather events such as cloud cover is less predictable; thus, the nature of the solar resource becomes stochastic [4]. There are both temporal and spatial variabilities: temporal variability can vary from seconds to years, decreasing

as the time period increases [4]. Spatial variability also smoothes as the considered site or region expands [4].

In this study, the long-term solar radiation trends are analyzed since the interannual variability of GHI is important to determine whether the solar energy potential of a site is feasible and bankable for a solar energy project throughout its operational lifetime. In Figure 2.1, the interannual variability of GHI in the Mediterranean area for the time period 1985-2004 is shown, according to a previous study done in 2007 [20].

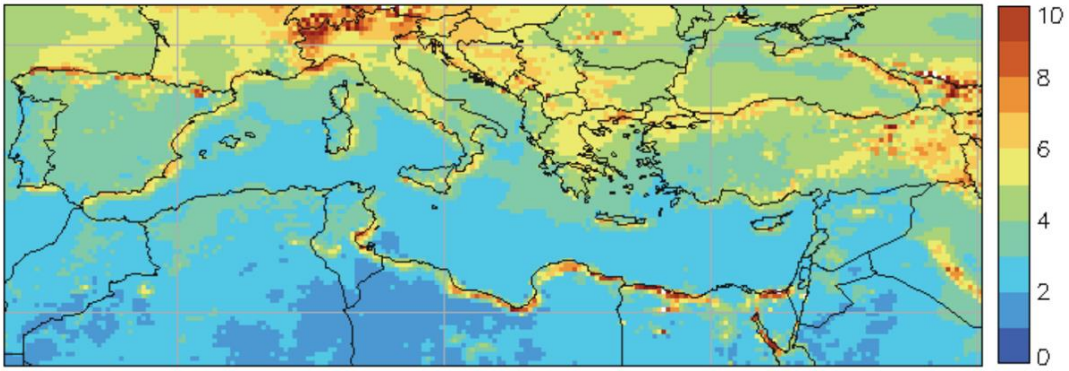

Figure 2.1. The interannual variability of global horizontal irradiation between the years 1985 and 2004, shown in percentages (%) [20].

2.2 Probability of Exceedance of Energy Yield

Energy exceedance probability values such as P50 and P90 are needed when the level of confidence of energy yield estimates is required by debt providers for making decisions on new renewable energy investments, and POE values are generally obtained using statistical methods [6]. Since renewable energy sources such as solar radiation and wind speed have stochastic nature, a specific statistical probability density function (PDF) does not always fit the data set. However, an assumption can be made by fitting data to a PDF, and its representativeness can be checked by statistical tests, such as goodness of fit and Normality tests [4], [21], [22].

Different methods were developed to calculate POE values; however, there is not an industry-standard methodology in the research field for doing resource risk assessments and estimating POE values [5], [12], [22]. The simplest method is the SolarGIS approach [12], in which an average solar resource year is represented by "TMY P50" data set, assuming that P50 value of the annual energy production (AEP) can be calculated with TMY data. Normal distribution was assumed for the annual solar irradiation; also, a combined uncertainty was used to account for the modeling estimate and interannual variability; thus, "TMY P90" was created to represent a low solar resource year. However, it is not recommended to use TMY data sets for risk analyses and multi-year time series data to see the effects of solar radiation variations on the AEP. Similarly, representative TMY data sets of DNI were created for concentrated solar power plants in the EVA method [15]. POE values were created from the annual energy outputs of the 34-year ground measurement data set, and the distribution of annual DNI values was fitted to Weibull PDF. However, a minimum of 15 years of DNI data is required for this method, and information is lost when generating TMY data sets. On the other hand, Dobos and Kasberg [23] assumed Normal distribution for the solar irradiation, but they also used the empirical cumulative distribution function (CDF) to calculate POE values. They found 2% lower estimates with the empirical method than the normally distributed value for the P90. On the other hand, Tadesse et al. [13] used a synthetic year generation approach to increase the length of the data set, which works by dividing each year into 4-month periods, taking the average of each period and creating all possible years from these periods. They also compared the POE values of their method with the Normal distribution assumption, and a 3% lower result was found for the P95 value with the Normal distribution assumption. Another study aimed to find the POE values using 19-year weather data and TMY datasets of 18 different PV plants worldwide [10]. They used the Kernel density function to find the PDF of long-term data, and Normal distribution was assumed for TMY datasets. They assumed the standard deviation of annual GHI as the interannual variability in TMY case. Then, they compared POE values of both cases and the interannual variability was found

to be dominant among other uncertainties, which causes about 3-5% difference in POE values. However, this study is not site-specific. Besides, a recently published study in Korea [24] compared three different distributions by calculating POE values of monthly and annual mean PV power potential, which are the Normal, Skew-Normal and empirical distributions. They used 27-year ground measurements, and it was found that skew-normal distribution was closer to the empirical CDF than normal distribution, which was concluded to be a more realistic modelling assumption.

Up to now, POE methods have found single values based on the first-year energy yield of a solar project. To predict the lifetime average energy yield values, Monte Carlo simulation (MCS) and Latin hypercube sampling (LHS) methods are suggested to generate hundreds of possible results from a limited number of data sets to enable resource risk assessments with time-dependent POE values [4], [25]. According to the International Energy Agency's (IEA) report under Task 13 published in 2018 [25], a general method was suggested to estimate the lifetime energy yield predictions and to include all sources of uncertainties that affect the estimations, which enables time-dependent POE values rather than calculating a single value for each exceedance probability. The method first chose a reference period from the historical data time series. It calculated the predicted reference energy yield to estimate the best mean annual yield by using a simulation tool, and finally, calculated the predicted energy yields over the prediction period by applying long-term changes of all parameters and models to the predicted reference energy yield with the use of Monte Carlo approach [25]. Thevenard and Pelland [26] followed this method in their study using the statistical modeling of System Advisor Model (SAM) software, in which the LHS method is used. They found that the lifetime average energy yield's uncertainty is 7.9%, whereas 8.7% uncertainty was found for the first year since solar radiation variability decreases as the time period increases. Belluardo et al. [27] also used the Monte Carlo approach in PVsyst software and the Normal distribution assumption to estimate the PV energy yield, and they obtained a 5-10% uncertainty range according to different scenarios. While

doing MCS with a more extended dataset of ground-measured data gave the lowest uncertainty, the highest uncertainty was found in assuming Normal distribution with a shorter dataset of satellite-based data [27]. A summary of the discussed studies can be seen in Table 2.1.

Table 2.1 Selected studies from the literature about the POE estimation of solar PV energy yield.

Study	Location	Parameter	Fitted PDF	Type of Data	Measured Period	Temporal Resolution	Calculated Metric	Software
Cebecauer & Suri, 2015	Almeria	GHI DNI	Normal	TMY	20 years	sub-hourly	TMY P50 TMY P90	SolarGIS
Fernández-Peruchena et al., 2018	Burns, Oregon (USA)	DNI	Weibull	ground	1980-2013	hourly	P10, P50, P90, P99	SAM R
Dobos & Kasberg, 2012	Phoenix, Arizona (USA)	GHI DNI DHI	Normal Empirical	TMY satellite	1961-2005	hourly	P50, P90	SAM
Tadesse et al., 2017	USA	GHI	Synthetic Normal	TMY satellite	1998-2016	hourly	POE	PVsyst
Pelland et al., 2016	worldwide 18 ground stations	GHI	Kernel Normal	TMY satellite	1997-2016	sub-hourly	POE	PVsyst
Kim et al., 2020	4 cities, Korea	GHI	Skew-Normal Empirical	ground	1991-2017	hourly	P50, P90	–
Thevenard & Pelland, 2013	Ontario, Canada	GHI	Normal	TMY ground	1960-1989	hourly	year-1 & lifetime average yield	SAM
Belluardo et al., 2017	Bolzano, Italy	GHI GTI	Normal Empirical	ground	22 years	hourly	P50, P90 P90/P50	PVsyst

2.3 Uncertainty Components of Solar PV Energy Yield

Uncertainty quantification of all inputs, parameters and modeling steps is required to predict the long-term energy yields with high confidence levels, and an overall uncertainty should be obtained by combining individual uncertainty sources [25]. Reducing the overall uncertainty means higher energy estimates, thus, reduced financial risks, increased potential revenues and lower electricity costs [28].

2.3.1 Data Uncertainty

Measuring devices should be well maintained and calibrated for an accurate data set; therefore, measurement uncertainties should be considered if ground measurements are used. If satellite data is used, data should be validated, and modeling data uncertainties should be considered. Site adaptation techniques are applied to the long-term satellite-derived data by using short-term on-site ground-measured data to correct systematic errors and bias, since satellite data may differ from ground data because of atmospheric effects such as aerosols, water vapor and cloudiness, also, albedo and topography of the region [16]. At least 1-year ground measured data is required to include seasonal effects for site adaptation [16]**.**

Temporal representativeness is another important factor that should include interannual variability. According to a study done by Müller et al. [29], global dimming and brightening effects, which is a multi-decadal trend for solar irradiance, were observed between years 1951-2010 in Germany, and they found that a 3% uncertainty is added to predictions if an average GHI obtained from historical data will be used for the future average GHI. This uncertainty level can increase up to 4-5% for 30º-tilted, south-facing panels for GTI and to 15% for DNI [29]. To best predict the future GHI trend throughout a PV plant's operational life, the most recent 10-year data is suggested to calculate the energy yield predictions in IEA's report [29]. When the on-site ground measurements have short periods of record, they can be adjusted by long-term satellite data using the measure-correlate-predict (MCP)

method so that the uncertainty related to the length of the historical period can be reduced [30]. The temporal resolution of data also affects the energy performance estimates. For example, sub-hourly direct normal irradiance (DNI) measurements are required for concentrating solar power (CSP) energy yield estimates [4]. The spatial resolution of data also has uncertainties, especially if near-site measured data is used and if the analysis is done for spatially dispersed power plants [31].

2.3.2 Energy Modelling Uncertainty

When estimating the annual energy output in energy simulation programs, many input parameters are required, such as PV system design characteristics, system losses, reference weather data and long-term energy yield simulation assumptions [5]. For solar energy and its PV application, the sources of uncertainties can be summarized as follows.

a. Converting GHI to POA Irradiance

Transposition models, which are applied to GHI time series to calculate the plane-of-array (POA) irradiance, introduce a level of uncertainty, and the accuracy of the models should be known [25]. To obtain POA irradiance, GHI is first decomposed into DNI, DHI and ground-reflected irradiance by using one of the decomposition models, such as Erbs, Ruiz and Skarveit [25]. The three components are then recombined to obtain POA by using algorithms such as isotropic, Hay & Davies, Muneer and Perez [25]. A study done in France showed that the highest accuracy is obtained by combining Skarveit and Hay & Davies models, compared to measured inclined irradiation values [26]. Another study was done across ten stations in the U.S., and they evaluated the performance of several decomposition and transposition models to obtain POA irradiance from measured GHI/DHI [33]. It was found that simple decomposition models generally underpredict DHI during cloudy periods and overpredict during clear periods, whereas the isotropic model estimates the lowest POA among transposition models [33]. Also, Hay & Davies and Perez models have the smallest errors in transposition models; however, the Perez model was not

recommended if the measured DHI is not available since the model is highly sensitive to the quality of the measurements [33]. The combination of Erbs and Hay & Davies models gave the smallest errors compared to measured POA when obtaining POA from measured only GHI. Nevertheless, it was concluded that measuring POA irradiance will reduce the biases in PV energy estimations [33].

b. Operating PV Cell Temperature

The incident solar radiation, ambient air temperature and wind speed are the primary drivers that affect the module temperature of PV, thus, the PV module efficiency [32]. As a result, the PV power output is affected by the variability of air temperature, and a proper correlation for the operating temperature of a PV module should be chosen [33]. In addition, the temperature coefficient of module efficiency adds another uncertainty, which was assumed as 10% for all technologies [25]. It was also mentioned that temperature is the largest influencer on the PV energy yield in hotter locations, whereas irradiance is the most important one with disregard of location [25].

c. PV Module Efficiency

PV module efficiency changes as a function of weather conditions, although initially, it is constant under standard test conditions (STC), and the module performance ratio (MPR) is used to account for the factors that affect it and to compare different PV modules at different locations [25]. Losses due to module reflection characteristics are approximated to account for 1% uncertainty for all locations and modules; however, detailed analysis or information from PV specifications is required [25]. The spectral shape of the incident solar irradiance also creates uncertainties; however, this effect is lower than the temperature and irradiance effects, about 2% for monocrystalline and polycrystalline silicon PV technologies [25].

d. Soiling, Shading, Reflection and Snow Cover

The soiling rate of solar PV panels significantly affects the energy losses, and a physical model of PV soiling mechanisms does not exist. In addition, local weather characteristics (wind, rain) and the operation and maintenance (O&M) of PV surface

cleaning schedules can estimate soiling rates more complicated [25]. Therefore, Fraunhofer Institute of Solar Energy (ISE) [25] developed a simplified approach to predict the uncertainty related to yearly averaged soiling loss as 2% for tilt angles above 15º. Shading and snow cover also cause a decrease in PV energy generation, and sometimes satellites may not recognize the difference between snow cover and the clouds.

e. Energy Modelling and Simulation Tools

Energy simulation tools and chosen models to calculate the actual energy production based on historical time-series data also have uncertainties related to the assumptions, chosen parameters and assumed losses [25]. On the other hand, PV system design characteristics such as orientation and tilt angle of PV modules affect energy generation. They should be optimized if they are fixed, or a tracking system is available (1-axis or 2-axis).

2.3.3 Statistical Uncertainty

To find the exceedance probabilities of annual energy yields, the solar resource's probability density function can be plotted over a specific time period and are generally fitted to specific statistical PDFs. For example, Weibull distribution is commonly fitted to predict DNI, whereas, Normal and Beta distributions are considered to fit GHI best [15], [21], [22], [34]–[37]. Thus, fitting PDFs also creates uncertainties, such as determining the shape and scale parameters of specific functions [15].

2.4 Quality Assessment of Ground Measurements

Financial institutions require bankable datasets to guarantee investments on large-scale solar energy projects, reducing the overall uncertainty of energy yield estimates [38]. Long-term modeled data such as satellite-derived data is mostly available globally; however, their systematic errors and bias should be removed by integrating

quality-checked ground measurements called “site adaptation” [39]. However, quality control of ground-measured data plays an important role in preventing erroneous results; otherwise, modeled data bias can increase [39]. Systematic errors of satellite-based data arise from low spatial resolution, assumptions on atmospheric data such as aerosols and water vapor, and irradiance models used, whereas ground measurements have erroneous data because of the inaccuracy of sensors, lack of calibration or error, and error due to insufficient maintenance to prevent soiling and shading [40]. Most erroneous data is recorded at sunrise and sunset times when the solar elevation angle is below 7º, which is called the cosine error, and these measurements are generally excluded [41], [42]. Reflection from the clouds and refraction of the atmosphere can cause positive measurements before sunrise and after sunset, which creates problems for the hours that contain sunrise and sunset times; thus, these measurements can be neglected [19].

Several quality check tests were developed by institutions and researchers for measured solar radiation data using physical limits and the relations between radiation components [41]–[43]. For example, Journee and Bertrand [43] applied several quality tests to sub-hourly solar radiation data such as physical threshold, step, persistence, quality envelope, sunshine and spatial consistency tests. Physical threshold and quality envelope tests were applied to the ground measurements used in this thesis.

2.5 Economic Analysis of a Solar PV Power Plant

Levelized cost of electricity (LCOE) is a useful economic metric to compare the viability of different energy generation technologies, which is the ratio of the total life cycle cost and energy production, in USD/kWh [44], [45]. There are several key parameters to calculate the LCOE of a renewable energy project, which are the capital expenditures, annual operation and maintenance expenditures, discount rate, annual energy production (AEP) and the project’s operational lifetime [45].

Previous case studies were done for METU NCC, and different assumptions were made for the economic assessments. For instance, solar PV investment cost varied from 1388 to 3200 USD/kW, whereas the annual total operation and maintenance (O&M) cost was between 14 and 25 USD/kW [17], [46]–[49]. The annual discount rate was assumed as 9% in [17], [47], while 10% was suggested in [49]. A sensitivity analysis was conducted to see the effects of solar and wind resources on the LCOE, and it was found that a 20% change in weather parameters of the TMY data set would deviate the LCOE by 8% [17]. However, further research is needed to see the long-term variability of renewable resources and their impacts when calculating LCOE throughout the operational lifetime of a plant.

CHAPTER 3

THEORY AND METHODOLOGY

In this chapter, different methods used throughout the study were explained, which can be applied to different sites and solar PV energy projects; thus, the methodology is widely applicable. In this study, the methodology was applied to the 1 MWp solar PV plant at METU NCC as a case study. First, data analysis was conducted, and different types of datasets were downloaded from different sources. Then, a quality assessment was done to the ground measurements, which has some erroneous data points. Using these datasets, energy yield was estimated, P50/P90 analysis was conducted to find the POE values, and a stochastic simulation was also done. Both SAM software and custom codes in MATLAB were used to do the calculations. Finally, the overall uncertainty of the energy yield was estimated, and the LCOE range was obtained. Figure 3.1 shows the flowchart of this thesis.

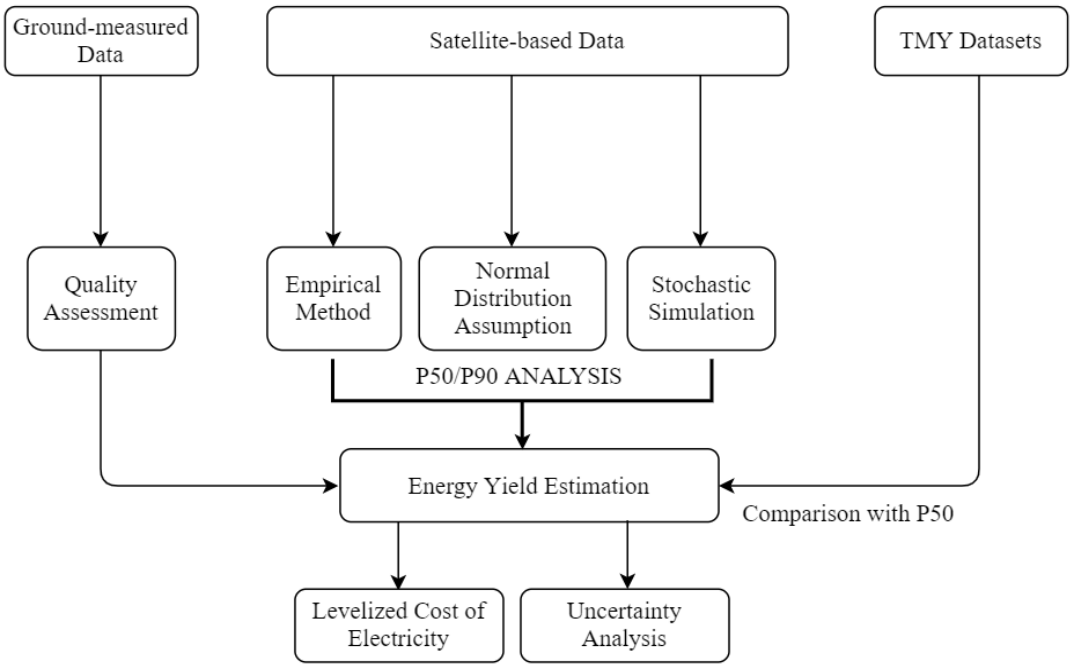

Figure 3.1. Flowchart of the thesis.

3.1 Data Analysis

3.1.1 Datasets

Long-term solar radiation data is required to find the POE values of energy yield estimations. In this study, both ground measurements and satellite-based data were used, whereas TMY data was used to compare P50 values. The satellite-based data was downloaded from the PVGIS web interface, and three different TMY data sets were used to obtain a general TMY result, which are TMY2-Meteonorm [50], TMYx.2004-2018 [51] and PVGIS-TMY [52]. Using different TMY datasets is to obtain an average TMY result, and the number of datasets can be increased if there are more data sources. For the long-term satellite-based data, the SARAH database was recommended for Europe, Africa, Asia, and South America regions, covering 12 years from 2005 to 2016 [53]. In Figure 3.2, default satellite databases for different parts of the world from the PVGIS interface are shown. In Table 3.1, site-specific climatic conditions of METU NCC and the type of datasets used in the study can be seen.

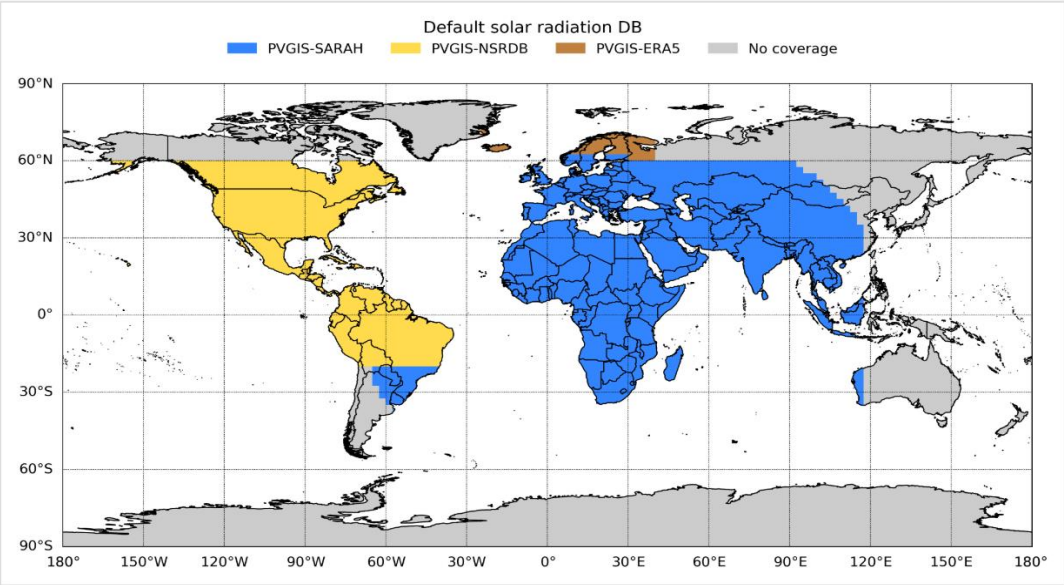

Figure 3.2. Default solar radiation database for different regions of the world, available in PVGIS [53].

Table 3.1 Climatic conditions of the region and type of datasets used in the study.

Location	METU NCC, Cyprus		
Latitude	35.25º N		
Longitude	33.02º E		
Elevation [m]	118		
GHI [kWh/m^2/day]	5.36		
DNI [kWh/m^2/day]	6.05		
DHI [kWh/m^2/day]	1.62		
Average Temperature [ºC]	19.7		
Average wind speed [m/s]	3.2		
Köppen-Geiger Climate	Csa		
Database	Satellite-based	Ground-measured	TMY
Time resolution	hourly	10-min	hourly
Time period	2005-2016 (12 years)	2010-2016 (7 years)	1 year

The PVGIS-SARAH data sets were validated by comparing them with the ground measurements provided by the Baseline Surface Radiation Network (BSRN) [54]. Although there is no validation study for Cyprus, the nearest BSRN stations are in Israel and Greece, where the relative mean bias deviations are +3.4% and +3.6%, respectively [54]. In addition, considering that Cyprus is in the middle of the two stations in Israel and Greece, it can be assumed that SARAH data overpredicts GHI up to 3.6% on average for the Cyprus region.

Satellite-based data includes in-plane beam and diffuse irradiance, sun elevation, air temperature at 2 meters and the wind speed at 10 meters above the ground. In the web interface, hourly time series data was downloaded for the location of the installed solar photovoltaic (PV) power plant at METU NCC, where the latitude is 35.253ºN and longitude is 33.016ºE. Fixed mounting type with zero slope and south-facing azimuth angle was given as inputs. Direct normal irradiance (DNI) values were calculated according to the zenith angle since SAM uses weather data inputs as GHI, DNI and DHI. In addition, individual weather files with 8760 hours were created for each year from the 12-year time series data because SAM is designed to run simulations for annual weather datasets. For this reason, leap days were removed from the years 2008, 2012 and 2016.

Apart from satellite-based and TMY datasets, ground-measured data has been recorded with 10-minute time steps. GHI has been measured with a pyranometer since January 1, 2010, while DNI has been measured with a pyrheliometer since June 1, 2013, at the solar PV power plant in METU NCC. After 2017, the quality of measurements reduced significantly; therefore, data between 2010 and 2016 were used. In addition, global tilted irradiation (GTI) has been recorded with a 30º-tilted pyranometer since February 13, 2016. In Table 3.2, details of measured data and sensor equipment at the solar PV plant are provided.

Table 3.2 Measured data and equipment details.

Measured parameter	Symbol	Type of instrument	Manufacturer	Model	Measured since
Global horizontal irradiance	GHI	pyranometer	Kipp & Zonen	CMP-22	2010
Direct normal irradiance	DNI	pyrheliometer	Kipp & Zonen	CHP-1	2013
Global tilted irradiance	GTI	30º-tilted pyranometer	Kipp & Zonen	CMP-10	2016
Temperature	T	thermometer	Kintech Galtech	KPC 1/5	2013
Recorded data	–	data logger	Campbell Scientific	CR800	–

3.1.2 Quality Assessment of Ground-Measured Data

Missing and suspicious data were found both for GHI and DNI. Thus, quality assessment was done to detect erroneous data points using quality control tests. For GHI, physically impossible values were found using ET radiation on a horizontal surface. Figure 3.3 shows the time series of the ground-measured data with 10-minute time steps and ET irradiation. Figures 3.4 and 3.5 also show the heat map of ground-measured GHI and DNI data, respectively.

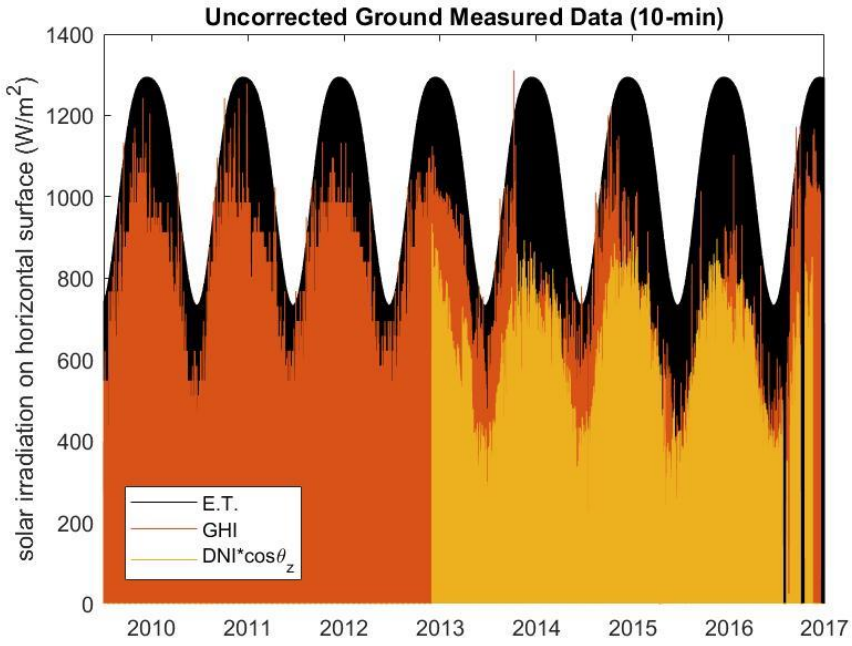

Figure 3.3. Time series of uncorrected ground-measured data with 10-minute time steps and extra-terrestrial irradiation between 2010 and 2017.

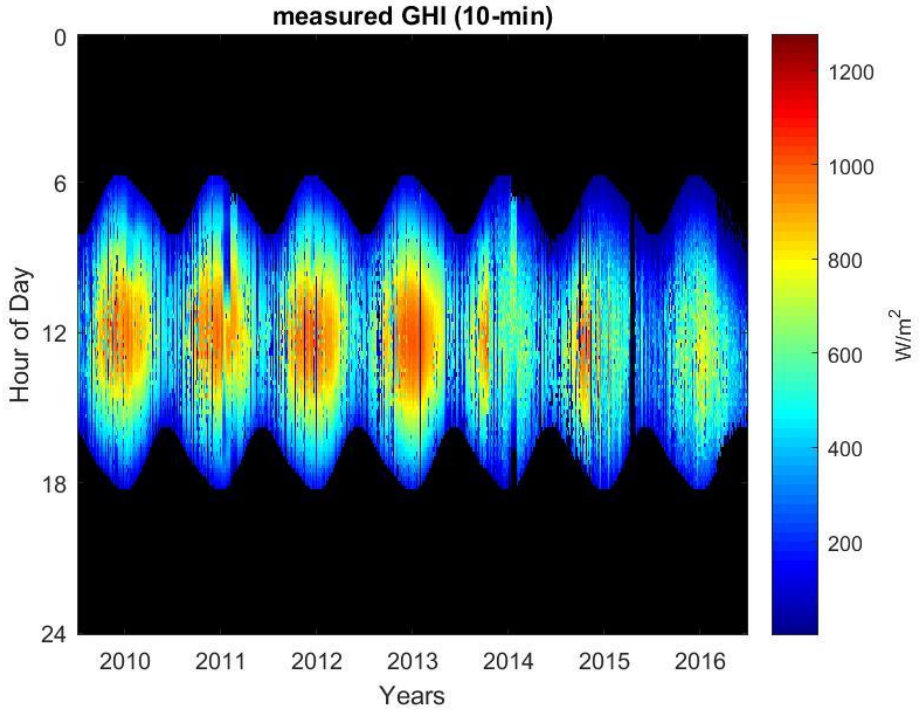

Figure 3.4. Heat map of 10-minute measured GHI for time period 2010-2016.

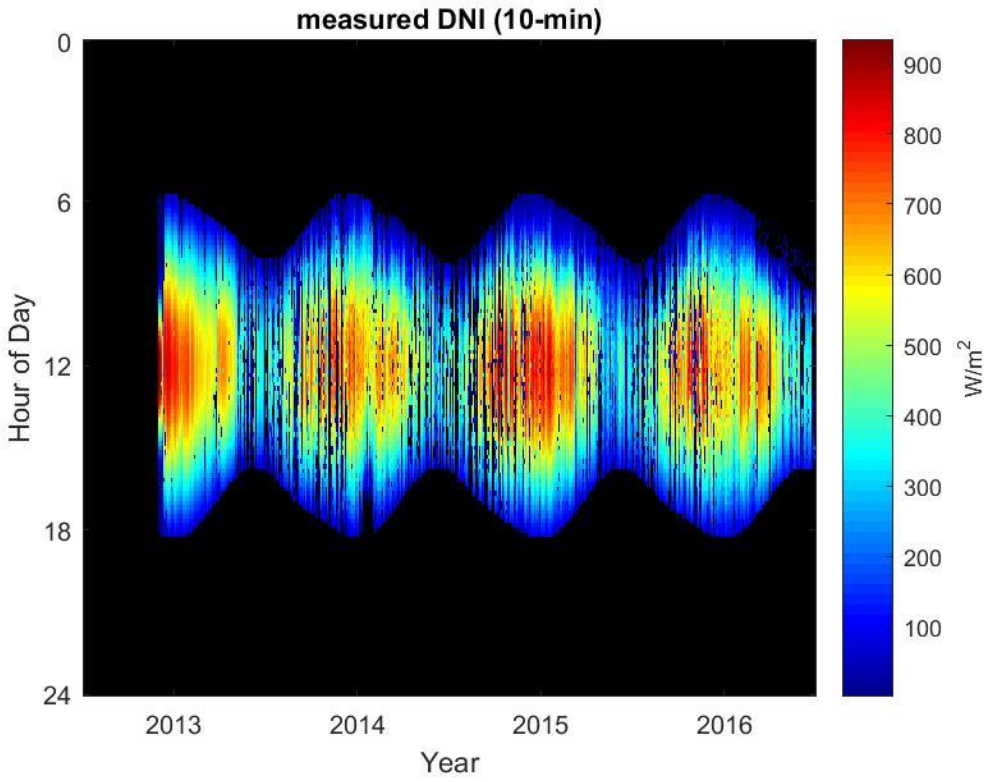

Figure 3.5. Heat map of 10-minute measured DNI from the second half of 2013 to 2016.

The following adjustments were made to the ground measurements:

- Leap days were removed from the years 2012 and 2016.
- All GHI and DNI data before sunrise and after sunset were converted to zero to correct any missing and positive values, as suggested by [54].
- To exclude any possible error due to sunrise and sunset times, GHI and DNI data were converted to zero when the solar elevation angle (h) is below 7º.
- For the upper limit, data were changed to missing if GHI exceeds the extra-terrestrial radiation on a horizontal surface (G_o) during daylight.

$$GHI < G_o \; if \; h > 0° \tag{1}$$

$$G_o = G_{sc}\left(1 + 0.033\cos\frac{360n}{365}\right)\cos\theta_z \tag{2}$$

where G_{sc} is the solar constant that is assumed as $1367\ W/m^2$, n is the day number in a year, and θ_z is the zenith angle [19].

- For the lower limit, data were changed to missing if GHI is lower than expected. Heavily overcast conditions determine the minimum GHI, and the following condition was adapted for sub-hourly data from [43]:

$$GHI \geq 10^{-4} \times (h - 10)\ \times\ G_o\ if\ h > 10° \tag{3}$$

- A persistence test was applied to all GHI data during daylight to find any sensor failure due to intermittent and/or constant recordings. Equation (4) was used from [43]:

$$\frac{1}{8}\mu(k_t) \leq \sigma(k_t) \leq 0.35\ \ if\ h > 10^0 \tag{4}$$

where k_t represents the clearness index at each time step, $\mu(k_t)$ and $\sigma(k_t)$ are the mean and standard deviation of clearness index values at each day, respectively. However, this test did not work for the Cyprus region, and it found clear-sky days rather than constant and intermittent measurements because of sensor failure. This test was studied over Belgium; thus, parameters may change due to site-specific conditions as indicated by the authors [43].

- For daily total GHI values, lower and upper limits were suggested by [55] :

$$0.03 \times G_{o,daily} < GHI_{daily} < 1.1 \times G_{cs,daily} \tag{5}$$

where $G_{o,daily}$ is daily total E.T. radiation, GHI_{daily} is daily total GHI measurement, and $G_{cs,daily}$ is daily total clear-sky radiation. In this study, clear-sky radiation was not found since it would introduce complex

parameters such as relative air mass, Linke turbidity factor and Rayleigh optical depth [42], [43], [55]. In addition, lower-than-expected GHI values were observed in the last years when compared to DNI measurements and satellite-based data. Thus, a lower limit was tested as a priority.

- 10-min data points were averaged to hourly values, omitting missing values. However, hourly data were kept as missing if a whole hour of data points were missing.
- An estimation was then done for GHI using the Erbs model [43], [56]. Since DNI measurements were available from June 2013, estimated GHI values were calculated based on beam transmittance, k_n (B/G_o) and the following conditions in equation (6):

$$\begin{cases} k_t = \sqrt{\frac{k_n}{0.09}} \quad if \quad 0 < k_n \leq 0.004356 \\ f(k_t) - k_n = 0 \;\; where \; f(k_t) = 0.0489k_t + 0.1604{k_t}^2 - 4.388{k_t}^3 \\ \qquad +16.638{k_t}^4 - 12.336{k_t}^5 \\ \qquad if \quad 0.004356 < k_n < 0.668 \\ k_t = \frac{k_n}{0.835} \quad if \quad 0.668 \leq k_n \leq 0.835 \end{cases} \tag{6}$$

- Quality envelope test was also applied to $k_n - k_t$ spaces between the years 2013 and 2016 because both DNI and GHI measurements exist in that period. Since DHI was not measured, $k_d - k_t$ envelopes were not created. It is a statistical outlier analysis and defining the boundary layers of envelopes depend on site-specific conditions [42]. Boundary layers are constructed using high quality and reliable ground measured data, and the nearest study was done in Cyprus by Pashiardis and Kalogirou [42]. They chose two sites which are Larnaca and Athalassa, and since Larnaca is a coastal region with similar solar radiation characteristics like at METU NCC, the following boundary layer equations created for Larnaca were used [42]:

$$f_{lower}(k_t) = 0.0441 - 0.752k_t + 1.480{k_t}^2 \tag{7}$$

$$f_{upper}(k_t) = -0.0705 + 0.6568k_t + 0.3814{k_t}^2 \quad (8)$$

- Gap filling can be done by estimations using the most correlated reference data from neighboring stations [57]. However, since measurements from a nearby alternative station are not available in our region, a spatial consistency test could not be done for our GHI & DNI measurements to estimate missing and erroneous data. Also, estimating solar radiation from nearby stations may not work on partly-cloudy days since weather conditions can change rapidly for each station [58]. As suggested by [59], up to 2 hours of missing data can be filled by linear interpolation.
- Before applying linear interpolation to missing hours, a replacement was done for the underestimated GHI measurements for 2014, 2015 and 2016. Both heat maps and daily total GHI graphs showed that GHI values are lower than or equal to DNI measurements in some periods; thus, the following criteria in equation (9) was applied to replace measured GHI with estimated GHI:

$$\begin{cases} use\ \ GHI_{estimated} \\ if\ GHI_{estimated} > GHI_{measured} \\ and\ if\ DNI * \cos\theta_z > 0.95 * GHI_{measured} \end{cases} \quad (9)$$

The second criterion was obtained from [43], and it comes from the relationship between the global, beam and diffuse radiation components, where DHI will always be greater than zero during daylight. Also, DHI will be minimum during clear-sky conditions so that the upper limit for beam component cannot exceed GHI multiplied by 0.95.

Missing GHI data was also estimated if DNI measurements were available. For example, 20 days of missing GHI data in October 2015 were estimated using DNI measurements and the Erbs model. The estimation procedure was applied for years 2014, 2015 and 2016. The remaining missing hours of GHI were then filled by linear interpolation if one or two hours are missing. As a result, the number of missing

hours was reduced from 269 to 51 between 2010 and 2016. In total, five days had both missing GHI and DNI values, and satellite-based data replaced them since it better tells us whether that day was clear-sky, partly cloudy or fully cloudy, rather than interpolating the whole day in between times.

Table 3.3 Days with missing GHI and DNI measurements. Missing hours were replaced by satellite-data.

Year	Month	Day
2013	July	30^{th}
2013	July	31^{th}
2014	May	31^{th}
2015	March	31^{th}
2016	September	30^{th}

Apart from these, lower-than-expected measurements were found in July 2011, and neither linear interpolation nor estimating GHI worked since there were no DNI records. Thus, lower-than-expected GHI measurements were replaced by satellite-based hourly GHI data between 188-220. days in 2011. According to the average daily total GHI values of measured and satellite-based data, average measured-to-satellite ratios were found as 0.9014, 0.8694 and 0.9576 throughout the whole year for 2010, 2012 and 2013, respectively. The mean measured-to-satellite daily GHI ratio was found as 0.933 with respect to 2010, 2012 and 2013, then a replacement was done for lower-than-expected GHI data in 2011 by multiplying satellite-based GHI with 0.933 for that time period only.

A summary of the detection of erroneous GHI, filling missing GHI and DNI data, and using estimated GHI at specific time periods can be seen at Figure 3.6. Applying this methodology to the measured GHI changed erroneous time periods; therefore, the term “constructed GHI” will be used, referring to the GHI after the quality assessment is done.

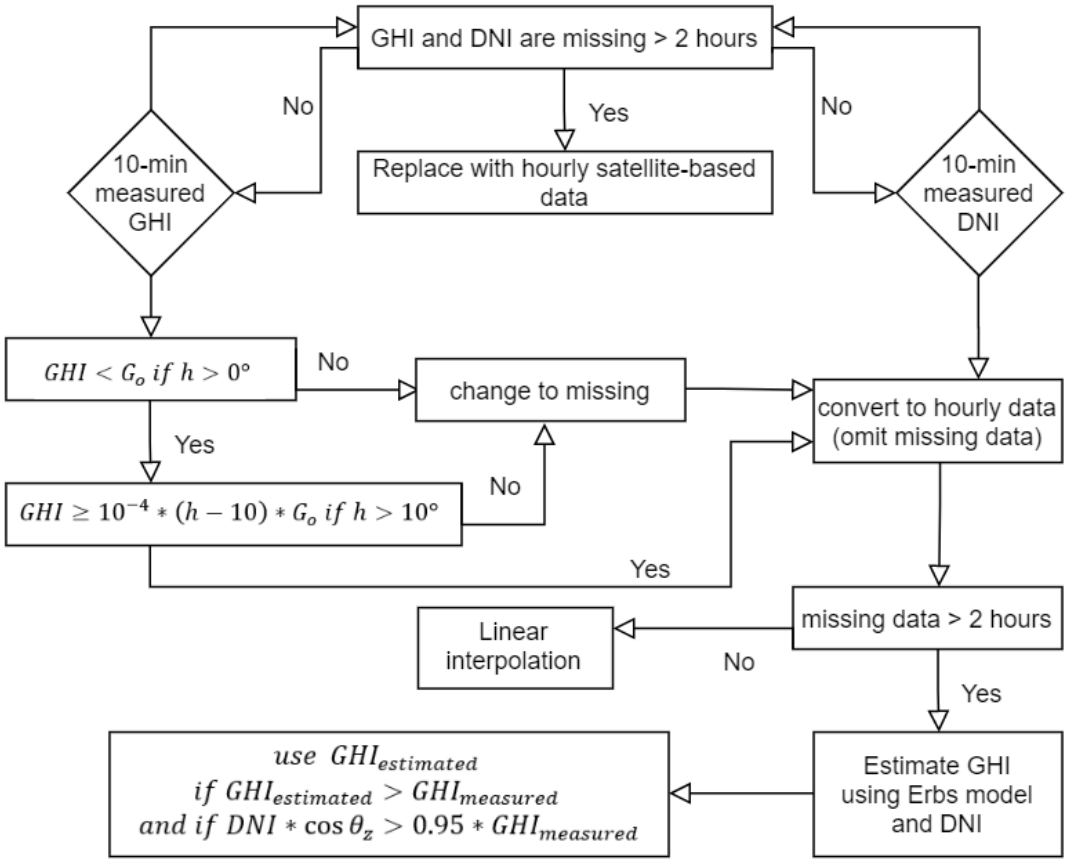

Figure 3.6. A flowchart of detecting erroneous GHI, filling missing data, and estimating GHI when it is needed.

- Ambient temperature measurements were recorded every 10 minutes from February 19, 2013, until March 25, 2018, as can be seen in Figure 3.7. Leap day in 2016 was removed, and only data recorded in 2014, 2015 and 2016 were taken to be used in solar PV energy production calculations since GTI estimation is available for that time period. Hourly missing data were filled by linear interpolation.

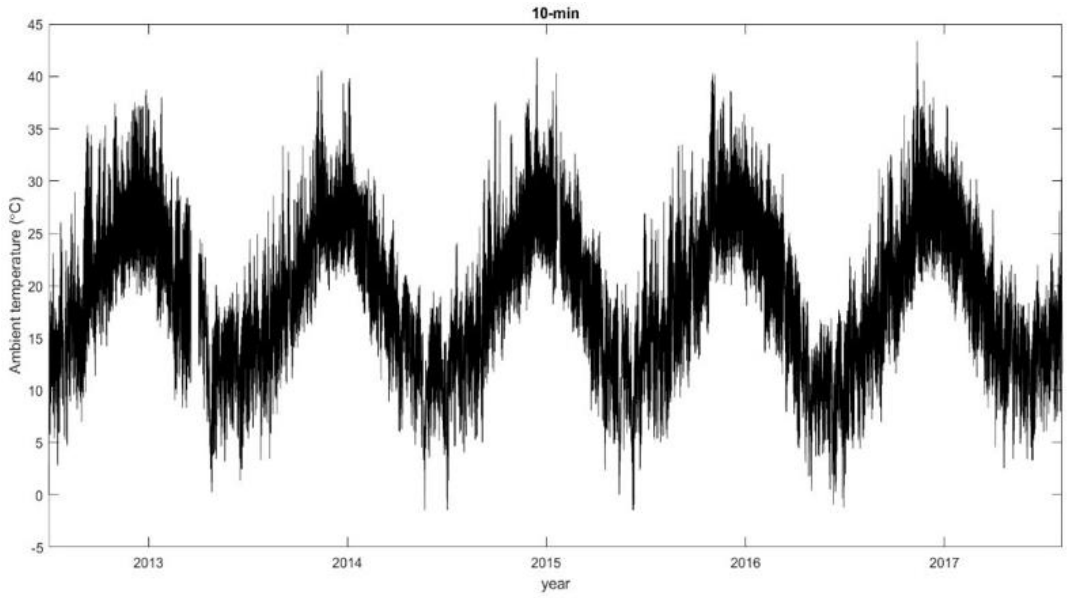

Figure 3.7. Time series of 10-minute measured ambient temperature between 2013 and 2017.

After all these adjustments, comparisons were made between measured, estimated, constructed and satellite-based data, using the relative root-mean-square error (rRMSE) formula in equation (10):

$$rRMSE = \frac{\sqrt{\frac{\sum_{i=1}^{n}\left(x_{estimated,i} - x_{measured,i}\right)^2}{n}}}{\bar{x}_{measured}} \quad (10)$$

3.2 Solar PV Energy Yield Estimation

The amount of energy output of a solar PV module is dependent on the geometrical relations between Sun, Earth and the module's surface where solar radiation reaches. Also, time is important in solar energy calculations, and solar time should be calculated, which is different from local time [19]. The following equation is used to calculate solar time [19]:

$$t_s = t_{std} + 4 \times (L_{st} - L_{loc}) + E \quad (11)$$

where t_{std} is local time, L_{st} is standard meridian, L_{loc} is the longitude of location, and E is the equation of time. These terms are calculated in equations 12-14 [19]:

$$L_{st} = \begin{cases} -(TZ) \times 15 & if\ TZ \leq 0 \\ 360 - (TZ) \times 15 & if\ TZ > 0 \end{cases} \quad (12)$$

$$L_{loc} = \begin{cases} L_{loc} & if\ West \\ 360 - L_{loc} & if\ East \end{cases} \quad (13)$$

$$E = 229.2 \times (0.000075 + 0.001868 \times \cos B - 0.032077 \times \sin B$$

$$-0.014615 \times \cos 2B - 0.04089 \times \sin 2B) \quad (14)$$

where B is a constant and calculated as follows [19]:

$$B = (n - 1) \times \frac{360}{365} \quad (15)$$

Solar time should be converted to angular form, which makes the hour angle [19]:

$$\omega = (t_s - 12) \times 15 \quad (16)$$

Apart from solar time, the position of the sun should also be found. Zenith angle is calculated as follows [19]:

$$\cos \theta_z = \cos \emptyset \cos \delta \cos \omega + \sin \emptyset \sin \delta \quad (17)$$

where $\emptyset$ is latitude, and δ is the declination angle which is calculated as follows [19]:

$$\delta = 23.45 \times \sin\left(\frac{360}{365} \times (284 + n)\right) \quad (18)$$

The solar azimuth angle is also needed and calculated as follows [19]:

$$\gamma_s = sign(\omega) \times \left|\cos^{-1}\left(\frac{\cos \theta_z \sin \emptyset - \sin \delta}{\sin \theta_z \cos \emptyset}\right)\right| \quad (19)$$

The PV module orientation should also be determined to optimize the energy output; thus, tilt (β) and surface azimuth angles (γ) should be optimized. Finally, the angle of incidence can be calculated as follows [19]:

$$\cos\theta = \cos\theta_z \cos\beta + \sin\theta_z \sin\beta \cos(\gamma_s - \gamma) \quad (20)$$

In this study, global tilted irradiation (GTI) was estimated using the isotropic sky-diffuse model proposed by Liu and Jordan, since it allows a simple calculation by not considering the circumsolar and horizon-brightening effects of DHI [19]:

$$GTI = DNI \times \cos\theta + DHI\left(\frac{1+\cos\beta}{2}\right) + GHI \times \rho \times \left(\frac{1-\cos\beta}{2}\right) \quad (21)$$

where θ is the angle of incidence, β is the surface tilt angle, and ρ is the surface albedo. Thus, GTI consists of beam, diffuse and reflected radiation components incoming to tilted solar panels. Surface albedo was assumed as 0.2, constant during a year. Apart from the isotropic sky-diffuse model, more detailed transposition models consider the circumsolar and horizon-brightening components of diffuse irradiation, such as Hay, Davies, Klucher, Reindl (HDKR) and Perez models [19]. HDKR model estimates GTI as follows [19]:

$$I_T = (I_b + I_d A_i) R_b + I_d(1 - A_i)\left(\frac{1+\cos\beta}{2}\right)\left[1 + f\sin^3\left(\frac{\beta}{2}\right)\right] + I\rho\left(\frac{1-\cos\beta}{2}\right) \quad (22)$$

where I_T, I_b, I_d and I are tilted, beam, diffuse and global horizontal irradiation, respectively. A_i is the anisotropy index and is calculated as follows [19]:

$$A_i = \frac{I_b}{I_o} \quad (23)$$

where I_o is the extra-terrestrial radiation on a horizontal surface. R_b is the geometric factor and is calculated as follows [19]:

$$R_b = \frac{\cos\theta}{\cos\theta_z} \quad (24)$$

where θ is the angle of incidence. Finally, f is the modulating factor which takes into account cloudiness, and is calculated as follows [19]:

$$f = \sqrt{\frac{I_b}{I}} \quad (25)$$

The most detailed estimation of GTI is found using the Perez model [19]:

$$I_T = I_b R_b + I_d(1 - F_1)\left(\frac{1+\cos\beta}{2}\right) + I_d F_1 \frac{a}{b} + I_d F_2 \sin\beta + I\rho\left(\frac{1-\cos\beta}{2}\right) \quad (26)$$

where F_1 and F_2 are circumsolar and horizon-brightness coefficients, respectively. The terms *a* and *b* account for the circumsolar radiation, and detailed information about these terms can be found in [19].

DHI can be calculated from the relationship between DNI and GHI [19]:

$$GHI = DNI \times \cos\theta_z + DHI \quad (27)$$

Annual energy production was calculated on an hourly basis, using the following equation [19]:

$$E_{PV} = \sum_{i=1}^{8760} \eta_{PV,i} \times GTI_i \times A_{PV} \times N_{PV} \quad (28)$$

where $\eta_{PV,i}$ is the PV module efficiency at i^{th} hour, A_{PV} is the PV module area and N_{PV} is the number of PV modules in the solar PV plant. PV module efficiency at i^{th} hour can be calculated from the following equation [19]:

$$\eta_{PV} = \eta_{PV,ref}\left[1 - \beta_t\left(T_{PV} - T_{ref,STC}\right)\right] \quad (29)$$

where $\eta_{PV,ref}$ is the reference PV module efficiency under standard test conditions (STC), β_t is the temperature coefficient, T_{PV} is the PV module temperature, and $T_{ref,STC}$ is the reference PV module temperature under STC. PV module temperature at i^{th} hour can be calculated from the following equation [19]:

$$T_{PV} = T_{ambient} + \left(T_{NOCT} - T_{ref}\right)\frac{GTI}{G_{ref}} \quad (30)$$

where $T_{ambient}$ is the ambient air temperature, T_{NOCT} is the nominal operating cell temperature, T_{ref} is the reference temperature under normal operating conditions, and G_{ref} is the reference irradiation under normal operating conditions. The input parameters used to calculate the solar PV energy yield can be found in Table 3.4.

After calculating the annual energy production, the final energy yield of a solar PV plant can be found as follows [19]:

$$Y_f = \frac{AEP}{Installed\ capacity} \tag{31}$$

where Y_f is the final energy yield in kWh/kWp, *AEP* is the annual energy production in kWh, and installed capacity of a solar PV plant is in kWp, which is 1000 kWp for the installed solar PV plant in METU NCC.

Table 3.4 Input parameters of the solar PV module [60].

Parameter	Symbol	Value	Unit
PV module area	A_{PV}	1.63	m^2
Number of PV modules	N_{PV}	4000	–
Reference PV module efficiency under STC	$\eta_{PV,ref}$	15.37	%
Temperature coefficient	β_t	0.0042	K^{-1}
Reference PV module temperature under STC	$T_{ref,STC}$	25	℃
Nominal operating cell temperature	T_{NOCT}	45	℃
Reference irradiation under normal operating conditions	G_{ref}	800	W/m^2
Reference temperature under normal operating conditions	T_{ref}	20	℃

Both ground-measured and estimated data, which were obtained by doing the quality assessment, were used to calculate the energy yield, and a summary of the methodology followed can be seen in Figure 3.8.

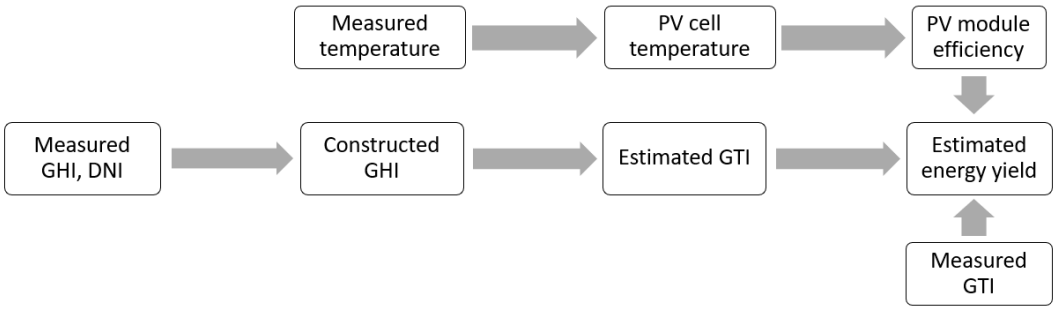

Figure 3.8. Summary of the procedure to find energy yield estimations using ground-measured data.

3.3 P50/P90 Analysis

An exceedance probability is the complementary value of a percentile, thus, 10^{th} percentile is the P90 value. In this study, the term "P" is used to denote P50 and P90 exceedance probabilities. Any POE value can be found from the inverse of a CDF, F(x), using the following equation:

$$POE = F^{-1}(x) \tag{32}$$

The empirical method is said to be the most direct application since it is based on concatenating data points with equal probability of occurrence without assuming a PDF [13], [23]. In this study, the empirical method was applied to find the POE values of GHI and AEP, considering that there may be outlier weather events that cause skewness in the data sets. Therefore, statistical uncertainties due to assuming a specific PDF are not included in the empirical results. SAM version 2020.2.29 was used to do a P50/P90 analysis, and a TMY simulation was done to compare the energy yield with the P50 value. SAM calculates the energy exceedance probability values using both the empirical method and the Normal (Gaussian) distribution assumption [23]. According to the Normal distribution, independent samples are normally distributed, and the following equations describe its PDF and CDF [22], [23]:

$$f(x) = \frac{1}{\sigma\sqrt{2\pi}} e^{-\frac{1}{2}\left(\frac{x-\mu}{\sigma}\right)^2} \tag{33}$$

$$F(x) = \frac{1}{2}\left[1 + erf\left(\frac{x-\mu}{\sigma\sqrt{2}}\right)\right] \tag{34}$$

where *erf* is error function, σ is the standard deviation, and μ is the mean of a sample. Assuming a Normal distribution for the long-term solar radiation dataset and the energy yield makes the P50 value mean, and P90 value can be calculated from the CDF of Normal distribution [22]:

$$P90 = \mu - 1.282 \times \sigma \tag{35}$$

At least ten years of weather data are required for the P50/P90 analysis in SAM to include the interannual variability of solar irradiation and obtain a representative CDF of the AEP. In addition, the most recent 10-year data is suggested to best predict the future GHI trend throughout the operational life of a PV plant [25]. Since the satellite-based data is available for the time period 2005-2016, 12 years of data were used in the simulation. However, including the recent years' data is of interest since the interannual variability of GHI directly depends on the length of the time period [32]. The interannual variability can be calculated with the coefficient of variation (COV) using the following equations, which are suggested by [4]:

$$COV = \frac{s}{\bar{x}} \tag{36}$$

$$s = \sqrt{\left(\frac{1}{N}\sum_{i=1}^{N}(x_i - \bar{x})^2\right)} \tag{37}$$

where s is the standard deviation, x_i is the individual value and $\bar{x}$ is the mean value of a sample. Here, N is the number of years for the time period of 2005-2016. Throughout the simulations, DNI and GHI datasets were used as the irradiance data from the weather files. Surface albedo was assumed to be constant which is 0.2. To convert irradiation components into POA irradiation on an inclined surface, SAM uses three different transposition models: the isotropic, HDKR, and Perez models. Therefore, results were obtained for each model to see the effects of transposition models on the POE values. In Table 3.5, SAM input parameters of the installed solar PV plant in METU NCC are shown, in which both specifications of the installed solar PV module and inverter are provided. Since SAM does not allow multiple maximum power point tracking (MPPT) inputs for inverters if it is a large-scale PV system, single MPPT input was assigned, although the number of MPPT input is 2 for the inverter model in the PV plant at METU NCC.

In Table 3.6, PV system losses, which are applied as default values, are given. Shading, reflection, soiling and snow cover correspond to irradiance losses that reduce the POA irradiance on PV modules, and the annual average values are presented. Here, the nameplate loss refers to the degradation of PV modules after

being exposed to sunlight, and the value was obtained from the manufacturer's datasheet [60]. However, P50/P90 analysis does not allow to consider the annual degradation rate of the PV system throughout its operational life since calculations are done only for the first year; thus, -0.48% degradation rate per year that is provided in the datasheet is not included in the calculation of AEP. On the other hand, the PV module efficiency deviates from the standard test condition (STC) since it depends on the solar irradiation, ambient temperature and the wind speed [33], the average deviation from STC was obtained for the PV modules. Other losses such as diodes and connections, AC/DC wiring, inverter power consumption and inverter efficiency loss are for AC and DC losses. Grid limits such as interconnection to the grid and curtailments were not considered in this study.

Table 3.5 Solar PV system inputs used in SAM software.

Parameter	Value
Rated power	1 MWp
Tilt angle	30º
Surface azimuth angle	0º
Tracking	Fixed
PV module	AC-250P/156-60S
PV technology	multi-c-Si
NOCT	45.8ºC
Temperature correction	NOCT method
PV module conversion efficiency	15.41%
DC to AC ratio	1
Mounting standoff	ground/rack mounted
PV module area	1.623 m^2
Total module area	6492 m^2
Ground coverage ratio	0.4
Number of modules	4000
Inverter	STP 25000TL-30
Inverter size	25 kW
Manufacturer's inverter efficiency	98.30%
Number of MPPT inputs	2
Number of inverters	40

Table 3.6 Solar PV system losses used in SAM software.

Losses	(%)
Shading	-2.2
Soiling	-2
Reflection	-2.5
Snow	0
Module mismatch	-2
Nameplate	-3
PV module deviation from STC	-5
Diodes and connections	-0.5
DC wiring	-2
AC wiring	-1
Inverter power consumption	-1
Inverter efficiency loss	-1.75
Inverter power clipping	0
Transformer & transmission	0
Availability & curtailment	0

3.4 Stochastic Simulation

Since estimating the long-term energy yield of solar PV includes many assumptions, such as modeling equations and losses, the effect of the uncertainty of each input on the energy output should be investigated. In addition, there can be correlations between the inputs. Generally, stochastic modeling is done by defining a probability distribution for each source of uncertainty, and many samples are created with respect to the defined distributions of inputs, then, many possible outputs are calculated according to the samples. This method allows us to obtain a range of the expected output, for example, energy yield and the LCOE. Furthermore, a short-term dataset with less than ten years can be used to obtain P50 and P90 values because creating the samples enables new possible inputs for the weather dataset. Using longer datasets will make the results more realistic in the long term since the interannual variability of GHI changes according to the selected time period.

As a part of this study, the exceedance probabilities of the energy yield and the LCOE are found using the empirical method and the Normal distribution assumption. The results are also compared with TMY results. For the energy yield, a photovoltaic model without financial analysis is used in SAM; also, energy yield is estimated using the basic equations and the same weather datasets in custom codes. By doing so, the deviation of results can be quantified between using a simple model and modeling software. Besides, the LCOE is calculated using an equation and the energy yield results obtained from SAM calculations. Other inputs are assumed according to the literature and best practices. Thus, the LCOE variations can be determined according to different energy yield estimations.

In addition to these, a stochastic simulation is done in SAM software (version 2020.2.29), which uses the Latin Hypercube Sampling (LHS) method in order to create many samples, which is like Monte Carlo Simulation (MCS) [61]. Basically, the difference is that the LHS method generates near-random samples, whereas MCS generates random samples. The procedure of doing a stochastic simulation in SAM follows these steps:

- Defining input variables and their probability distributions
- Defining correlations between inputs, if there is any
- Choosing the output(s)
- Enabling weather file analysis for either GHI or DNI, if there are multiple weather files
- Defining the number of samples
- Computing the samples that will be used in the simulations
- Running simulations

Enabling weather file analysis is important because the interannual variability of GHI can also be considered by this way. In this study, satellite-based data (PVGIS-SARAH) was used with 12-year weather data for the time period of 2005-2016. Besides, the number of samples can be chosen by the user; however, there should be an optimum point at which the run-time will not take a long time, and the confidence

level of the outputs will be adequate. Thevenard and Pelland [26] showed in their study that computing 100 samples could give reliable results in less than 10 minutes. In Figure 3.9, a screenshot of the stochastic simulation tools which are used in this study can be seen. The input variables and assumed distributions can also be found in Table 3.7. UserCDF is defined by SAM for the sky diffuse model, temperature correction method and self-shading loss, which does not allow to choose another distribution. Other variables are assumed to be normally distributed, and their standard deviations are created by SAM, whereas the mean values have been assumed by the user previously. Here, it is important to note that SAM does not allow to choose and specify an uncertainty distribution for the soiling loss, which is assumed as 2% for the average annual soiling loss in the losses. Thus, the uncertainty related to dirt and soiling is not analyzed in detail in this study.

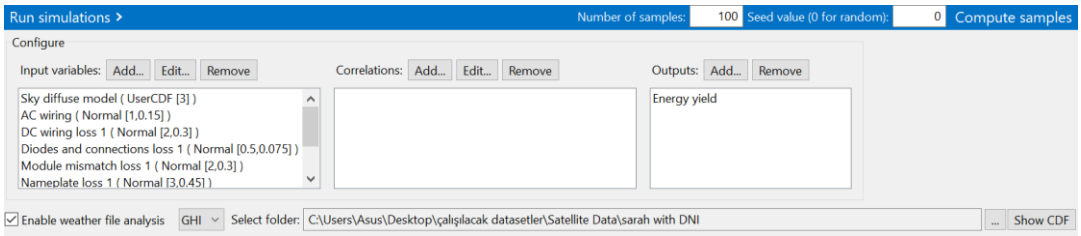

Figure 3.9. Stochastic simulation tools in SAM software.

Table 3.7 The input variables with their assumed distributions in the simulations with no financial model. Mean and standard deviations are shown in percentage.

Input variable	Assumed distribution	Mean (%)	Standard deviation (%)
Sky diffuse model	userCDF (Isotropic, HDKR, Perez)	–	–
Temperature correction method	userCDF (NOCT, heat transfer)	–	–
Self-shading loss	userCDF (None, standard, thin film)	–	–
AC wiring loss	Normal	1	0.15
DC wiring loss	Normal	2	0.3
Diodes & connection loss	Normal	0.5	0.075
Module missmatch loss	Normal	2	0.3
Nameplate loss	Normal	3	0.45

The stochastic simulation was then done for a financial model, which is chosen as PV LCOE Calculator to simplify the financial parameters used in SAM. By doing

so, both energy yield and LCOE can be chosen as output in the simulation. Other input variables are also added to previously mentioned inputs, which can be seen in Table 3.8.

Table 3.8 The input variables with their assumed distributions in the simulations with the financial model, PV LCOE Calculator.

Input variable	Assumed distribution	Mean	Standard deviation
Sky diffuse model	userCDF (Isotropic, HDKR, Perez)	–	–
Temperature correction method	userCDF (NOCT, heat transfer)	–	–
Self-shading loss	userCDF (None, standard, thin film)	–	–
AC wiring loss	Normal	1%	0.15%
DC wiring loss	Normal	2%	0.30%
Diodes & connection loss	Normal	0.5%	0.08%
Module missmatch loss	Normal	2%	0.30%
Nameplate loss	Normal	3%	0.45%
Capital Cost	Normal	1880 $/kW	282 $/kW
Annual fixed operating cost	Normal	15 $/kW	5 $/kW
Fixed charge rate	Normal	0.098	0.0147

3.5 Uncertainty Analysis

There are several sources of uncertainties when calculating a solar PV plant's annual energy production, such as data accuracy, energy modeling assumptions, and other sources of error [25]. In this study, uncertainty components can be classified as data uncertainty (accuracy of the satellite-based data used), converting GHI to POA irradiance (transposition models), the interannual variability of solar irradiation, uncertainties due to dirt, soiling, shading, reflection and other sources of error. According to the propagation of error, a function $f(x_1, \dots, x_n)$ has an uncertainty as,

$$dq = \sqrt{\left(\frac{\partial q}{\partial x_1} dx_1\right)^2 + \cdots + \left(\frac{\partial q}{\partial x_n} dx_n\right)^2} \tag{38}$$

Thus, considering that the function is the annual energy production,

$$AEP = \sum_{i=1}^{8760} \eta_{PV,ref} A_{PV} N_{PV} GTI_i \left[1 - \beta_t \left(T_{a,i} - T_{ref} + \left(NOCT - T_{ref}\right) \frac{GTI_i}{G_{ref}}\right)\right] \tag{39}$$

where $\eta_{PV,ref}, A_{PV}, N_{PV}, \beta_t, T_{ref}, NOCT$ and G_{ref} are constant parameters. Then, the AEP can be written as,

$$AEP = f(G_T, T_a) \tag{40}$$

which is a function of GTI and ambient air temperature. The uncertainty of AEP can be written as,

$$dAEP = \sqrt{\left(\frac{\partial AEP}{\partial GTI} dGTI\right)^2 + \left(\frac{\partial AEP}{\partial T_a} dT_a\right)^2} \tag{41}$$

where GTI includes the interannual variability of GHI, uncertainty coming from converting GHI to POA (transposition model), and the accuracy of a chosen dataset for a specific site. In addition, losses due to dirt, soiling, shading and reflection put additional uncertainty to global tilted irradiation (GTI). On the other hand, ambient temperature variability can be considered in other sources of error. If all uncertainty components are independent, the overall uncertainty of AEP can be found by the rule of squares method [26]:

$$\sigma_{overall} = \sqrt{(\sigma_{data})^2 + (\sigma_{POA})^2 + (\sigma_{interannual})^2 + (\sigma_{dirt})^2 + (\sigma_{other})^2} \tag{42}$$

3.6 Economic Analysis

In this study, the effects of the interannual variability of GHI, hence, the AEP impact on the LCOE was investigated using the empirical method of the P50/P90 analysis. Thus, it is aimed to find the non-exceedance probabilities of LCOE according to the exceedance probabilities of AEP since LCOE decreases as the AEP increases. All the parameters, except AEP, are kept constant to investigate the effect of AEP on LCOE. Also, any incentives, subsidies and taxes are assumed as zero. The solar PV system's residual value is not also considered since the operational lifetime is expected to be 25 years.

Since the LCOE is calculated for an energy project's whole operational lifetime, total electricity produced should be found considering the system degradation rate (SDR),

which is mainly affected by the solar PV module performance [62]. In the manufacturer's datasheet for solar PV modules, the performance linearly decreases from 97 to 85 percent in 25 years; thus, the annual SDR is guaranteed as 0.48% per year [60]. Hence, the LCOE formula was modified to account for the PV system degradation rate over the project's lifetime [62], [63]:

$$LCOE = \frac{C_0 + \sum_{i=1}^{t} \frac{M_i}{(1+r)^i}}{\sum_{i=1}^{t} \frac{(AEP_i) \cdot (1-SDR)^i}{(1+r)^i}} \quad (43)$$

where C_0 is the initial investment cost, M_i is the annual total O&M cost, r is the annual discount rate, t is the project lifetime, AEP is the first-year electricity generation and SDR is the PV system annual degradation rate.

Financial assumptions of the 1 MW solar PV plant in METU NCC can be seen in Table 3.9. Specifically, the initial investment and O&M costs are assumed from the Transparent Cost Database [64] for 2016, when the solar PV plant is installed. Further information about the historical and future trends of these costs can be found in Figures 3.10 and 3.11.

Table 3.9 Financial assumptions and parameters used in the LCOE formula of solar PV.

Parameter	Value	Unit	Ref.
Initial investment cost	1880	USD/kW	[64]
Annual total O&M cost	15	USD/kW	[64]
Annual discount rate	9	%	[17], [47]
Project lifetime	25	years	[60]
PV system annual degradation rate	0.48	%	[60]

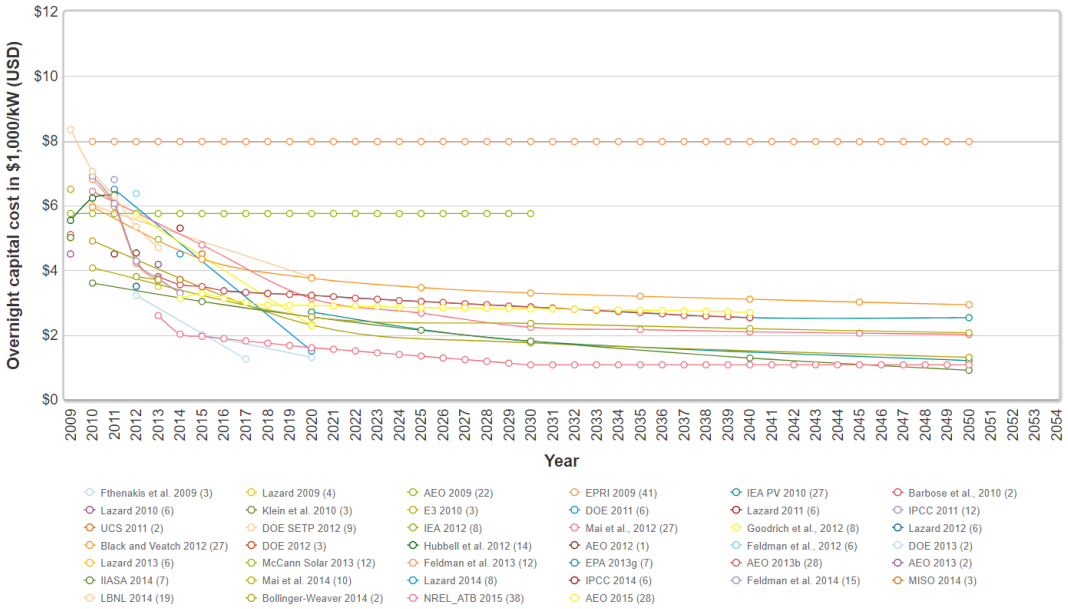

Figure 3.10. Historical and projection data trends for the overnight capital cost of solar photovoltaics. Adapted from [64].

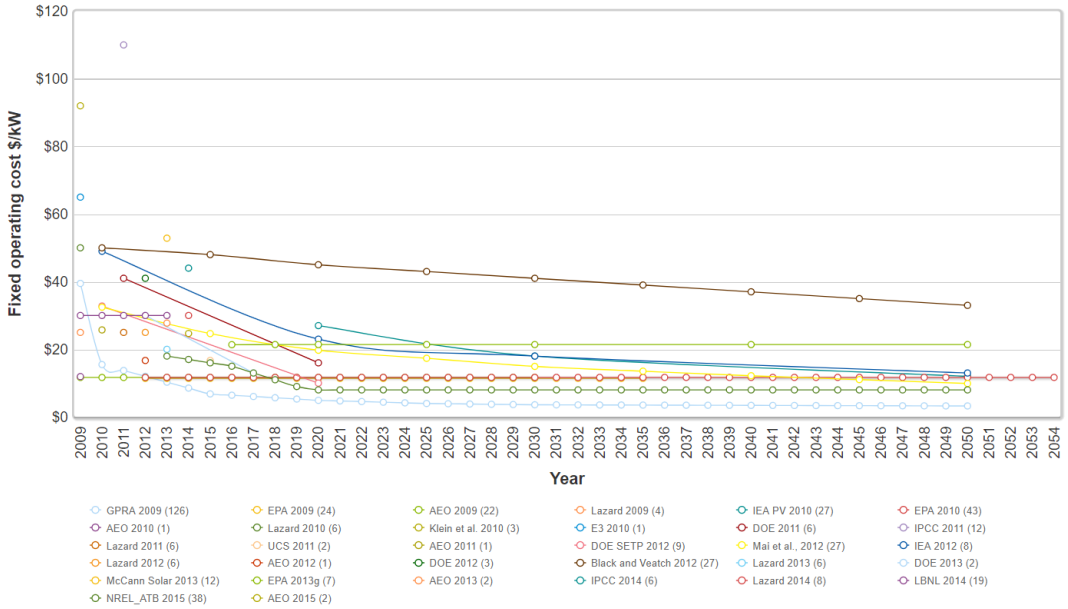

Figure 3.11. Historical and projection data trends for the fixed operating cost of solar photovoltaics. Adapted from [64].

In addition to this, SAM software is also used to calculate LCOE. The simple PV LCOE Calculator is chosen to keep the financial parameters simple, and the following equation is used in SAM:

$$LCOE = \frac{(FCR)(TCC)+FOC}{AEP} + VOC \quad (44)$$

where FCR is the fixed charge rate, TCC is total capital cost in $/kW, FOC is fixed annual operating cost in $/kW/yr, VOC is the variable operating cost (zero for solar PV), and AEP is the annual energy production in kWh/yr. The fixed charge rate was chosen as 0.098 by SAM, and it is affected by many parameters such as the inflation rate, project term debt, tax rate, interest rate and analysis period of the project. To obtain similar results, VOC is kept zero, TCC is assumed as 1880 $/kW, and FOC is assumed as 15 $/kW/yr. This method is said to be suitable for preliminary analyses and to see the market trends of solar PV.

CHAPTER 4

RESULTS AND DISCUSSION

4.1 Data Analysis and Quality Assessment

Figures 4.1-4.4 show both measured and estimated hourly data points, in addition to the boundary layers of quality control envelopes, where the lower curve is made by $f_{lower}(k_t)$ and upper curve is made by $f_{upper}(k_t)$. There might be a calibration error for measured GHI since most data is out of the quality envelope limits; in addition, estimated data do not represent measured values. It is understood that GHI measurements were underestimated in the last three years by a factor of 1.75 on average. Although the second half of 2013 was tested, the measured data is almost consistent with the limits.

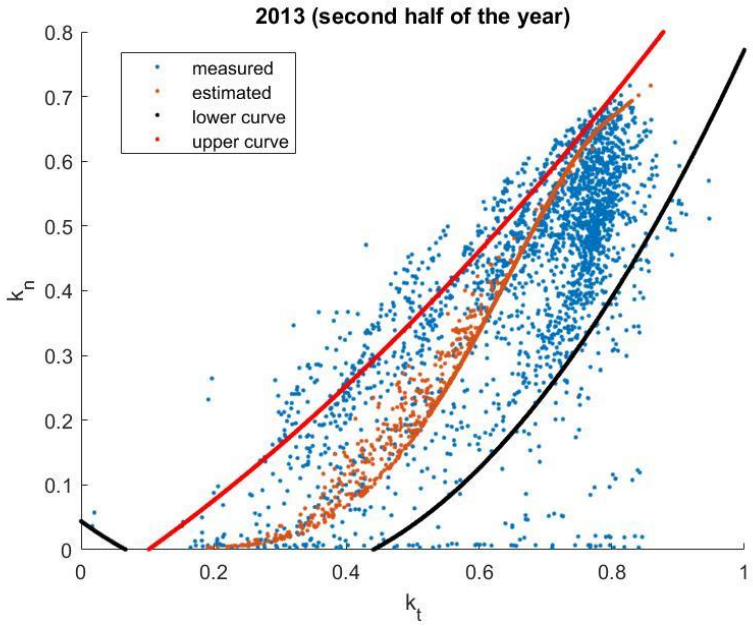

Figure 4.1. $k_n - k_t$ quality envelopes for measured and estimated data with upper and lower boundary layers in 2013.

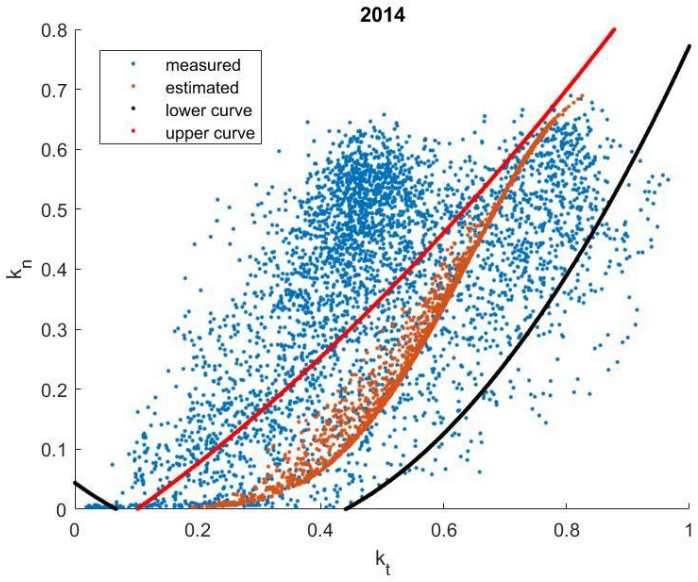

Figure 4.2. $k_n - k_t$ quality envelopes for measured and estimated data with upper and lower boundary layers in 2014.

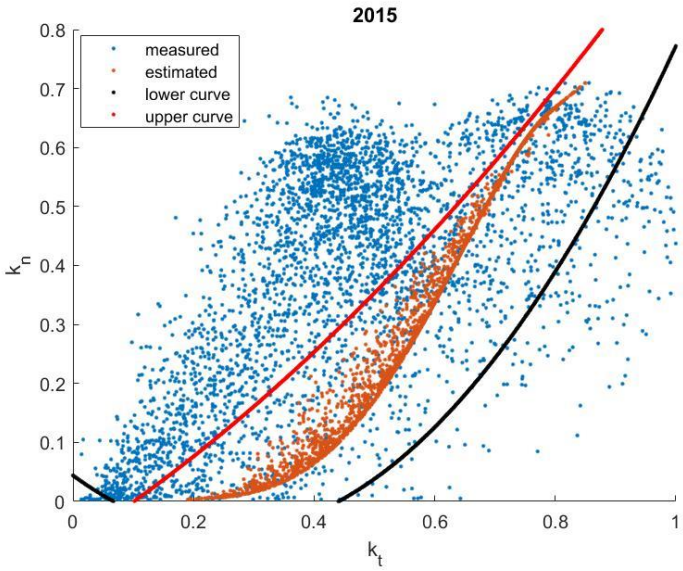

Figure 4.3. $k_n - k_t$ quality envelopes for measured and estimated data with upper and lower boundary layers in 2015.

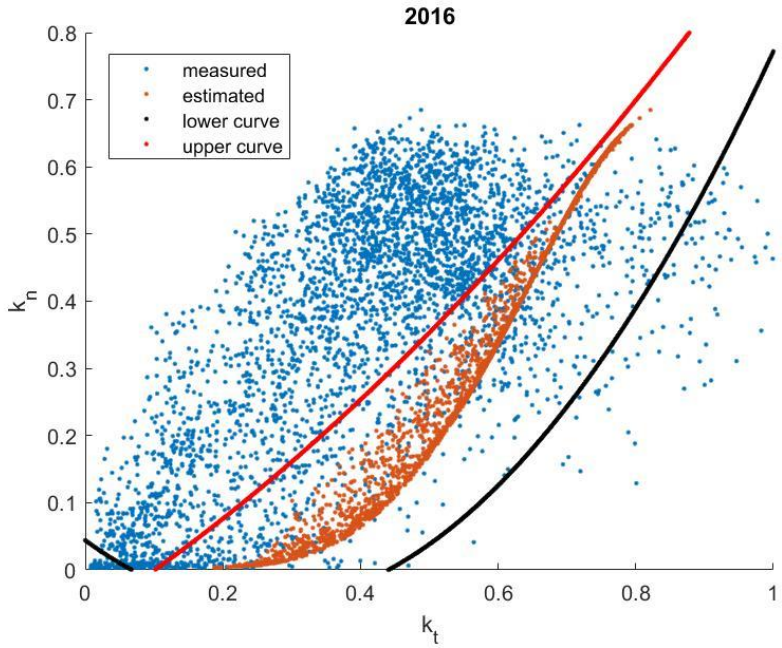

Figure 4.4. $k_n - k_t$ quality envelopes for measured and estimated data with upper and lower boundary layers in 2016.

After doing the quality assessment, GHI data were estimated and constructed according to the methodology explained in Section 3.1.2. The methodology was applied to the specific parts of data, which are shown in boxes in Figures 4.5, 4.7, 4.9 and 4.11. The aim of choosing specific parts of data is to construct hourly GHI only when a significant difference with the daily total GHI of satellite-based data exists. Therefore, the boxes are specified manually, and only those periods in the boxes are constructed for the years of 2011, 2014, 2015 and 2016. No significant difference is found according to RMSE results of GHI for the years 2010, 2012 and 2013. By doing so, it is also aimed not to change ground-measured data unless it is suspicious since it is known from the validation studies that satellite-based GHI can be overestimated by about 3.6% compared to ground measurements. In Figures 4.5-4.12, the changes done to the ground-measured GHI data can be seen, compared with E.T. radiation and satellite-based GHI.

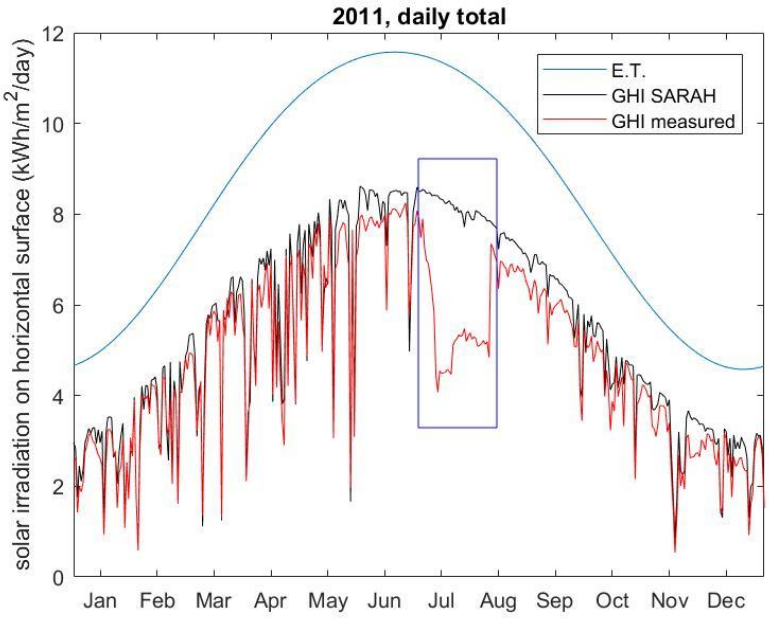

Figure 4.5. A comparison of daily total E.T., satellite-based GHI (SARAH) and ground-measured GHI before the adjustment done to selected time period shown in rectangle, in 2011.

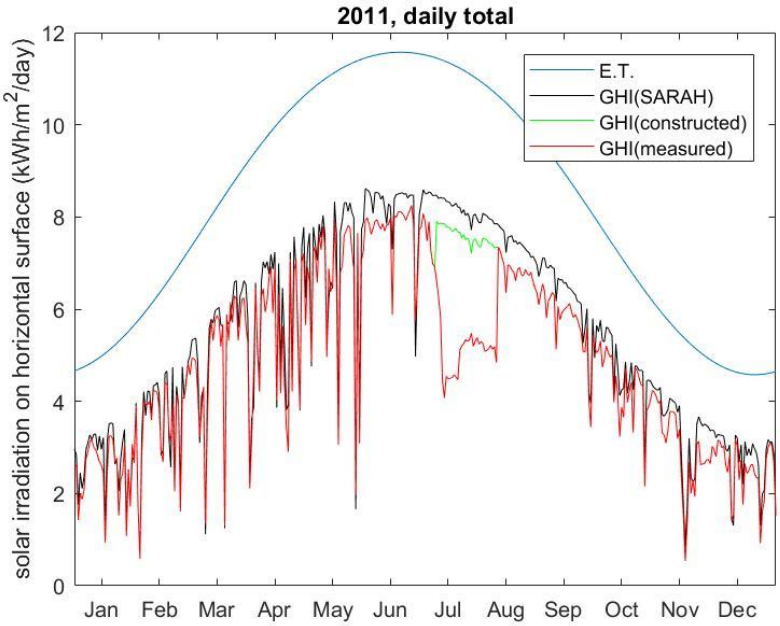

Figure 4.6. A comparison of daily total E.T., satellite-based GHI (SARAH), constructed GHI and ground-measured GHI after the adjustment, in 2011.

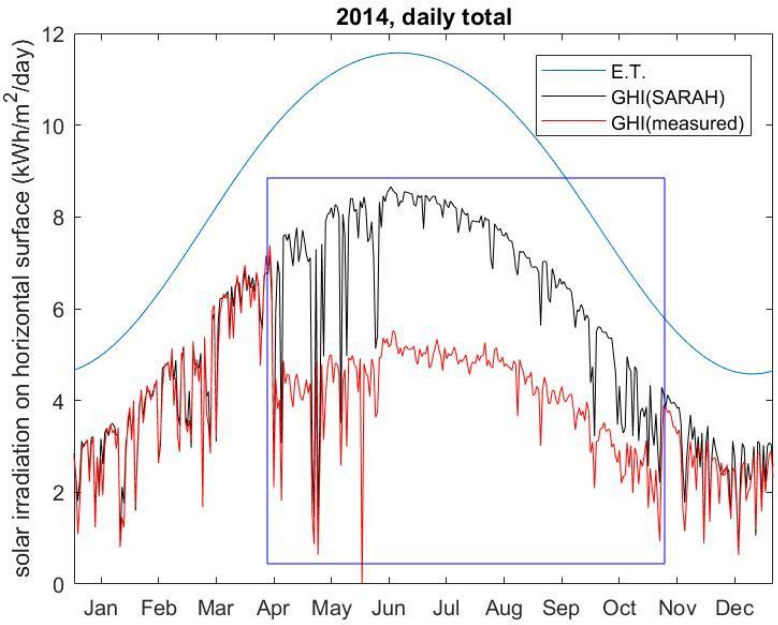

Figure 4.7. A comparison of daily total E.T., satellite-based GHI (SARAH) and ground-measured GHI before the adjustment done to selected time period shown in rectangle, in 2014.

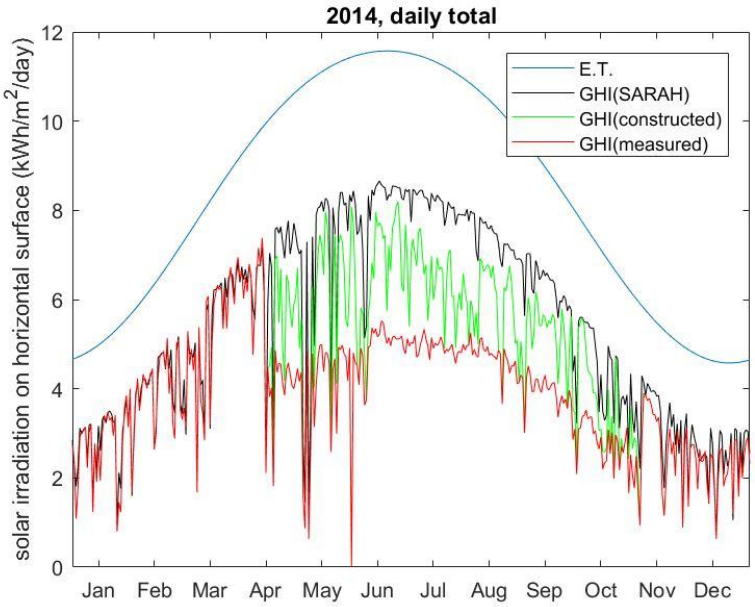

Figure 4.8. A comparison of daily total E.T., satellite-based GHI (SARAH), constructed GHI and ground-measured GHI after the adjustment, in 2014.

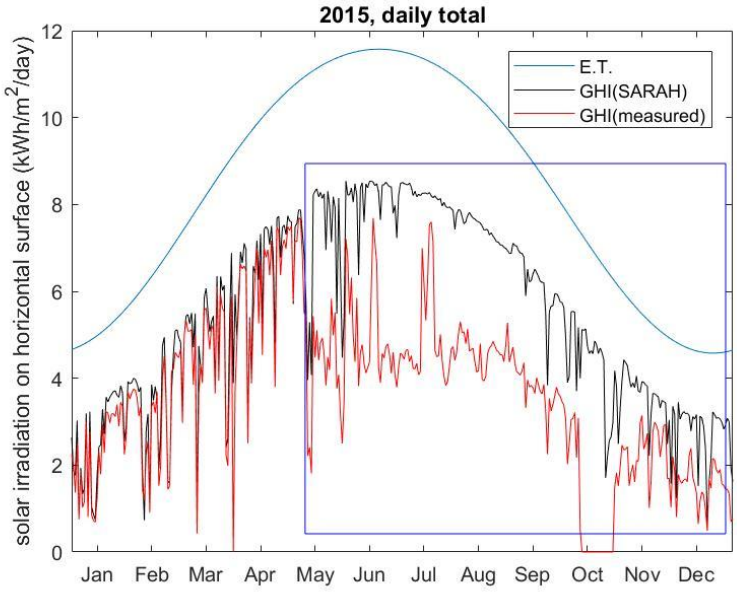

Figure 4.9. A comparison of daily total E.T., satellite-based GHI (SARAH) and ground-measured GHI before the adjustment done to selected time period shown in rectangle, in 2015.

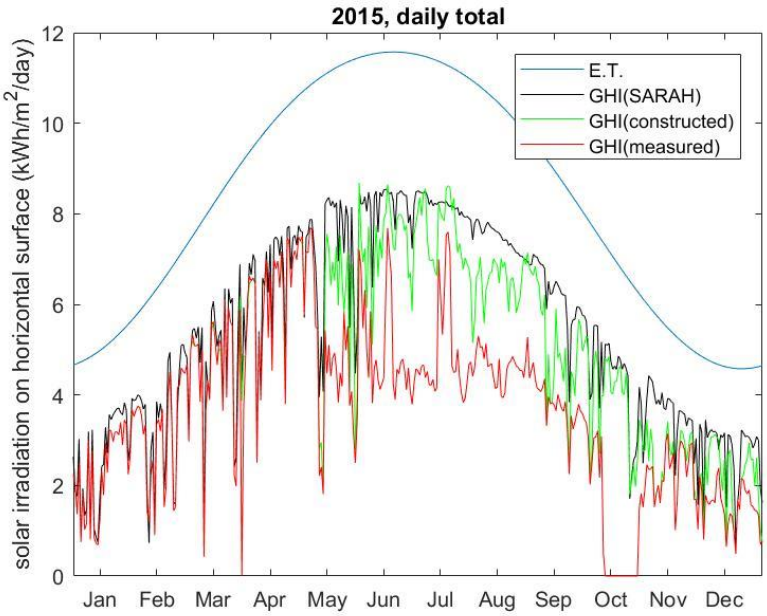

Figure 4.10. A comparison of daily total E.T., satellite-based GHI (SARAH), constructed GHI and ground-measured GHI after the adjustment, in 2015.

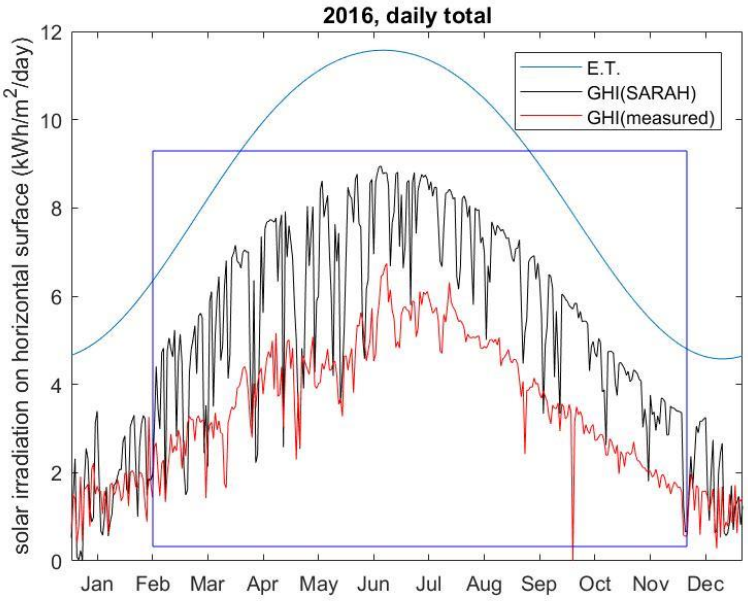

Figure 4.11. A comparison of daily total E.T., satellite-based GHI (SARAH) and ground-measured GHI before the adjustment done to selected time period shown in rectangle, in 2016.

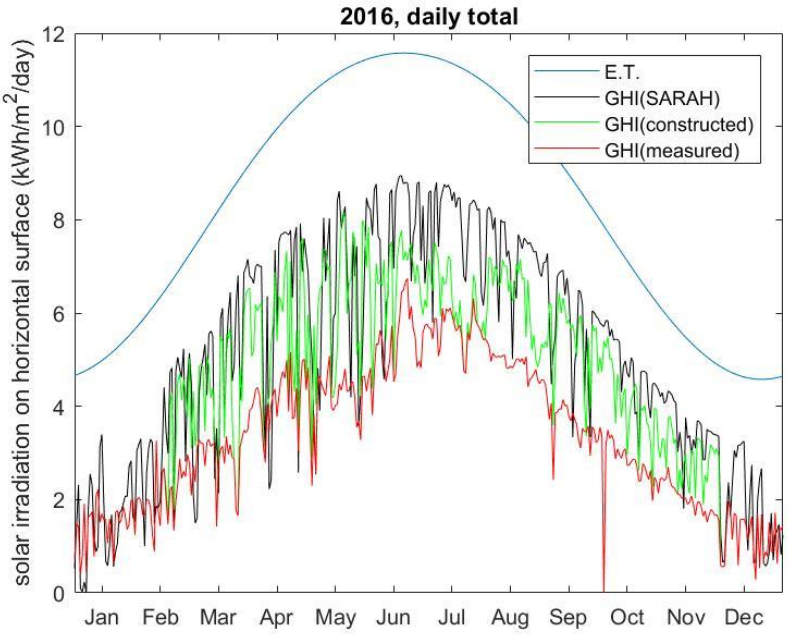

Figure 4.12. A comparison of daily total E.T., satellite-based GHI (SARAH), constructed GHI and ground-measured GHI after the adjustment, in 2016.

Relative root-mean-square error (rRMSE) is calculated to compare ground-measured and satellite-based data. In Table 4.1, RMSE results of GHI and DNI data can be seen. First, the results are found for the measured GHI values, and the rRMSE significantly increased after the year 2013. Then, the estimated GHI are calculated using the available DNI data and Erbs model. It is found that rRMSE values were reduced by a factor of 4 on average. Finally, new GHI values are constructed using both measured and estimated GHI, and the average RMSE for the time period 2010-2016 reduced from 34.63% to 14.02%. Monthly mean daily total GHI values are also found from the newly constructed GHI data and comparing them with monthly mean satellite-based GHI data resulted in 11.22% RMSE on average. Comparing the annual mean daily total GHI data of satellite-based and ground-measured data from 2010 to 2016 gave a relative RMSE of 8.78%.

Table 4.1 Relative root mean square error (rRMSE) of measured GHI, measured DNI, estimated GHI and constructed GHI with respect to satellite-based GHI and DNI data, obtained from daily total & monthly mean daily total DNI and GHI (kWh/m^2/day) for each year. DNI is available after June 2013.

	Daily total				Monthly mean
Year	Measured GHI (%)	Measured DNI (%)	Estimated GHI (%)	Constructed GHI (%)	Constructed GHI (%)
2010	14.28	–	–	14.28	10.39
2011	21.36	–	–	9.34	7.82
2012	8.75	–	–	8.75	6.62
2013*	18.32	–	9.04	2.80	5.91
2014	53.09	32.11	15.51	20.61	18.01
2015	61.97	23.15	11.95	16.40	13.71
2016	64.66	43.00	22.05	25.98	16.10
average	34.63	32.75	14.64	14.02	11.22

*Estimated and constructed GHI in 2013 are calculated starting from June.

4.1.1 Validation of Ground Measurements

RMSE results show that ground-measured GHI has some inaccuracies since the error increased from 18.32% in 2013 to 64.66% in 2016. In fact, it was aimed to find any biases or systematic errors in satellite-based data; however, this was not possible due to the lack of high-quality ground-measured data. Thus, the satellite-based data was used to compare with ground measurements between 2010 and 2016. Applying the quality control tests also consolidated the lower-than-expected GHI values in some periods. An estimation was then done using the inversion of the Erbs model [56] and measured DNI data. Instead of replacing the lower-than-expected GHI data with estimated GHI directly, a method was followed which has two conditions. If the estimated GHI is higher than the measured GHI, and if the measured beam component is higher than the measured GHI, it is multiplied by 0.95, as explained in Section 3.1.2. Therefore, the estimated GHI data was only used if these two conditions are valid, and the constructed GHI was obtained. Indeed, this method can only estimate the actual GHI data, and it also has some sources of error, such as using the measured DNI data and Erbs model. Still, DNI measurements helped us understand how reliable are GHI measurements; also, we were able to estimate GHI by using the relationship between clearness index and beam transmittance in the Erbs model. In Figures 4.13 and 4.14, heat maps of the measured and constructed GHI can be seen. Changes were made in some periods of 2011, 2014, 2015 and 2016.

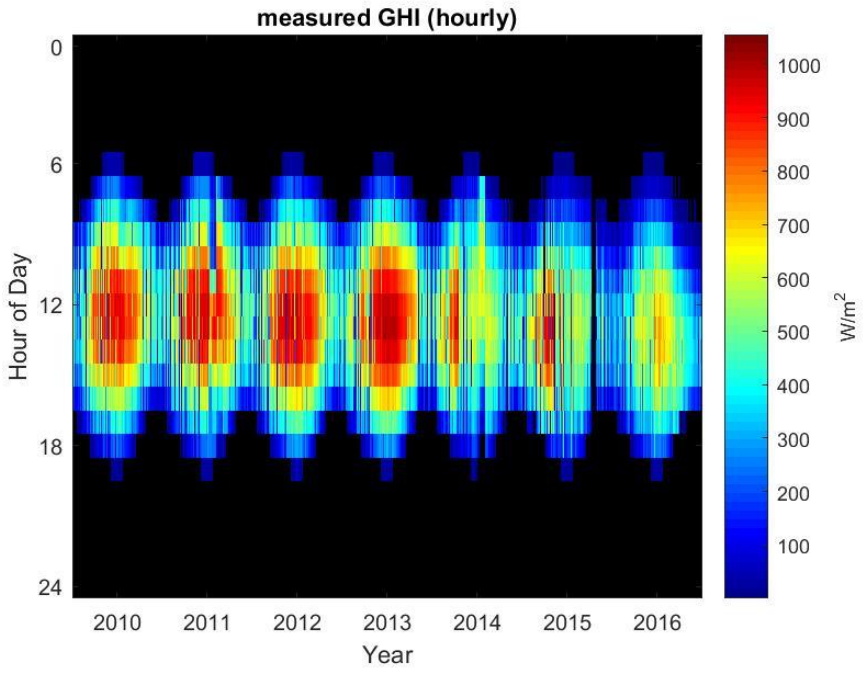

Figure 4.13. Heat map of hourly measured GHI between 2010 and 2016.

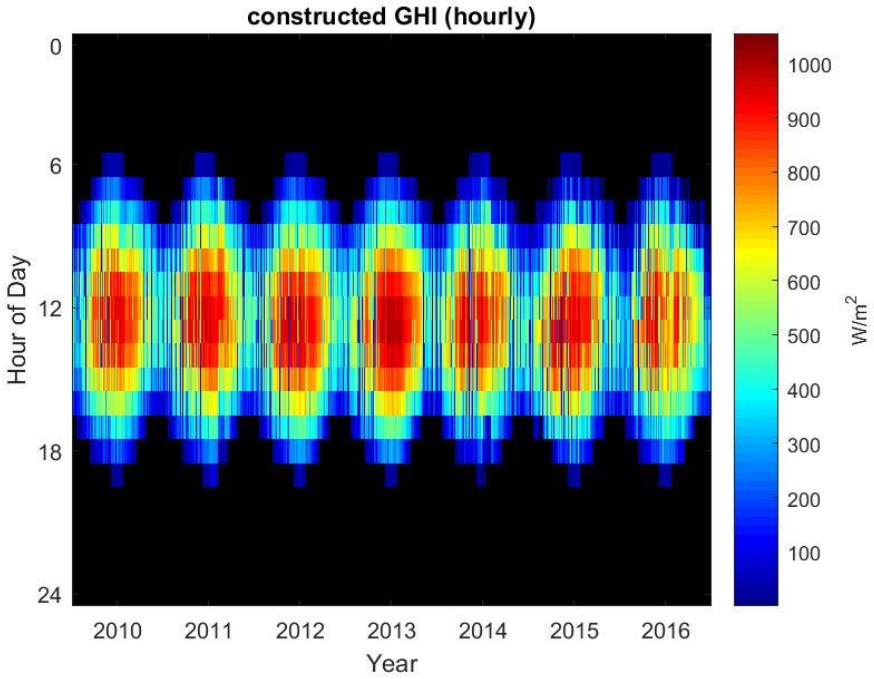

Figure 4.14. Heat map of hourly constructed GHI between 2010 and 2016.

To validate the method used to construct GHI data, different time periods were selected from 2013 and 2015. In 2013, DNI was available starting from June; thus, the remaining last 214 days of 2013 were used to estimate and construct GHI. Previously, it was found that GHI measurements of 2013 were in the range of quality envelope, and the RMSE of measured GHI with respect to satellite-based GHI was 18.32%. Thus, it can be said that GHI data is reliable in 2013 compared to years 2014, 2015 and 2016, so a comparison of constructed and measured GHI data can be done to validate the method. In Table 4.2, the RMSE values are given in percentage for daily total GHI data. It can be understood from the results that the method replaced a very small amount of data to construct GHI since RMSE was found as 0.06%. On the other hand, the first 130 days of 2015 was selected to apply the method, which was found to be close to satellite-based GHI, and the method had not been applied to that period previously. Similarly, an RMSE of 5.20% was found for constructed GHI data, and the changes can be seen in Figures 4.15 and 4.16. However, the period of October was not considered when calculating RMSE values since there were no GHI measurements during that time as the pyranometer was sent out for calibration. It can be said that the estimation method gave smaller errors when compared to the results of satellite-based data, and the range is about 5% with respect to measured data. Therefore, it can be assumed that this method is validated against reliable measured GHI data, chosen from 2013 and 2015. It should also be noted that 344 days were used to apply the method, and only 21 days in May are unknown in terms of the validity of the construction of GHI data.

Table 4.2 Relative RMSE values of estimated, constructed and satellite-based GHI with respect to measured GHI, for selected time periods in 2013 and 2015.

RMSE with respect to daily total measured GHI data	2013 (last 214 days)	2015 (first 130 days)
estimated GHI (%)	6.37	1.98
constructed GHI (%)	0.06	5.20
satellite-based GHI (%)	2.94	9.53

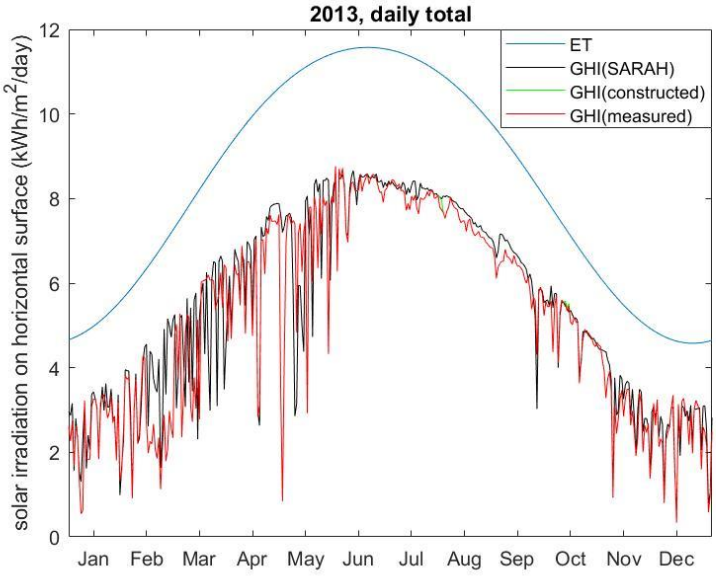

Figure 4.15. Comparison of constructed and measured GHI with satellite-based data in selected periods of 2013, for the validation of the method.

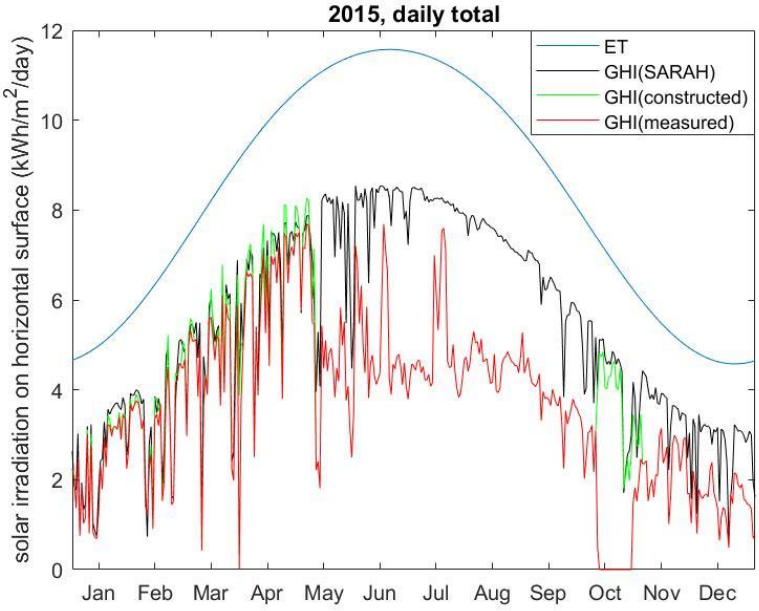

Figure 4.16. Comparison of constructed and measured GHI with satellite-based data in selected periods of 2015, for the validation of the method.

Comparing daily total DNI measurements with satellite-based DNI gave 33% RMSE on average for the last three years. This error might come from the fact that satellite-based data covers up to 5 km area as spatial resolution; also, hourly data is calculated based on one satellite image per hour, as time resolution [54]. Therefore, DNI measurements from the ground can reflect the actual changes in cloud cover and solar radiation. Comparisons of ground-measured and satellite-based DNI data for 2014, 2015 and 2016 can be seen in Figure 4.17, 4.18 and 4.19, respectively.

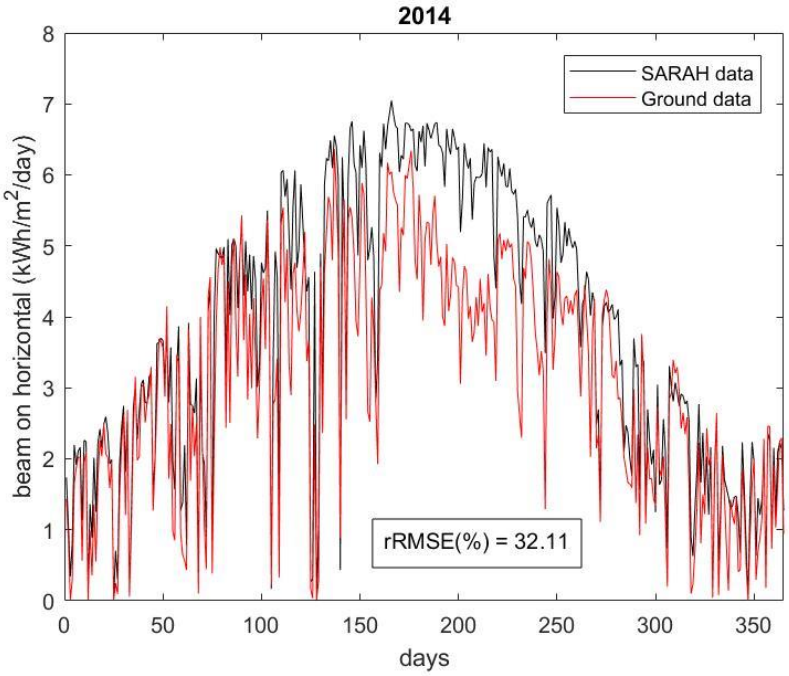

Figure 4.17. Comparison of ground-measured and satellite-based daily total DNI with rRMSE value, in 2014.

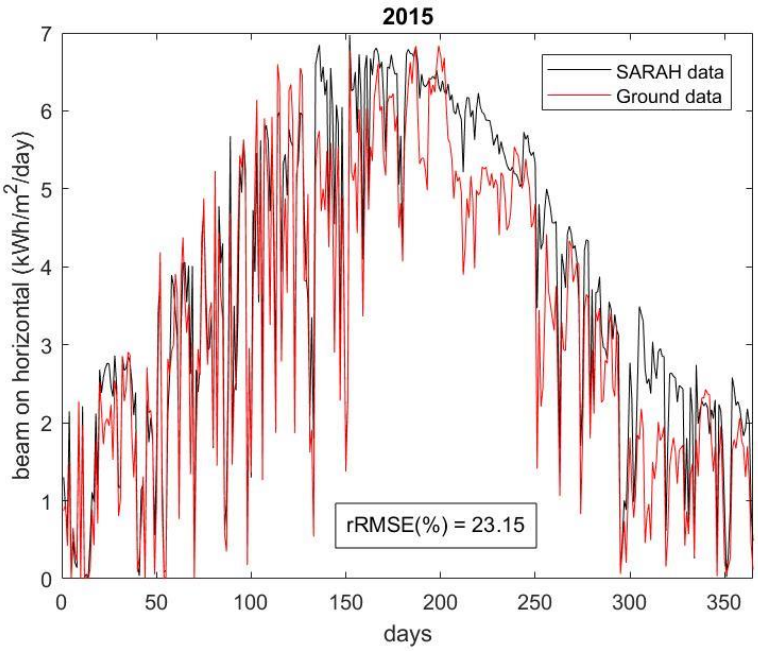

Figure 4.18. Comparison of ground-measured and satellite-based daily total DNI with rRMSE value, in 2015.

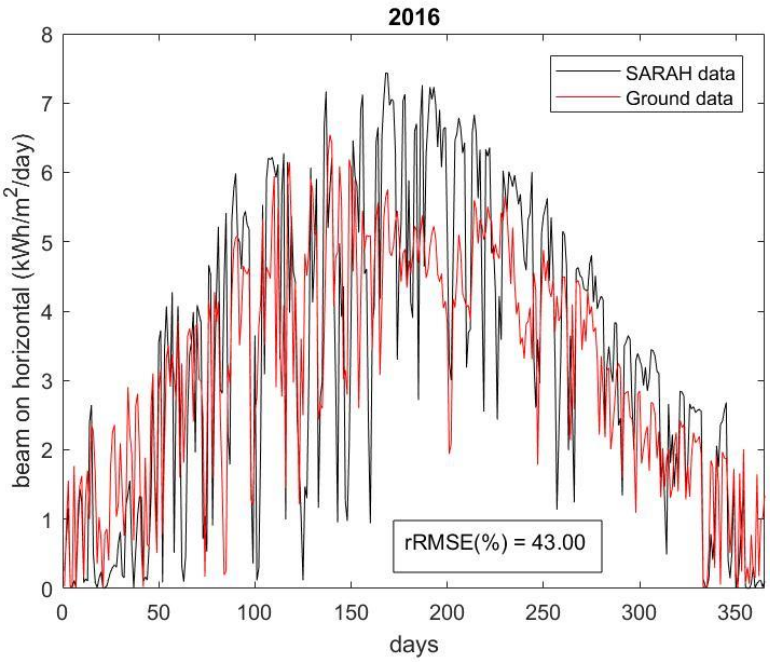

Figure 4.19. Comparison of ground-measured and satellite-based daily total DNI with rRMSE value, in 2016.

4.1.2 Variability of Global Horizontal Irradiation

In this study, the long-term solar radiation trend is investigated to see its effect on the energy yield estimations. As mentioned above, a multi-year weather dataset enables the calculation of the interannual variability, and more reliable results are obtained as the time period of the dataset increases. On the other hand, a TMY dataset is useful when doing preliminary calculations of a solar PV energy project. In this study, both TMY and multi-year datasets are used to estimate the energy yield, and the differences between TMY and individual weather datasets obtained from PVGIS are shown in the box plot of monthly GHI in Figure 4.20. This shows us that although TMY gives an average of the individual years, we can see that year 2016 was an outlier and that year can be considered a low-resource year in terms of solar radiation.

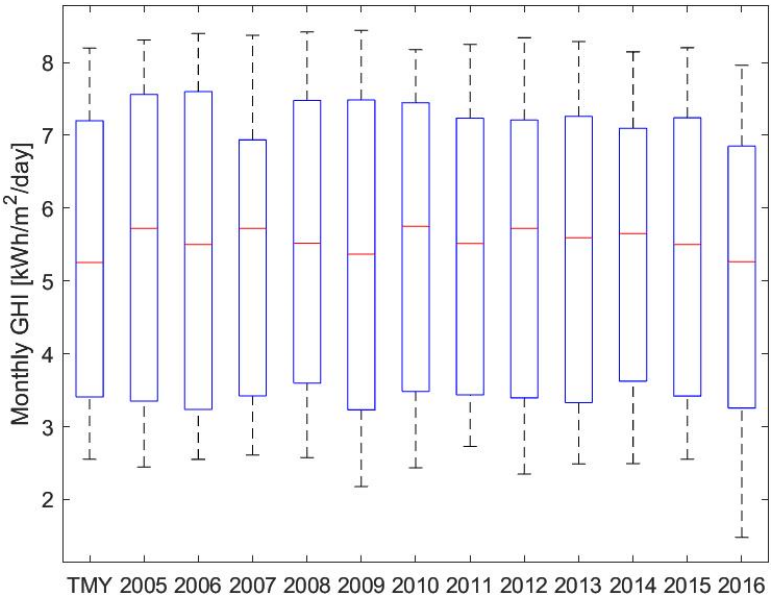

Figure 4.20. Monthly average daily total GHI at METU NCC, between 2005 and 2016 (PVGIS-SARAH), in comparison with PVGIS-TMY.

The coefficient of variation (COV) is found to estimate both intra-annual and interannual variability of GHI between 2010 and 2016. In Tables 4.3 and 4.4, the

results of monthly and annual mean daily total GHI for ground-measured and satellite-based data are represented, respectively. Both ground-measured and satellite-based data results show that the intra-annual variability of GHI is higher in winter months, whereas, the summer season has the lowest variability. On the other hand, the interannual variability of GHI is found as 5.94% and 2.21% for ground-measured and satellite-based data, respectively. This is expected since the solar resource variability decreases as the time period increases [65]. Similarly, another study was done to observe the long-term solar radiation trends in the Black Sea and Mediterranean region using satellite-based data between 1985 and 2004 [20]. They also found that the lowest and highest variability of GHI was observed in summer and winter, respectively. Also, they reported low interannual variability, which is lower than 4%, for Northern Africa, Middle East, and the Mediterranean islands. Therefore, our COV results match with this study. Other statistical indices and the COV results can also be seen. A comparison of the intra-annual and interannual variabilities of ground-measured and satellite-based GHI was provided in Figure 4.21.

Table 4.3 Constructed ground-measured data results of monthly and annual mean daily total GHI (kWh/m^2/day).

	Jan	Feb	Mar	Apr	May	Jun	Jul	Aug	Sep	Oct	Nov	Dec	Annual
2010	2.16	2.99	4.74	6.23	6.86	7.43	7.23	6.61	5.69	3.84	3.14	2.27	4.94
2011	2.49	3.46	5.01	5.39	6.56	7.73	7.60	6.93	5.65	4.27	2.81	2.47	5.04
2012	2.28	3.39	4.92	6.05	6.68	7.65	7.49	6.98	5.94	4.02	2.88	2.16	5.04
2013	2.44	2.65	4.92	6.21	6.68	8.21	8.07	7.30	6.06	4.86	2.82	2.36	5.23
2014	2.65	3.98	5.10	5.77	5.66	6.64	6.45	5.80	5.03	3.50	2.71	2.25	4.63
2015	2.23	3.08	4.48	6.10	6.04	7.35	7.53	6.56	4.99	3.64	2.38	2.18	4.72
2016	1.45	2.62	4.27	5.56	6.22	6.70	6.22	6.30	5.39	3.94	2.72	1.24	4.39
min	1.45	2.62	4.27	5.39	5.66	6.64	6.22	5.80	4.99	3.50	2.38	1.24	4.39
max	2.65	3.98	5.10	6.23	6.86	8.21	8.07	7.30	6.06	4.86	3.14	2.47	5.23
std.	0.39	0.48	0.30	0.33	0.43	0.56	0.66	0.50	0.42	0.45	0.23	0.41	0.29
mean	2.24	3.17	4.77	5.90	6.39	7.39	7.23	6.64	5.54	4.01	2.78	2.13	4.86
COV(%)	17.21	15.25	6.31	5.61	6.69	7.59	9.15	7.47	7.52	11.25	8.19	19.19	5.94

Table 4.4 Satellite-based data results of monthly and annual mean daily total GHI (kWh/m^2/day).

	Jan	Feb	Mar	Apr	May	Jun	Jul	Aug	Sep	Oct	Nov	Dec	Annual
2005	2.45	3.51	5.24	6.20	7.68	8.31	8.24	7.44	6.31	4.69	3.20	2.55	5.50
2006	2.55	3.19	4.73	6.27	7.75	8.40	8.03	7.46	6.27	4.17	3.29	2.70	5.41
2007	2.93	3.47	5.08	6.36	6.47	8.37	8.01	7.41	6.46	4.76	3.38	2.61	5.45
2008	2.87	3.78	5.24	6.65	7.76	8.42	8.24	7.19	5.80	4.53	3.42	2.57	5.55
2009	2.59	3.22	4.87	6.50	7.51	8.44	8.21	7.46	5.87	4.58	3.24	2.18	5.40
2010	2.44	3.37	5.19	6.68	7.59	8.06	8.18	7.31	6.31	4.31	3.60	2.63	5.48
2011	2.77	3.60	5.26	5.77	6.96	8.20	8.25	7.51	6.18	4.66	3.27	2.73	5.44
2012	2.42	3.66	5.10	6.35	7.00	8.34	7.90	7.42	6.36	4.28	3.13	2.35	5.37
2013	2.63	3.54	4.89	6.53	6.99	8.29	8.23	7.53	6.23	4.96	3.13	2.49	5.46
2014	2.83	4.06	5.24	6.58	6.83	8.08	8.15	7.37	6.07	4.31	3.19	2.49	5.44
2015	2.55	3.38	4.87	6.54	7.07	8.20	8.18	7.41	6.13	4.16	3.46	2.77	5.40
2016	1.48	3.22	4.79	6.41	6.25	7.84	7.96	7.30	5.74	4.69	3.29	1.76	5.07
min	1.48	3.19	4.73	5.77	6.25	7.84	7.90	7.19	5.74	4.16	3.13	1.76	5.07
max	2.93	4.06	5.26	6.68	7.76	8.44	8.25	7.53	6.46	4.96	3.60	2.77	5.55
std.	0.38	0.25	0.20	0.25	0.51	0.18	0.12	0.10	0.23	0.26	0.14	0.28	0.12
mean	2.54	3.50	5.04	6.40	7.15	8.25	8.13	7.40	6.14	4.51	3.30	2.49	5.41
COV(%)	14.81	7.28	3.93	3.88	7.07	2.18	1.50	1.29	3.78	5.72	4.29	11.40	2.21

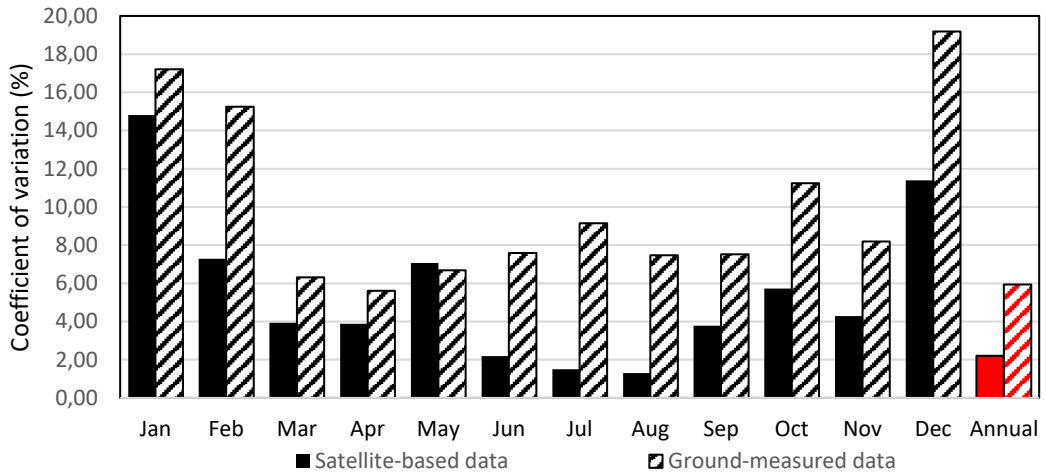

Figure 4.21. Monthly and annual COV values of ground-measured (constructed) and satellite-based GHI data.

4.1.3 Global Tilted Irradiation Results

Estimated GTI is compared with tilted pyranometer measurements in 2016, which is recorded since February 13, 2016. Thus, a comparison is made for ten months in 2016, excluding January and February. According to Table 4.5, similar results are found for estimated GTI and satellite-based GTI, except monthly mean RMSE

results. In Figure 4.22, a comparison of the measured, estimated and satellite-based GTI in 2016 is shown. It can be understood that estimated GTI has the lowest results when compared to measured and satellite-based GTI data. On the other hand, using satellite-based data predicts similar GTI with measured GTI. Thus, it can be said that choosing the type of dataset affects the GTI data directly, which is used to predict the energy yield of a solar PV plant. For example, using a tilted pyranometer to measure GTI will give more reliable data rather than measuring GHI and then estimating GTI with a transposition model since there will be fewer sources of error, such as the accuracy of the transposition model used. In addition, DNI should also be measured with a pyrheliometer if GHI is measured, which helps to eliminate the need for estimating beam and diffuse components by using a decomposition model. However, this study also showed that the accuracy of the measurements, calibration of the sensors and cleaning them regularly are very important to obtain highly accurate and quality-checked ground-measured data, which was not the case for the ground-measured data according to the quality assessment. Besides, considering that long-term ground measurements with the quality check are not available in every region of the world, using satellite-based data can be an option to make reliable and long-term energy yield prediction, which is also valid for this study. Finally, estimated GTI was superimposed to the graphs of the constructed GHI, beam and diffuse horizontal irradiation (DHI) data for the years 2014, 2015 and 2016, which can be seen in Figures 4.23, 4.24 and 4.25.

Table 4.5 RMSE (%) with respect to measured GTI in 2016, excluding January and February.

	hourly	daily total	monthly mean
estimated GTI	48.23	22.41	20.78
satellite-based GTI	54.92	20.81	10.34

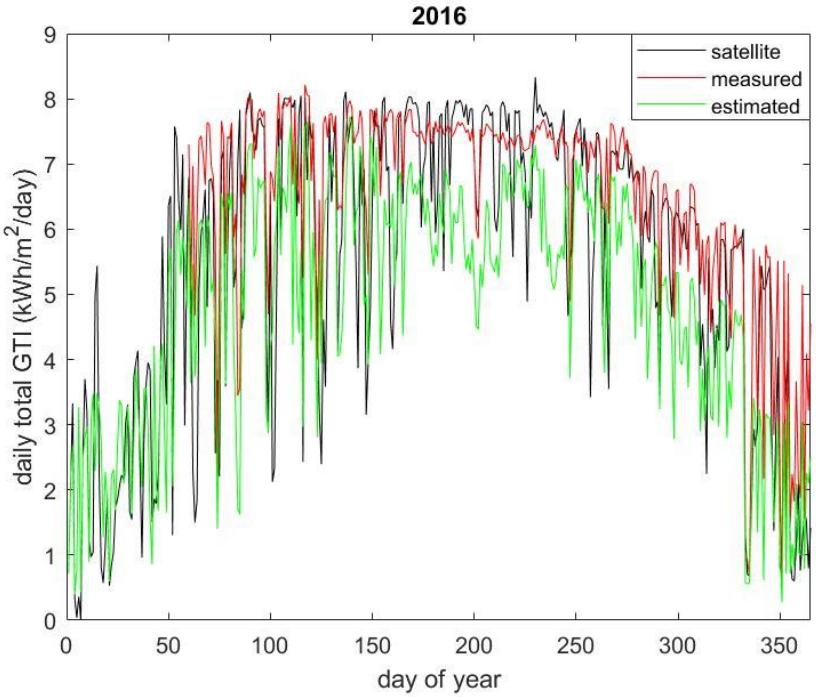

Figure 4.22. A comparison of daily total global tilted irradiation (GTI) of satellite-based, measured and estimated data in 2016.

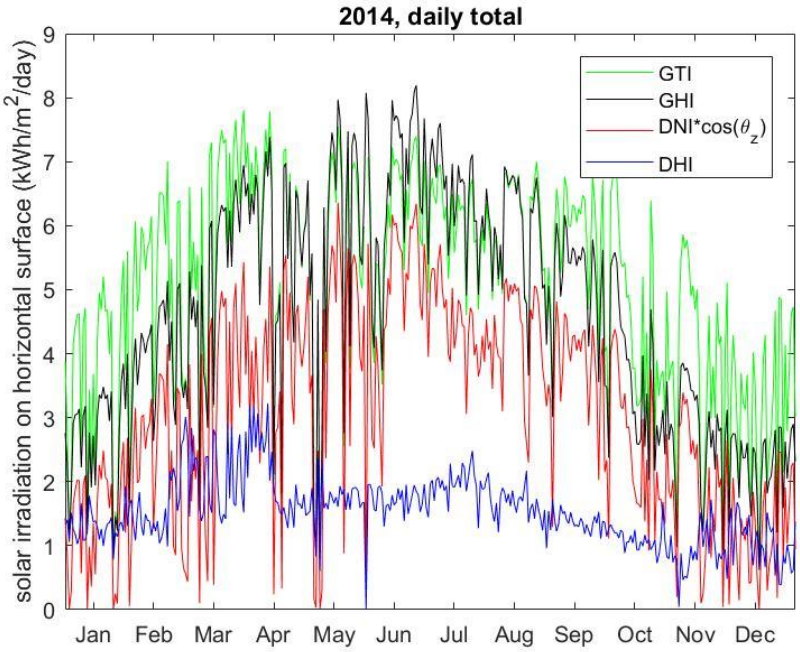

Figure 4.23. Comparison of GTI, GHI, beam and diffuse irradiation in 2014.

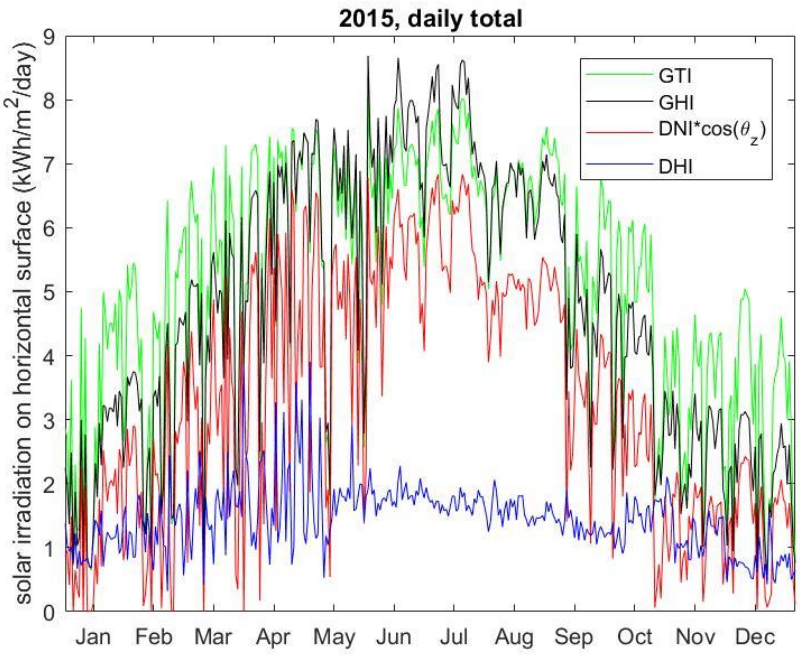

Figure 4.24. Comparison of GTI, GHI, beam and diffuse irradiation in 2015.

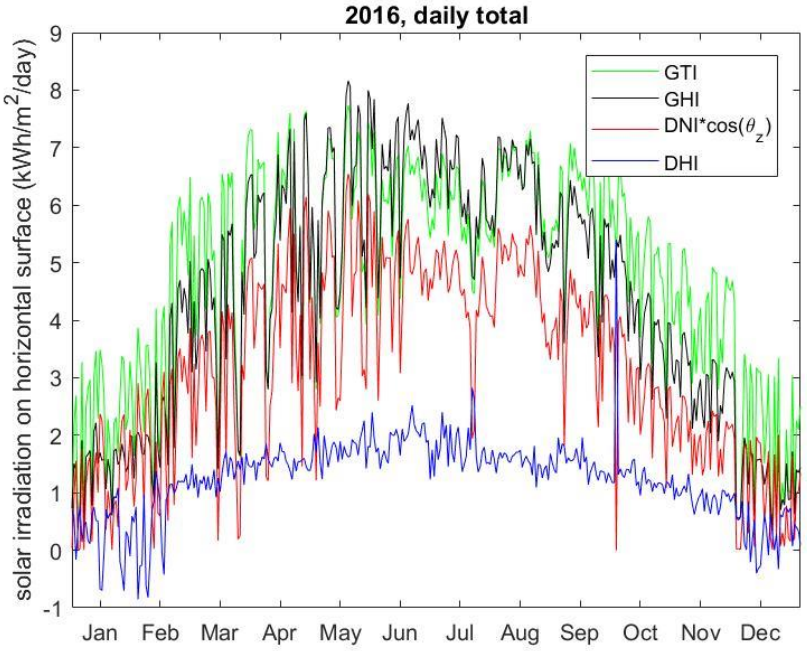

Figure 4.25. Comparison of GTI, GHI, beam and diffuse irradiation in 2016.

4.2 Energy and Economic Yield Estimations

In Table 4.6, all energy yield results can be seen, and Figure 4.26 gives a comparison of these results. It can be seen that year 2016 has the most information in terms of the availability of datasets. In 2016, the energy yield was 1693 kWh/kWp; however, measurements started from February 13, since the solar PV plant became operational from that day. Thus, energy yield in 2016 should be slightly higher than that measured value. In 2017, the solar PV plant produced 1807 kWh/kWp. There is a clear difference in the energy produced between 2016 and 2017, and 2016 reflects the low solar resource, whereas 2017 is one of the high resource years according to the energy yield calculations. However, using satellite-based data underpredicted the actual energy yield value of 2016 by about 8.67% in SAM, although it was assumed that GHI is overestimated by 3.5% for the Cyprus region by the PVGIS-SARAH dataset. Still, the difference between the results of satellite-based and actual AEP data might be because of the modeling assumptions used in SAM, such as the PV system losses.

After calculating the energy yield in MATLAB codes, energy yield values were found for 1 MWp solar PV plant using satellite-based, ground-measured and TMY datasets. For satellite-based data results, calculations were done both in SAM and MATLAB, and it was found that using SAM resulted in 14.74% lower estimations on average compared to the calculations in MATLAB codes. This is due to the modeling assumptions like PV system losses used in SAM as mentioned previously. On the other hand, ground measurements gave different estimations according to the type of GTI used. For example, using estimated GTI from constructed GHI and measured DNI underestimated the energy yield in 2016 by 10.6%. However, using measured GTI was overestimated by 9.4% compared to the actual energy yield in 2016. It should be noted that actual and estimated energy yields were obtained after February 13, 2016. Similarly, using measured GTI in 2017 overestimated the energy yield by 11.4%. Besides, three different TMY datasets were used to compare their

estimations with other results, and the Meteonorm dataset gave the closest energy yield compared to actual values.

Table 4.6 Energy yield (kWh/kWp) estimations using different datasets with isotropic sky-diffuse model. System Advisor Model (SAM) results were also shown for satellite-based data.

Year	Satellite (SAM)	Satellite (MATLAB)	Ground using estimated GTI (MATLAB)	Ground using measured GTI (MATLAB)	Actual	TMY_Meteonorm (MATLAB)	TMYx.2004-2018 (MATLAB)	TMY_PVGIS (MATLAB)
2005	1735.6	2,030.50	–	–	–	1,799.88	1,816.98	1,854.46
2006	1703.2	1,989.65	–	–	–	1,799.88	1,816.98	1,854.46
2007	1740.19	2,032.37	–	–	–	1,799.88	1,816.98	1,854.46
2008	1760.59	2,056.50	–	–	–	1,799.88	1,816.98	1,854.46
2009	1687.79	1,978.65	–	–	–	1,799.88	1,816.98	1,854.46
2010	1725.82	2,024.00	–	–	–	1,799.88	1,816.98	1,854.46
2011	1730.98	2,032.30	–	–	–	1,799.88	1,816.98	1,854.46
2012	1680.78	1,972.35	–	–	–	1,799.88	1,816.98	1,854.46
2013	1720.12	2,013.76	–	–	–	1,799.88	1,816.98	1,854.46
2014	1721.01	2,017.39	1,705.72	–	–	1,799.88	1,816.98	1,854.46
2015	1697.74	1,999.26	1,710.96	–	–	1,799.88	1,816.98	1,854.46
2016	1546.37	1,838.30	1,513.88	1851.57	1,693.11	1,799.88	1,816.98	1,854.46
2017	–	–	–	2,014.08	1,807.75	1,799.88	1,816.98	1,854.46
average	1704.18	1,998.75	1,643.52	1,932.82	1,750.43	1,799.88	1,816.98	1,854.46

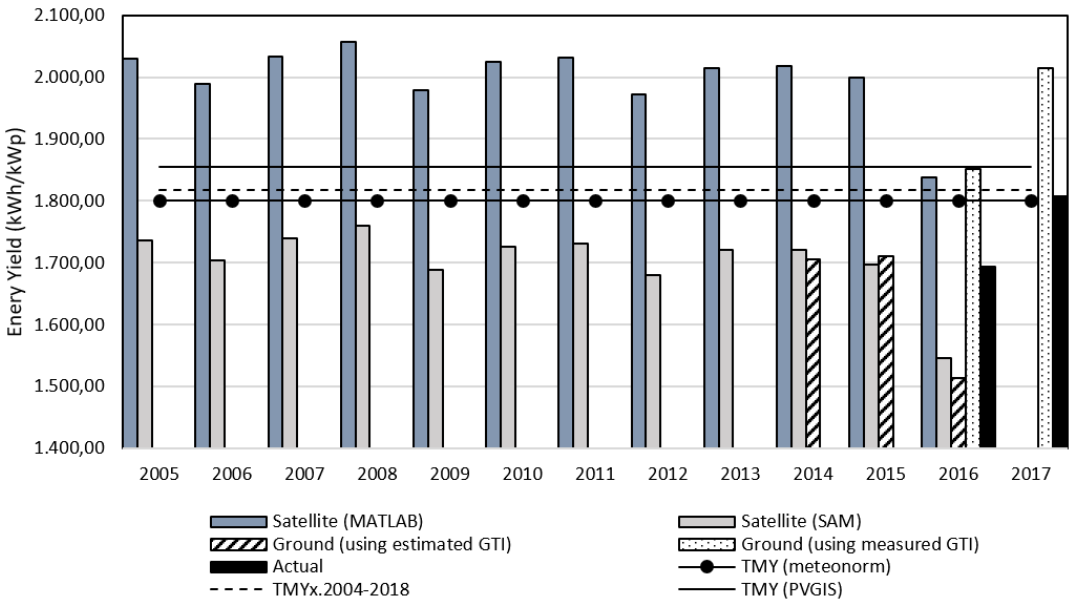

Figure 4.26. A comparison of satellite-based, ground-measured, TMY and actual energy yield results obtained from calculations and SAM simulations using isotropic sky-diffuse model.

4.2.1 TMY, Empirical and Normal Distribution

The empirical CDF of annual mean GHI was obtained using the 12-year satellite-based data of PVGIS-SARAH, which can be seen in Figure 4.27. This graph shows the POE values of GHI, and each GHI value was sorted in ascending order with an equal probability of occurrence. Therefore, each year is paired with a specific POE value. For example, the lowest annual mean GHI belongs to the year 2016, and since that data point is very close to P90, the year 2016 can be considered the P90 of GHI. Also, there are only 12 years of GHI data, the year 2016 also represents the minimum GHI, which can be assumed as the worst case. On the other hand, the year 2014 stands for P50, and P10 can be represented by the year 2005. This graph was obtained empirically; thus, different shapes can be obtained if the time period of satellite-based data decreases or increases. However, a better representation of the long-term GHI of a site is obtained if the available time period of the dataset increases [4].

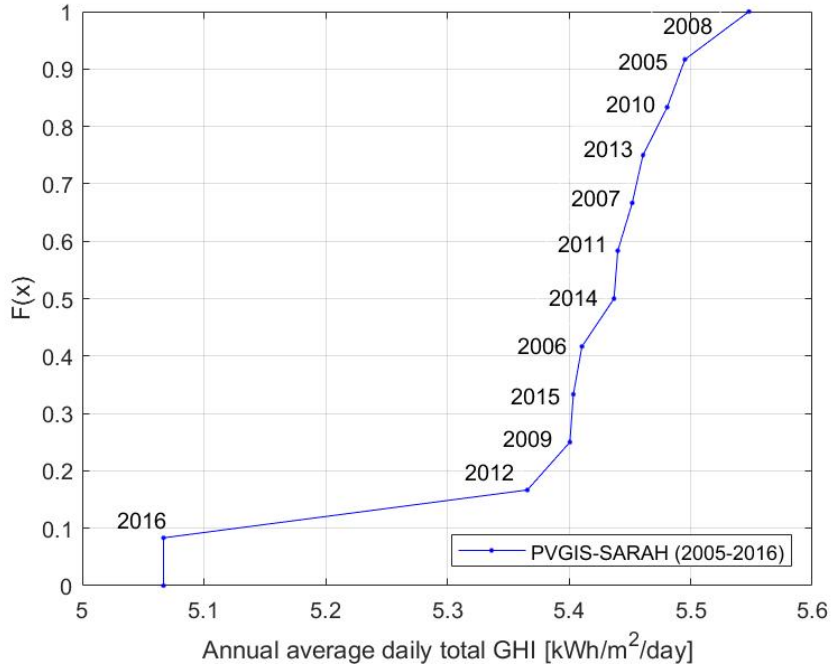

Figure 4.27. Empirical cumulative distribution function of annual GHI according to satellite-based data between time period 2005-2016.

A base case scenario was obtained using three different TMY datasets, and the results are presented in Table 4.7. POE values cannot be calculated with TMY simulation since outlier weather events are not included in 1-year TMY data; thus, the most typical results of GHI, POA and AEP are found for each TMY dataset. On the other hand, the same simulations were done using the satellite-based data, and results were obtained for each year during the time period 2005-2016. In addition, P50/P90 analysis was done using the multi-year data set, and energy exceedance probabilities were found for GHI and AEP values. It is worth mentioning that SAM enables a much faster analysis with P50/P90 option rather than calculating individual AEPs for each year and finding the empirical CDF according to the AEP values. One can also find the same POE values using AEP results shown for each year in Table 4.7.

In Table 4.7, the interannual variability of annual GHI was found as about 2.21%. For the AEP, the variability is about 3.26%, which is the average value of the coefficient of variation (COV) of three different transposition models, while the LCOE varies by 3.50% as a function of AEP. Thus, the variability increases from solar irradiation to AEP, and the most increase is found in the LCOE results. This shows us the sensitivity of an economic index to solar resource and the importance of doing P50/P90 analysis to make investment decisions.

Table 4.7 Simulation results of three different TMY data sets and satellite-based data for the 1 MW solar PV plant in METU NCC. POA, AEP and LCOE values were averaged according to different transposition models used in SAM software (Isotropic, HDKR and Perez). Detailed results are available in Appendix A.

Database	Temperature (ºC/yr)	GHI (kWh/m²/yr)	POA (kWh/m²/yr)	AEP (MWh/yr)	LCOE ($/kWh)
TMY2-Meteonorm	19.70	1811.89	2001.48	1555.70	0.138
deviation of TMY from P50 (%)	-1.01	-8.70	-9.74	-11.43	12.91
TMYx.2004-2018	17.90	1880.1	2076.80	1620.80	0.132
deviation of TMY from P50 (%)	-10.05	-5.26	-6.35	-7.72	8.37
PVGIS-TMY (2007-2016)	19.70	1954.73	2182.26	1733.59	0.124
deviation of TMY from P50 (%)	-1.01	-1.50	-1.59	-1.30	1.32
average TMY	19.10	1882.24	2086.85	1636.69	0.131
deviation of TMY from P50 (%)	-4.02	-5.15	-5.89	-6.82	7.53
PVGIS-SARAH					
2005	19.30	2005.80	2225.54	1771.73	0.121
2006	19.50	1974.91	2186.58	1739.35	0.123
2007	19.70	1989.99	2235.39	1777.76	0.121
2008	19.90	2024.99	2263.02	1798.62	0.119
2009	19.90	1971.29	2173.60	1722.82	0.124
2010	20.60	2000.47	2228.37	1762.48	0.122
2011	19.50	1985.66	2227.19	1767.85	0.121
2012	19.80	1958.54	2171.41	1715.56	0.125
2013	20.00	1993.22	2217.56	1756.48	0.122
2014	20.00	1984.52	2219.18	1757.66	0.122
2015	20.10	1972.33	2199.40	1733.44	0.124
2016	20.30	1849.40	2015.32	1576.36	0.136
min	19.30	1849.40	2015.32	1576.36	0.119
max	20.60	2024.99	2263.02	1798.62	0.136
st.dev.	0.36	43.60	63.09	56.77	0.0043
mean	19.88	1975.93	2196.88	1740.01	0.123
COV (%)	1.82	2.21	2.87	3.26	3.50
P90	19.34	1871.23	2046.54	1604.20	0.134
P75	19.50	1971.29	2173.60	1722.82	0.124
P50	19.90	1984.52	2217.56	1756.48	0.122
P25	20.00	1993.22	2227.24	1767.85	0.121
P10	20.26	2004.74	2233.99	1776.55	0.121

In Figure 4.28, empirical CDFs with TMY results are shown for three different transposition models. According to the comparison of TMY and P50 values, it was found that TMY datasets underpredicted the annual GHI by about 5.15%, and the AEP values by 6.77%, 6.86% and 6.83%, for isotropic, HDKR and Perez models, respectively. As a result, TMY simulations underpredicted the AEP in all cases and it can be concluded that the P50 assumption for TMY is not valid for the location in

Cyprus. Moreover, the TMY dataset with the isotropic sky diffuse model predicted the lowest P50 assumption, whereas the anisotropic models estimated a higher probability of exceedance values. The reason is that anisotropic models are more sensitive to the DHI component; thus, more accurate GTI estimations result in higher energy yield estimations [19]. However, the Perez model is not recommended if the measured DHI is not available since the model is highly sensitive to the measurements [66]. Thus, the average of the three model results are obtained in Table 4.7 so that a more general discussion can be made for the POE values, irrespective of transposition models used. A detailed version of Table 4.7, which includes the transposition models, can be seen in Appendix A.

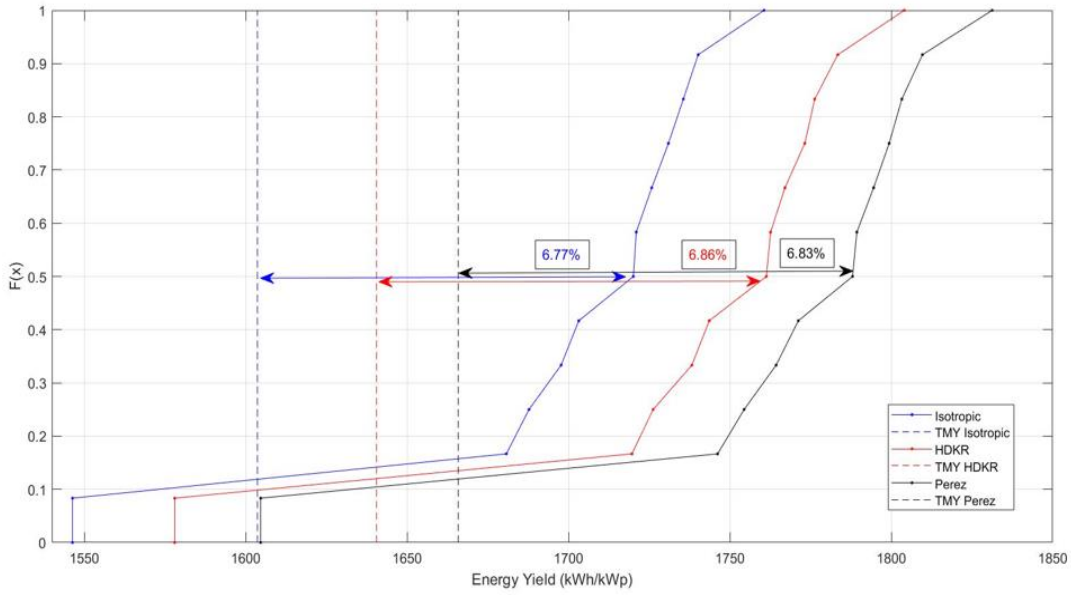

Figure 4.28. Empirical cumulative distribution functions of the energy yield (kWh/kWp) using Isotropic, HDKR and Perez models. Double arrows show the difference between the average TMY and P50 values.

SAM software also calculates POE values assuming a Normal CDF which is obtained by using the mean and standard deviation of data, and normal CDFs are superimposed in Figures 4.29 and 4.30 to compare with the results of the study. In Table 4.8, a comparison was made according to the results of Normal and empirical CDFs. It was found that the P50 value was underpredicted by the Normal CDF assumption for all cases, which means that using the empirical method gives more realistic P50 results. On the other hand, Normal CDF significantly overpredicted P90 values than the empirical CDF both for annual GHI and the energy yield. Therefore, empirical P90 values should be used since conservative results are the focus of obtaining P90. Overall, Normal CDF did not represent the actual results, and the empirical method is a reliable approach to find POE values if there exist at least ten years of a dataset. It should be kept in mind that including recent years' data (2017, 2018, 2019) will change the empirical CDF and the POE values; thus, the results of this study depend on the historical time period between 2005 and 2016.

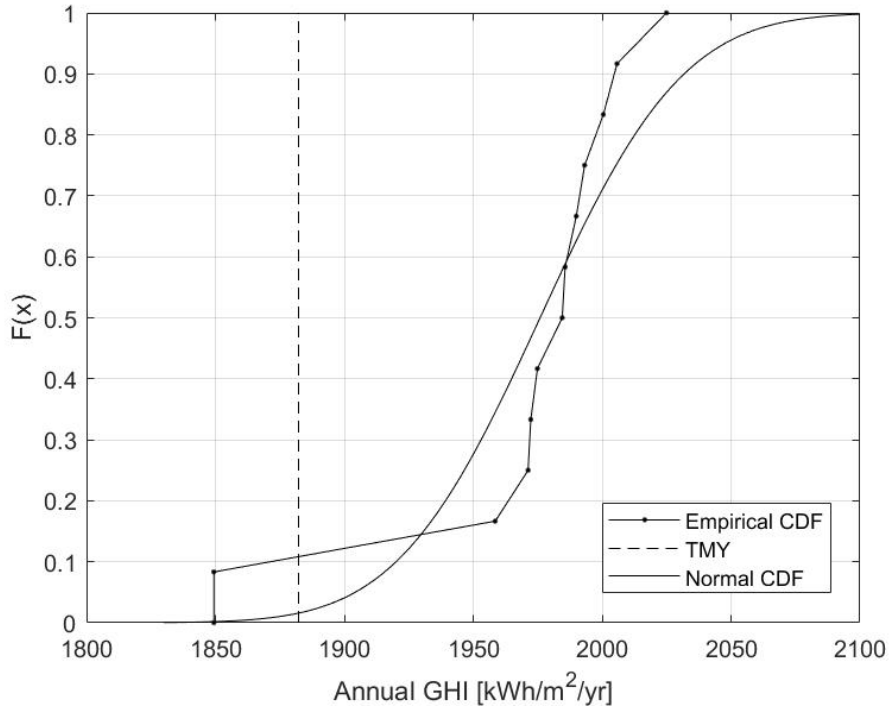

Figure 4.29. Comparison of empirical and normal CDFs with average TMY result of the annual GHI, for time period 2005-2016.

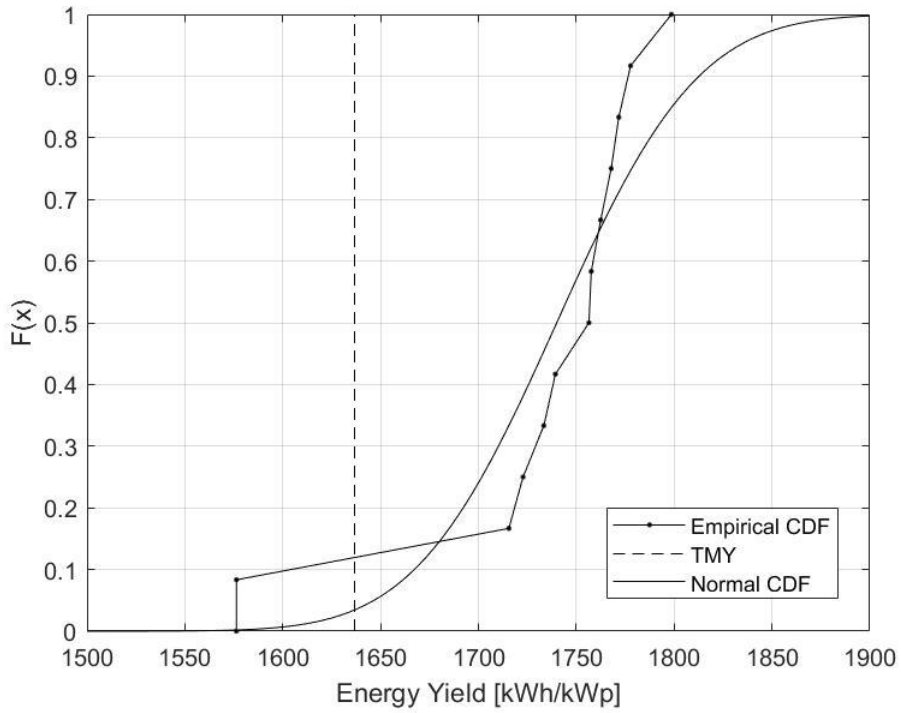

Figure 4.30. Comparison of empirical and normal CDFs with TMY results of the energy yield, for time period 2005-2016.

Table 4.8 Probability of exceedance values of annual GHI and energy yield according to Normal and Empirical CDFs. Deviation of Normal CDF from empirical CDF values are shown in the last column as percentages.

GHI (kWh/m^2/yr)	POE	Normal CDF	Empirical CDF	Δ(%)
	P50	1975.93	1984.52	-0.43
	P90	1920.03	1871.23	2.61
Energy Yield (kWh/kWp)				
	P50	1740.15	1756.48	-0.93
	P90	1667.23	1604.20	3.93

4.2.2 Stochastic Simulations

Apart from the empirical and Normal distribution assumptions, a stochastic simulation was carried out to find the POE values of energy yield. By doing so, modeling assumptions and other uncertainty components also had a distribution which is given in Table 3.7. In Appendix B, an example of 100 computing samples created by the stochastic simulation in SAM, using the input variables in Table 3.7 can be seen.

In Figure 4.31, CDFs were obtained both for TMY and satellite-based datasets using all uncertainty distributions. First, it can be noted that TMY results also had a distribution unlike previous results, because stochastic simulation computed many samples using possible uncertainty assumptions. Thus, other POE values such as P90 and P10 can also be found using a TMY dataset, if stochastic simulation is done. However, it should be kept in mind that TMY distributions still do not include the interannual variability of solar radiation, which is one of the main factors when estimating POE values [27]. In Table 4.9, POE values of energy yield are compared between TMY and satellite results. P99 and P95 values were also found and compared to see the worst-case estimates. Using a TMY dataset underpredicted the POE values except for P99, and for P50, the deviation of TMY from satellite increased to about 9%, which was about 7% in empirical CDF results.

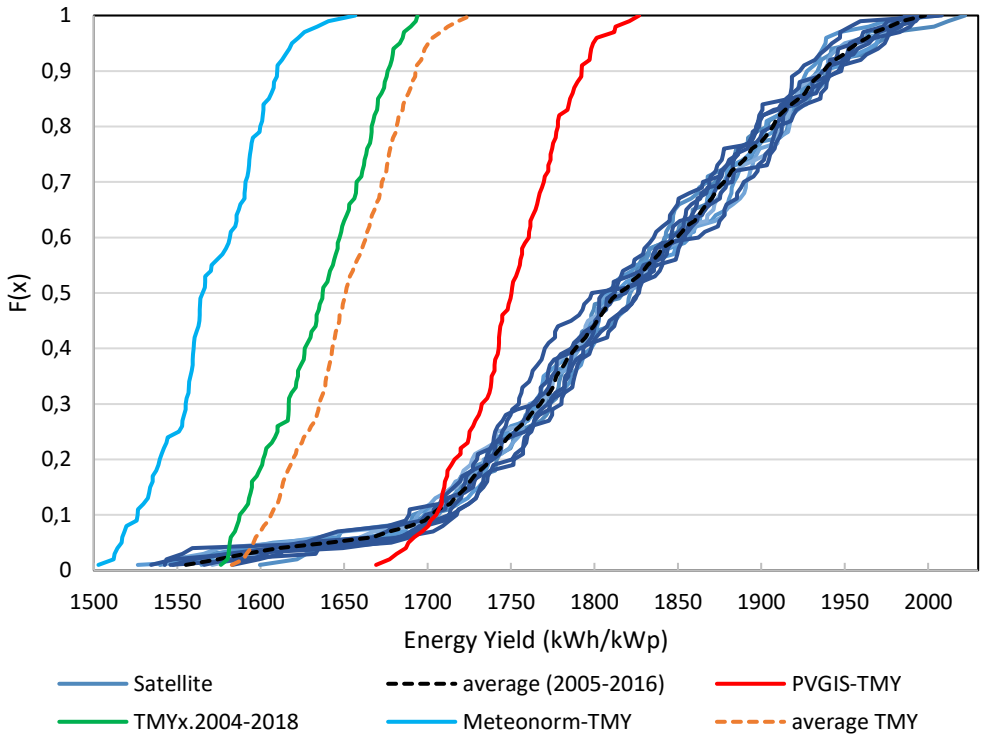

Figure 4.31. CDF of energy yields generated by stochastic simulation, using all uncertainty distributions given in Table 3.7.

Table 4.9 Empirical cumulative distribution results of stochastic simulation for satellite-based and TMY datasets. Deviation of the mean TMY results from mean satellite-based data are also given in percentages.

PVGIS-SARAH	P99	P95	P90	P50	P10
mean (kWh/kWp)	1555.20	1641.00	1702.11	1814.52	1937.41
st.dev. (kWh/kWp)	21.70	24.61	9.17	8.51	6.98
range (%)	4.70	4.31	1.68	1.56	1.29
TMY					
mean (kWh/kWp)	1582.67	1595.60	1606.30	1650.89	1692.73
deviation of mean (%)	1.77	-2.77	-5.63	-9.02	-12.63

On the other hand, some differences were observed between stochastic simulation and empirical CDF graphs. To see the effect of each variable on the CDF, following scenarios were simulated for input variables:

- Only sky-diffuse model
- Sky-diffuse & temperature correction model
- Sky-diffuse & self-shading model
- Sky-diffuse & temperature correction & self-shading model
- All input variables in Table 3.7

The first difference is that, the shape of CDF was linearized, and the reason was understood when only sky-diffuse model was chosen as input variable, ignoring other uncertainty distributions. Stochastic simulation computed random samples using Isotropic, HDKR and Perez models, and sorting them in ascending order created the following CDF in Figure 4.32. These results match with the previous empirical results obtained from Isotropic, HDKR and Perez models.

Secondly, the minimum and maximum energy yield values scaled down and up, respectively, because of assigning other uncertainty components as input variables. However, it was also observed that changing temperature correction model made CDF right skewed, which caused higher energy yield values that can be seen in Figure 4.33. In temperature correction model, NOCT method was chosen as input in empirical results. In stochastic simulation, heat transfer method was also randomly selected in the samples, and this may explain the reason behind increased energy yields.

Finally, changing only sky-diffuse model and all input variables were compared in Figure 4.34. According to the energy yields, changing all input variables increased the mean P90, P50 and P10 by 1.25%, 3.69% and 7.50%, respectively, when compared to changing only sky-diffuse model. Therefore, these results clearly show the importance of choosing modelling assumptions and losses when doing energy calculations.

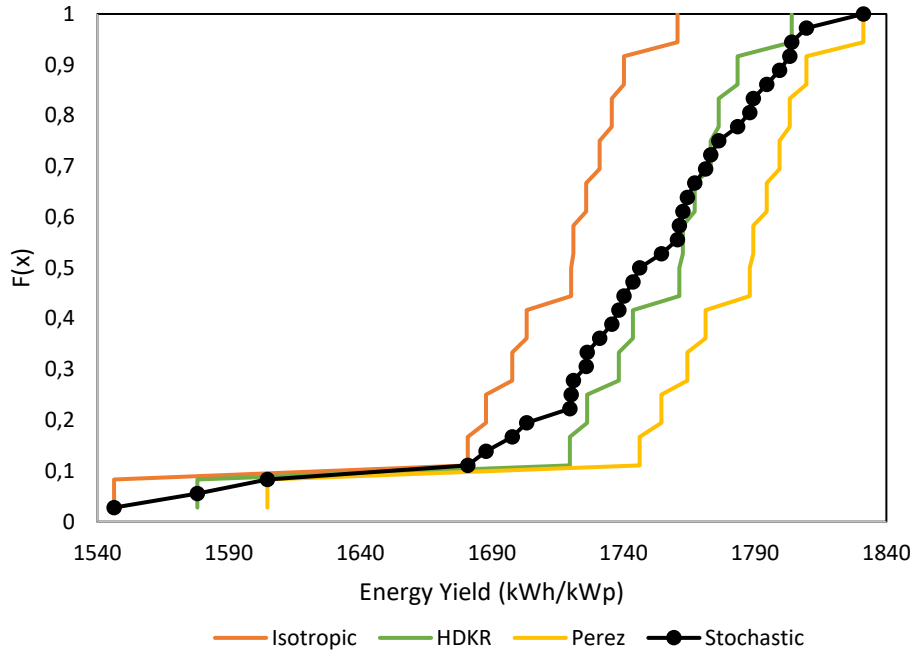

Figure 4.32. A comparison of empirical and stochastic CDF results, when only sky-diffuse model is changed.

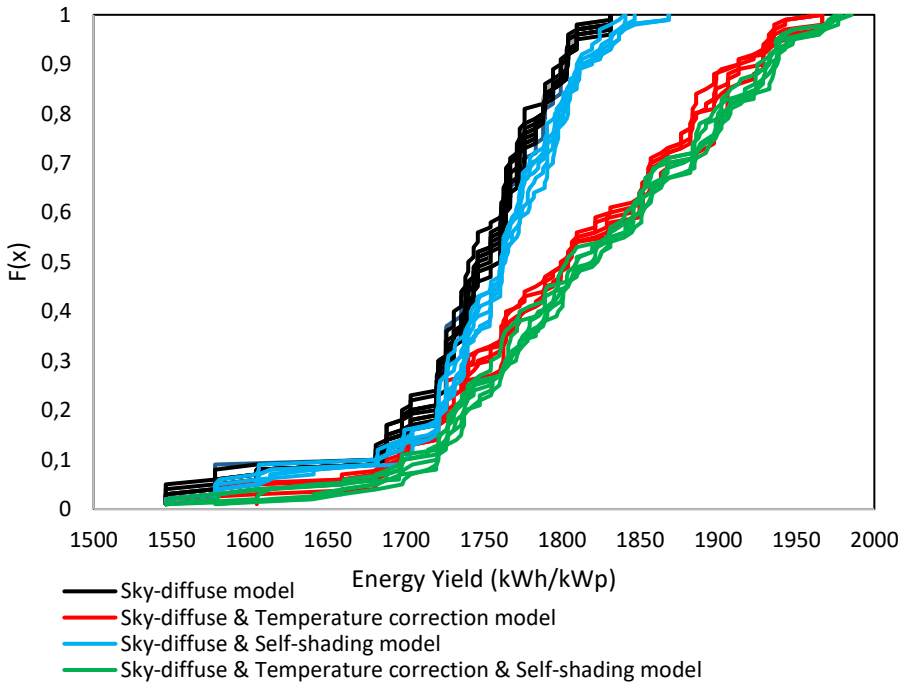

Figure 4.33. A comparison of scenarios of different input variables used in stochastic simulation.

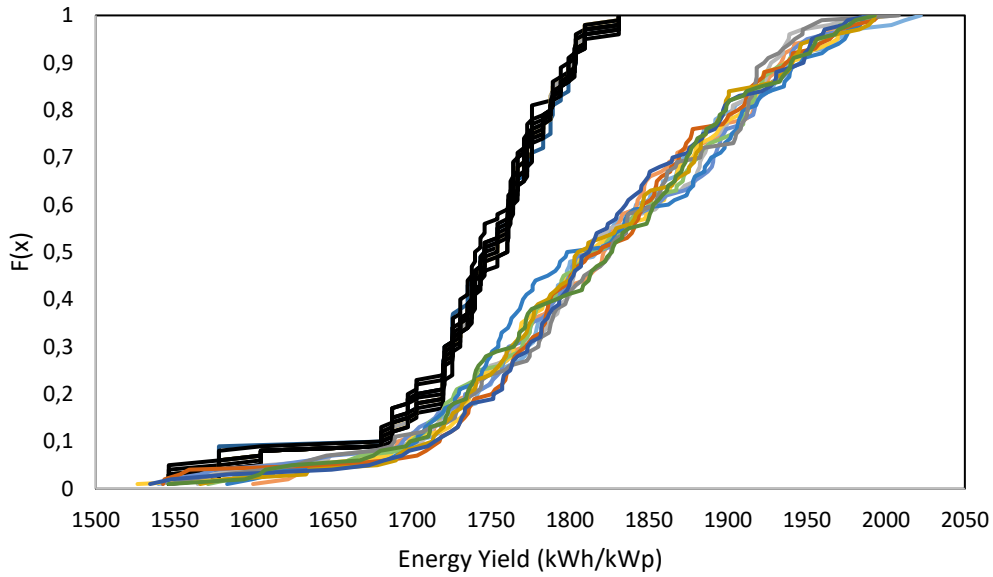

Figure 4.34. Comparison of stochastic simulations. Black lines were obtained by only changing sky-diffuse model, colored lines were obtained using the input variables in Table 3.7.

To sum up, different methods were applied to estimate the long-term energy yield of a 1 MWp solar PV plant, and to find POE values. First, TMY datasets were used to see an average energy yield and the P50 assumption was made. Then, empirical and Normal CDFs were obtained using satellite-based data, and these graphs represent the 12-year period between 2005 and 2016. Finally, a stochastic simulation was done to see the effect of uncertainty distributions on possible energy yield values. Although TMY datasets were again used to obtain a distribution by stochastic simulation, those results are not included in Table 4.10. Because the interannual variability of GHI does not exist in a TMY dataset, only P50 assumption of TMY is given in Table 4.10, which was previously obtained in SAM. In Table 4.10, the average results of energy yield that are found using TMY, Normal CDF, empirical CDF and stochastic simulation are shown, specifically, P50, P90 and P90/P50 ratios. Doing stochastic simulations resulted in the highest POE values in all methods. For example, P50 and P90 values increased by 3.30% and 6.10% compared to empirical method, respectively. Thus, a detailed uncertainty analysis in a stochastic simulation

can increase the expected energy yield and the bankability of a project. On the other hand, a high P90/P50 ratio means that P90 value converges to P50, which in turn, reduces the risk of having lower energy yields [27]. In this study, all methods gave P90/P50 ratios that are close to 100%. Although Normal distribution assumption has the highest ratio, it does not represent a realistic result since higher P50 values were obtained from empirical and stochastic simulation methods. Belluardo et al. [27] also found similar results in which they compared P50 and P90 values from using Normal distribution and using Monte Carlo approach. They found the P50 value as about 1445 kWh/kWp as a base case scenario for a solar PV plant in Bolzano, Italy, and they found that Normal distribution assumption resulted in higher-than-expected P90 and P99 values compared to Monte Carlo approach [27]. They also found the P90/P50 ratio as 94% for the best-case scenario with an overall uncertainty of 4.6%.

Table 4.10 P50, P90 and P90/P50 comparisons of energy yield using different methods.

Method	P50 (kWh/kWp)	P90 (kWh/kWp)	P90/P50 (%)
TMY	1636.69	–	–
Normal CDF	1740.15	1667.23	95.81
Empirical CDF	1756.48	1604.2	91.33
Stochastic (all input variables)	1814.52	1702.11	93.80

4.2.3 Effects of GHI and Temperature on Energy Yield

The annual GHI and energy yield values were highly correlated according to the scatter plot in Figure 4.35. This is expected since the amount of incident solar radiation is the primary factor for solar PV energy output. However, the annual average daily mean temperature is negatively correlated with the energy yield according to Figure 4.36, and it is because of the relation between the PV cell temperature and PV module efficiency. It is important to note that GHI and ambient temperature affect the energy yield together; in other words, these are not

independent variables. It was also mentioned that temperature is the largest influencer on the PV energy yield in hotter locations, whereas irradiance is the most important one at any location [25]. It can be seen from Figure 4.37 that the lowest solar resource with a hot year was in 2016, which has the least energy yield estimations in the previous results. Therefore, the effect of GHI and temperature variability should be considered when estimating POE values of the energy yield. Here, the interannual variability of temperature was found as 1.82%; however, it does not consider the effect of climate change, and the projected values of the future temperature may not follow this variability range. In addition, since there is no energy production before sunrise and after sunset, obtaining the mean temperature during sunshine duration hours may represent the correlation between energy yield and ambient temperature better.

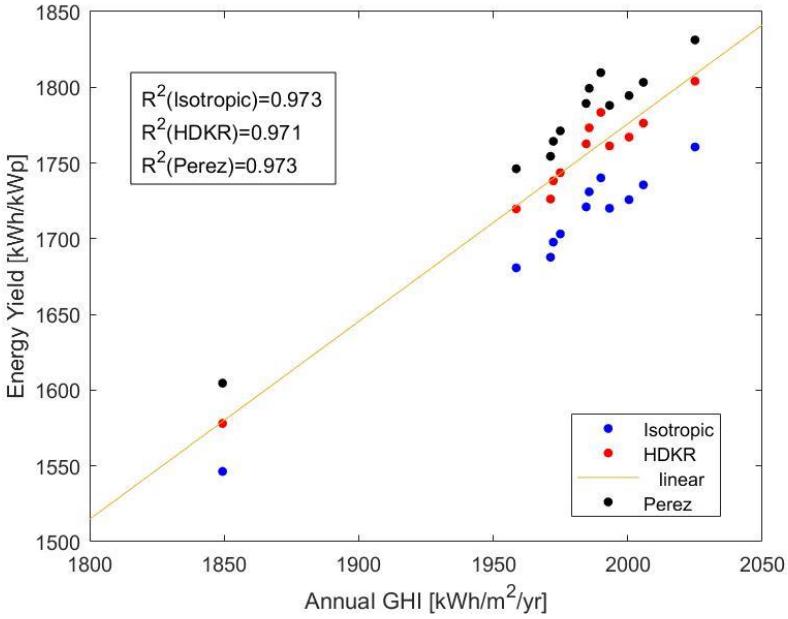

Figure 4.35. Correlation between the energy yield and annual GHI for time period 2005-2016.

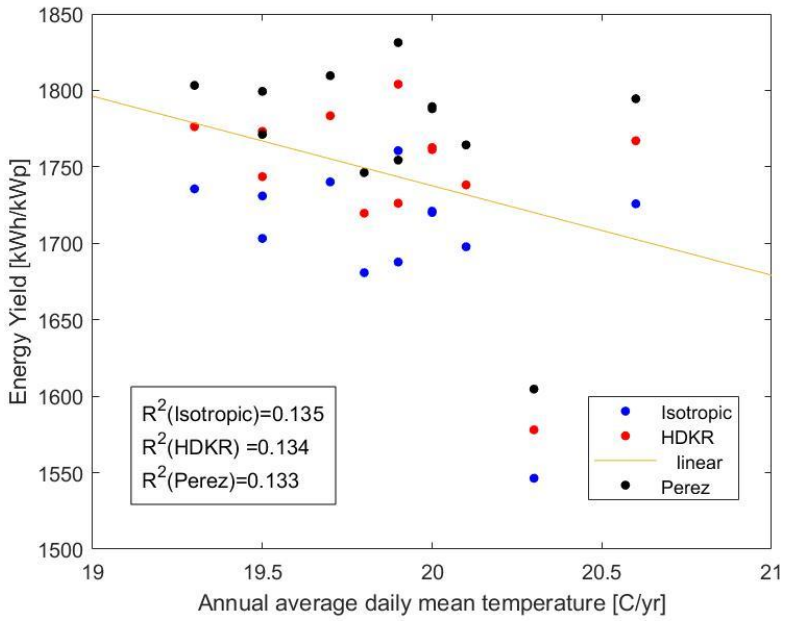

Figure 4.36. Correlation between the energy yield and annual average daily mean temperature for time period 2005-2016.

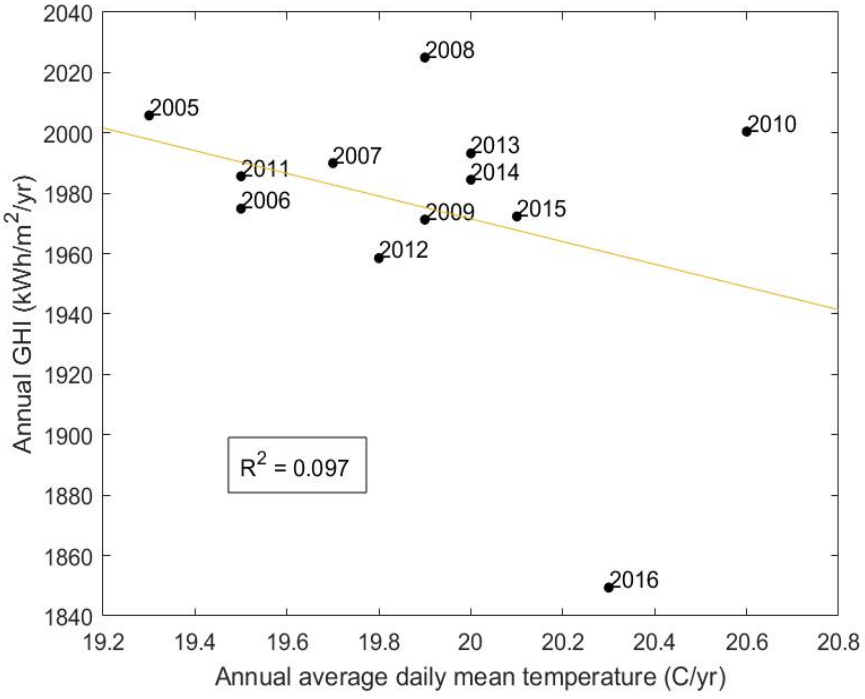

Figure 4.37. Correlation between annual GHI and annual average daily mean temperature between 2005-2016.

4.2.4 Overall Uncertainty

The sources of uncertainties of energy yield can be seen in Table 4.11. While the interannual variability of GHI is considered a random (stochastic) error, other uncertainty components are assumed as systematic errors. For the transposition model's uncertainty, converting GHI into POA irradiance varies by 2% for Isotropic, HDKR and Perez models. Also, using satellite-based data (PVGIS-SARAH) has an uncertainty of about 3.5% on solar radiation for the Cyprus region, whereas the interannual variability of GHI was found as 2.21% for the time period 2005-2016. On the other hand, the uncertainty related to dirt, soiling, shading and reflection of solar PV modules was assumed as 2%.

By using the rule of squares method, all uncertainty components were considered as independent from each other. As the overall uncertainty of energy yield was found as 7.08%, it can be further decreased by searching for other sources of error, which is assumed as 5%. For instance, temperature effects on the energy yield were not analyzed in detail in this study, and it can be considered other sources of error.

Table 4.11 Sources of uncertainties in percentages and the overall uncertainty of the energy yield.

Uncertainty Components	(%)	Reference
Satellite-based data	3.50	[54]
Transposition model (isotropic, HDKR, Perez)	2.00	Appendix A
Interannual variability of GHI	2.21	Table 4.7
Dirt, soiling, shading, reflection	2.00	[25]
Other sources of error	5.00	[26]
Overall uncertainty	7.08	

4.2.5 Levelized Cost of Electricity

Figure 4.38 shows the relationship between energy yield and LCOE in terms of POE values; in addition, TMY results are given at P50. As can be seen, the average of different TMY datasets did not match with the P50 range. The lowest energy yield with the highest LCOE belongs to the TMY2-Meteonorm dataset among other TMY results. The shaded bands were obtained by the standard deviation and mean values of energy yield and LCOE of three different models used in the calculations (isotropic, HDKR and Perez). Also, the inverse correlation between energy yield and LCOE introduces the non-exceedance probability values of LCOE. For example, the P90 value of the energy yield means that it will be met or exceeded with 90% probability at any time, while the LCOE will be less than or equal to the P90 value at nine-tenths of occurrence. On the other hand, the actual energy output data in 2016 and 2017 gives further information about the energy yield variations. The year 2016 is close to the P90 value, whereas 2017 passes the P10 value and stands maximum. Although including more annual data points will increase POE values' reliability, 12-year satellite-based data seem to represent the variabilities in the energy yield, according to the actual results. However, LCOE results depend on many financial assumptions, and this study only focused on the effects of energy yield on the LCOE. Therefore, it is possible to obtain lower LCOE values with the same energy yield data if the financial parameters in Table 3.9 are changed.

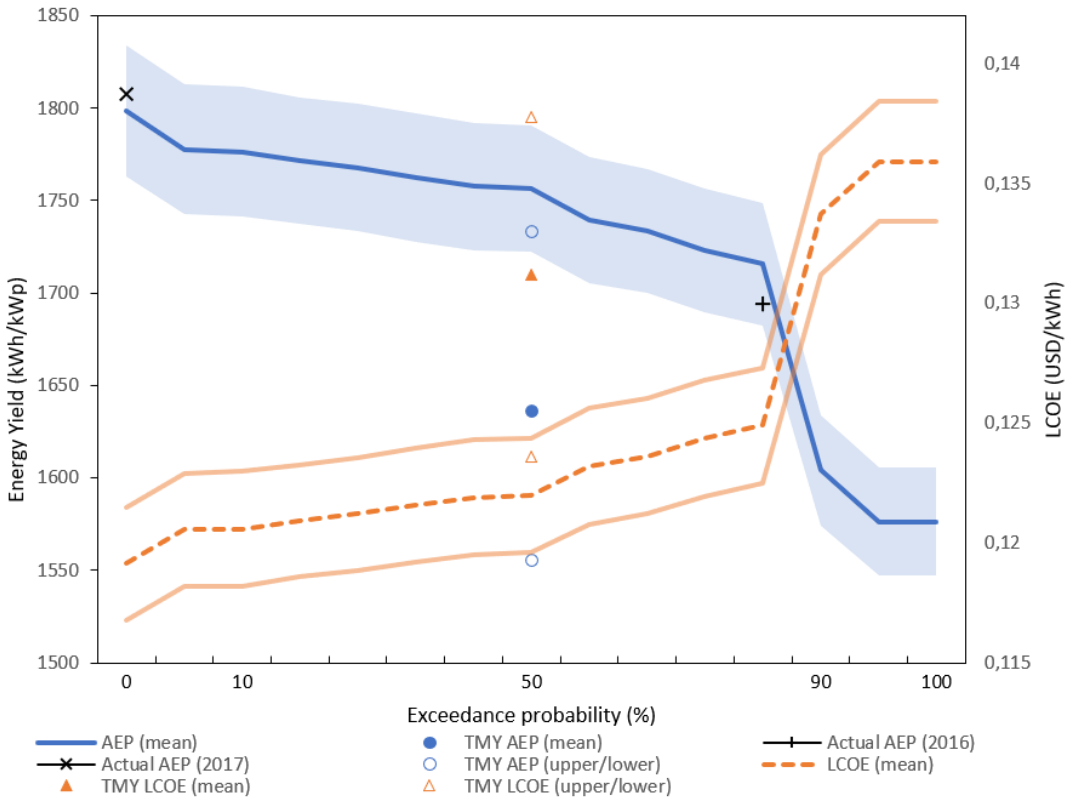

Figure 4.38. Exceedance and non-exceedance probabilities of AEP and LCOE with error bands, respectively. Actual energy yield data of 2016 and 2017 are shown at closest points to the mean energy yield line. Average results for different TMY datasets are represented in filled pointers, upper and lower bounds are obtained from specific TMY datasets (PVGIS-TMY, TMYx.2004-2018, TMY2-Meteonorm).

In Figure 4.39, stochastic simulation results of the energy yield and LCOE can be seen. Simulations were done multiple times to obtain a possible range, and the input variables in Table 3.8 were used in SAM. Main differences can be observed between Figures 4.39 and 4.40. For example, the range of energy yield increased, with a maximum value at about 2000 kWh/kWp and a minimum of about 1500 kWh/kWp. Similarly, LCOE results also changed. However, there is a significant change in the range, having values between 0.05 and 0.19 $/kWh. Since all financial parameters were kept constant in previous results, choosing a distribution for capital cost, fixed O&M cost and fixed charge rate affected the LCOE, as can be expected. The reason

is that all possible results were found considering the interannual variability of GHI by enabling weather file analysis for the time period 2005-2016. Therefore, it reduced the uncertainty and increased the confidence level of the POE values of energy yield and LCOE.

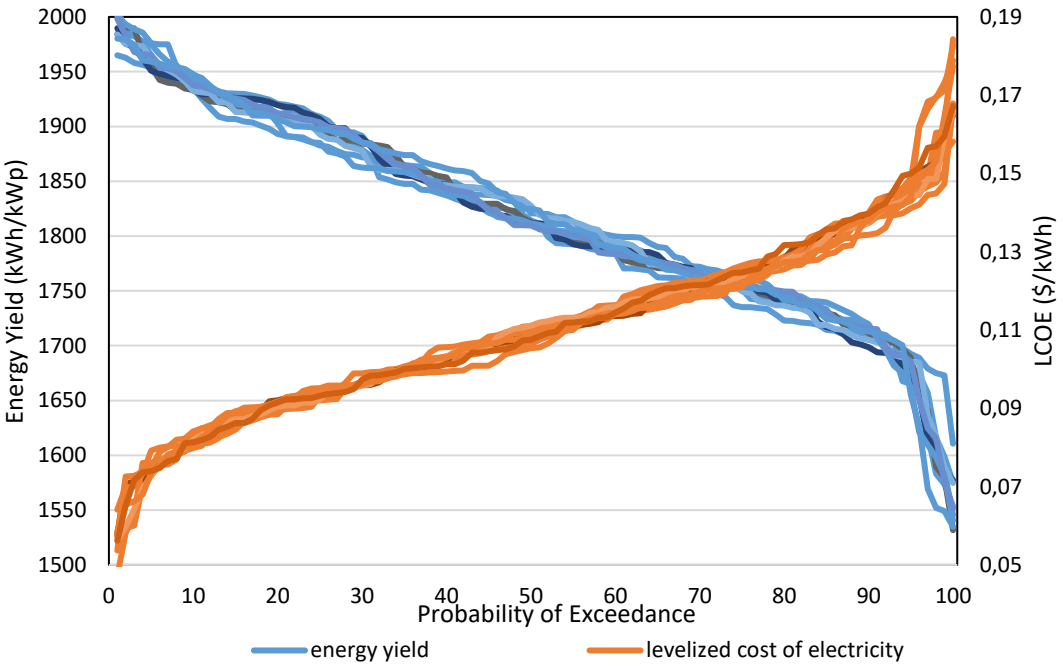

Figure 4.39. Probability of exceedance values of energy yield and LCOE, obtained from stochastic simulations.

CHAPTER 5

CONCLUSIONS AND FUTURE WORK

5.1 Conclusions

Penetration of large amounts of solar energy into the grid requires risk assessments since the solar resource is variable. Thus, energy exceedance probabilities such as P50 and P90 are calculated to statistically represent the energy yield in any year throughout the operational life of a solar power plant. Different methods exist to find the POE values, and there is no consensus in the research field. In this study, the empirical method was chosen to perform P50/P90 analysis for the solar PV plant located at METU NCC. Results were compared with the Normal distribution assumption, and it was found that empirical CDF gave more realistic results for P50 and P90. Stochastic simulations were also done to see the effects of all uncertainty components on energy yield by assuming probability distributions in SAM. It was found that stochastic simulations resulted in the highest POE values than the empirical method and Normal distribution assumption. For example, P50 and P90 values increased by 3.30% and 6.10% compared to the empirical method, respectively. Thus, detailed uncertainty analysis in a stochastic simulation can increase the expected energy yield and a project's bankability.

On the other hand, it was aimed to reduce the overall uncertainty using ground measurements, which have a shorter time period than satellite-based data. However, the quality assessment showed that GHI measurements had some erroneous data; thus, post-processing was done to reduce the RMSE of ground-measured GHI data. Several quality tests were made, and GHI was estimated using measured DNI for years of 2014, 2015 and 2016. While up to 2 hours of missing GHI data were filled by linear interpolation, longer missing data were filled by estimated GHI. Both measured and constructed GHI data were compared with satellite-based GHI data

for the time period 2010-2016. The results indicated that the average rRMSE of daily total GHI reduced from 34.63% to 17.77% after the data filing process. The rRMSE decreased to 8.78% for the annual mean daily total GHI data. Additionally, GTI was estimated using the isotropic sky-diffuse model, and it was compared with measured GTI. RMSE of daily total estimated GTI was 22.41%, whereas satellite-based GTI had an RMSE of 20.81%. Energy yield estimations were also compared using all datasets. For example, using SAM software reduced the energy yield by 14.74% on average compared to the calculations without using software.

According to empirical CDF results, the interannual variability of annual temperature, GHI, AEP and LCOE were found as about 1.82%, 2.21%, 3.26% and 3.50%, respectively. Although the LCOE is found through the operational lifetime of a plant, this study aimed to see the variations of LCOE with respect to possible AEP values. According to the comparison of TMY and P50 values, it was found that an average TMY underpredicted the annual GHI and AEP by 5.15% and 6.82%, respectively, while it overpredicted the LCOE by 7.53%. It was also found that AEP is highly correlated with annual GHI, whereas, a negative correlation was found with the annual average daily mean temperature. LCOE values were also found in stochastic simulation by enabling uncertainty distributions for the capital cost, annual operational cost and the fixed charge rate. The range of LCOE was found between 0.05 and 0.19 $/kWh, while energy yield had a range between 1500 and 2000 kWh/kWp.

In conclusion, while using TMY datasets can give a fast prediction of the long-term average energy yield, multi-year historical data sets are required to understand the long-term trends of solar resources and to obtain POE values of energy yield. In addition, the assumptions while doing calculations matter when the results are compared with actual energy yield data. Using a quality-checked, high accurate dataset also matters since it directly affects energy yield estimates. It is important to mention that long-term ground measurements may not always be available and even if it exists, regular calibration and maintenance of the ground station is necessary to obtain accurate measurements. Therefore, satellite-based data can be used as long-

term reference data when doing a detailed analysis. Besides, measuring GTI with a tilted pyranometer can give a better value than estimating GTI from GHI and DNI; however, its quality should also be checked. In this study, the interannual variability of GHI was found as about 2.21% and 5.94% with satellite-based and ground-measured data, respectively. Both results show that COV is below 6%, which is considered low [20]. The P50 value of energy yield was also found as 1756.48 and 1814.52 kWh/kWp with the empirical method and stochastic simulations, respectively, whereas 1604.2 and 1702.11 kWh/kWp were found for the P90 value with the empirical method and stochastic simulations, respectively. This means that higher P50 and P90 values can be estimated by doing more detailed uncertainty analyses; as a result, the project's bankability increases.

Considering these results, making new solar PV plant investments is suitable for this region, and confidence levels such as P90 and P50 values were found, which can be used by project developers and investors in the future. LCOE results also show that installing a solar PV power plant is feasible in this region.

5.2 Future Work

In this study, historical weather datasets were used to see the interannual variability of GHI, to estimate the energy yield with the POE values and the LCOE estimates. Further study can include the effects of climate change on weather parameters, and projected weather datasets can be used. Including recent years' weather data and extending the time period of the dataset will also make the long-term trend of solar radiation more reliable, thus, the energy and economic yield results. Furthermore, the lack of high-quality ground measurements showed the importance of collecting solar radiation data from nearby ground stations for validation. It will also help to do a spatial analysis if there are more ground-measured data from nearby stations.

Also, uncertainty components of the energy yield such as temperature, dirt and soiling should be further investigated since reducing the overall uncertainty will

increase the confidence level of energy yield estimates. The uncertainty components may also have some correlations with each other, which was not considered in stochastic simulations. On the other hand, different methods were applied to estimate the POE values of energy yield. Further study may include obtaining a perfect weighted linear combination of these methods. In addition, synthetic weather datasets can be generated for different POE scenarios.

The methodology explained in this thesis was applied to the 1 MWp solar PV plant in METU NCC as a case study; however, it can also be applied to a hypothetical large-scale plant if a new renewable energy project will be planned to be installed. This study can be expanded to analyze CSP and wind energy projects as well.

Finally, economic analysis can be further done; for example, project revenues, debt-size coverage ratio (DSCR), and net present value can be calculated in addition to the LCOE. Financial parameters can also be considered in detail, such as taxes, subsidies, and incentives.

REFERENCES

[1] IRENA, “Global Energy Transformation: A Roadmap to 2050,” Abu Dhabi, 2019.

[2] P. D. Lund, J. A. Byrne, R. Haas, and D. Flynn, “PART IV: Changing Electricity Markets. Designing Electricity Markets for a High Penetration of Variable Renewables,” in *ADVANCES IN ENERGY SYSTEMS: The Large-scale Renewable Energy Integration Challenge*, John Wiley & Sons Ltd, 2019, pp. 479–491.

[3] R. Pacudan, “Implications of applying solar industry best practice resource estimation on project financing,” *Energy Policy*, vol. 95, pp. 489–497, 2016.

[4] A. Habte *et al.*, “Best Practices Handbook for the Collection and Use of Solar Resource Data for Solar Energy Applications: Second Edition, NREL,” 2017.

[5] A. C. Mcmahan, C. N. Grover, and F. E. Vignola, “Evaluation of Resource Risk in Solar-Project Financing,” in *Solar Energy Forecasting and Resource Assessment*, Elsevier, 2013, pp. 81–95.

[6] J. Polo, F. M. Téllez, and C. Tapia, “Comparative analysis of long-term solar resource and CSP production for bankability,” *Renew. Energy*, vol. 90, pp. 38–45, 2016.

[7] F. Vignola, C. Grover, and N. Lemon, “Building a bankable solar radiation dataset,” *40th ASES Natl. Sol. Conf. 2011, Sol. 2011*, vol. 1, no. 8, pp. 705–712, 2011.

[8] A. Lopez and G. Maclaurin, “Capturing Inter-Annual Variability of PV Energy Production in South Asia,” 2017.

[9] S. A. Kalogirou, “Environmental Characteristics, 2.4. The solar resource,” in *Solar Energy Engineering - Processes and Systems*, 2nd ed., Elsevier, 2014, pp. 109–123.

[10] S. Pelland, C. Maalouf, R. Kenny, L. Leahy, B. Schneider, and G. Bender, “Solar energy assessments: When is a typical meteorological year good enough?,” *Sol. 2016 - Am. Sol. Energy Soc. Natl. Sol. Conf. 2016 Proc.*, pp. 77–83, 2016.

[11] F. E. Vignola, A. C. McMahan, and C. N. Grover, “Bankable Solar-Radiation Datasets,” in *Solar Energy Forecasting and Resource Assessment*, Elsevier, 2013, pp. 97–131.

[12] T. Cebecauer and M. Suri, “Typical Meteorological Year Data: SolarGIS Approach,” *Energy Procedia*, vol. 69, pp. 1958–1969, 2015.

[13] A. Tadesse, A. Kankiewicz, A. Kubiniec, R. Perez, J. Dise, and T. Hoff, "Advances in long-term solar energy prediction and project risk assessment methodology," in *2017 IEEE 44th Photovoltaic Specialist Conference (PVSC)*, 2017, pp. 132–137.

[14] C. M. Fernández-Peruchena, M. Gastón, M. Sánchez, J. García-Barberena, M. Blanco, and A. Bernardos, "MUS: A multiscale stochastic model for generating plausible meteorological years designed for multiyear solar energy yield simulations," *Sol. Energy*, vol. 120, pp. 244–256, 2015.

[15] C. M. Fernández-Peruchena *et al.*, "Probabilistic assessment of concentrated solar power plants yield: The EVA methodology," *Renew. Sustain. Energy Rev.*, vol. 91, no. July 2016, pp. 802–811, 2018.

[16] J. Polo *et al.*, "Preliminary survey on site-adaptation techniques for satellite-derived and reanalysis solar radiation datasets," *Sol. Energy*, vol. 132, pp. 25–37, 2016.

[17] S. M. S. Sadati, E. Jahani, O. Taylan, and D. K. Baker, "Sizing of Photovoltaic-Wind-Battery Hybrid System for a Mediterranean Island Community Based on Estimated and Measured Meteorological Data," *J. Sol. Energy Eng. Trans. ASME*, vol. 140, no. 1, pp. 1–12, 2018.

[18] "Goal 7 | Department of Economic and Social Affairs." [Online]. Available: https://sdgs.un.org/goals/goal7. [Accessed: 20-Jan-2021].

[19] J. A. Duffie, W. A. Beckman, and J. McGowan, *Solar Engineering of Thermal Processes*, 4th ed. University of Wisconsin-Madison, 2005.

[20] S. Marcel, H. Thomas, D. Ewan, A. Michel, L. Mireille, and W. Lucien, "Uncertainties in solar electricity yield prediction from fluctuation of solar radiation," in *Proceedings of the 22nd European Photovoltaic Solar Energy Conference*, 2007, pp. 3547–3552.

[21] S. A. Kalogirou, "Wind Energy Systems," in *Solar Energy Engineering - Processes and Systems*, 2nd ed., Elsevier, 2014, pp. 735–762.

[22] C. M. Fernández Peruchena *et al.*, "A statistical characterization of the long-term solar resource: Towards risk assessment for solar power projects," *Sol. Energy*, vol. 123, no. January, pp. 29–39, 2016.

[23] A. P. Dobos and M. Kasberg, "WREF 2012 : P50/P90 Analysis for Solar Energy Systems Using the System Advisor Model," in *World Renewable Energy Forum*, 2012.

[24] S. Y. Kim, B. Sapotta, G. Jang, Y. Kang, and H. Kim, "Prefeasibility Study of Photovoltaic Power Potential Based on a Skew-Normal Distribution," *Energies*, pp. 1–12, 2020.

[25] C. Reise, B. Müller, D. Moser, G. Belluardo, and P. Ingenhoven,

"Uncertainties in PV System Yield Predictions and Assessments, IEA PVPS Task 13, Subtasks 2.3 & 3.1," 2018.

[26] D. Thevenard and S. Pelland, "Estimating the uncertainty in long-term photovoltaic yield predictions," *Sol. Energy*, vol. 91, pp. 432–445, 2013.

[27] G. Belluardo, M. Herz, U. Jahn, M. Richter, and D. Moser, "Evaluation of uncertainty in PV project design: definition of scenarios and impact on energy yield predictions," in *2017 IEEE 44th Photovoltaic Specialist Conference (PVSC)*, 2017, pp. 3360–3365.

[28] A. Clifton, A. Smith, and M. Fields, "Wind Plant Preconstruction Energy Estimates : Current Practice and Opportunities, NREL," 2016.

[29] B. Müller, M. Wild, A. Driesse, and K. Behrens, "Rethinking solar resource assessments in the context of global dimming and brightening," *Sol. Energy*, vol. 99, pp. 272–282, 2014.

[30] M. Schnitzer, C. Thuman, and P. Johnson, "REDUCING UNCERTAINTY IN SOLAR ENERGY ESTIMATES: Mitigating Energy Risk through On-Site Monitoring," 2012.

[31] R. Perez and T. E. Hoff, "Solar resource variability," in *Solar Energy Forecasting and Resource Assessment*, Elsevier, 2013, pp. 133–146.

[32] R. Bryce, I. Losada Carreño, A. Kumler, B. M. Hodge, B. Roberts, and C. Brancucci Martinez-Anido, "Consequences of neglecting the interannual variability of the solar resource: A case study of photovoltaic power among the Hawaiian Islands," *Sol. Energy*, vol. 167, no. June, pp. 61–75, 2018.

[33] S. Dubey, J. N. Sarvaiya, and B. Seshadri, "Temperature dependent photovoltaic (PV) efficiency and its effect on PV production in the world - A review," *Energy Procedia*, vol. 33, pp. 311–321, 2013.

[34] F. Y. Ettoumi, A. Mefti, A. Adane, and M. Y. Bouroubi, "Statistical analysis of solar measurements in Algeria using beta distributions," *Renew. Energy*, vol. 26, no. 1, pp. 47–67, 2002.

[35] M. Bolinger, "Using Probability of Exceedance to Compare the Resource Risk of Renewable and Gas-Fired Generation," 2017.

[36] A. Abdulkarim, S. M. Abdelkader, and J. Morrow, "Statistical Analyses of Wind and Solar Energy Resources for the Development of Hybrid Microgrid," *Springer Proc. Energy*, no. July, 2015.

[37] H. Cherif and J. Belhadj, "Energy output estimation of hybrid Wind-Photovoltaic power system using statistical distributions," *J. Electr. Syst.*, vol. 10, no. 2, pp. 117–132, 2014.

[38] G. Bender, F. Davidson, S. Eichelberger, and C. A. Gueymard, "The road to bankability: Improving assessments for more accurate financial planning," in

40th ASES National Solar Conference 2011, SOLAR 2011, 2011, vol. 1, no. January 2011, pp. 733–738.

[39] J. Polo *et al.*, "Integration of ground measurements to model derived data: A report of IEA SHC Task 46 Solar Resource Assessment and Forecasting," 2015.

[40] J. S. Stein and B. Farnung, "PV Performance Modeling Methods and Practices Results from the 4th PV Performance Modelling Collaborative Workshop," 2017.

[41] S. Younes, R. Claywell, and T. Muneer, "Quality control of solar radiation data: Present status and proposed new approaches," *Energy*, vol. 30, no. 9 SPEC. ISS., pp. 1533–1549, 2005.

[42] S. Pashiardis and S. A. Kalogirou, "Quality control of solar shortwave and terrestrial longwave radiation for surface radiation measurements at two sites in Cyprus," *Renew. Energy*, vol. 96, pp. 1015–1033, 2016.

[43] M. Journée and C. Bertrand, "Quality control of solar radiation data within the RMIB solar measurements network," *Sol. Energy*, vol. 85, no. 1, pp. 72–86, 2011.

[44] K. Branker, M. J. M. Pathak, and J. M. Pearce, "A review of solar photovoltaic levelized cost of electricity," *Renew. Sustain. Energy Rev.*, vol. 15, no. 9, pp. 4470–4482, 2011.

[45] W. Short, D. Packey, and T. Holt, "A Manual for the Economic Evaluation of Energy Efficiency and Renewable Energy Technologies," Golden, Colorado, National Renewable Energy Laboratory (NREL), 1995.

[46] O. Taylan, "Sizing of Photovoltaic and Wind Energy Systems by Techno-Economic Analysis: Effects of Discount Rate and Feed-in-tariff," *DEUFMD*, vol. 21, no. 63, pp. 879–895, 2019.

[47] L. Al-Ghussain, R. Samu, O. Taylan, and M. Fahrioğlu, "Hydrogen Fuel Cell / Pumped Hydro Storage System for Micro Grid Applications : Case Study in Cyprus," in *2018 International Conference on Photovoltaic Science and Technologies (PVCon)*, 2018.

[48] G. Taylan, O. Taylan, and M. Fahrioglu, "Comparison of Middle-Sized PTC and PV Power Plants for METU NCC," *World J. Environ. Res.*, vol. 8, no. 2, pp. 53–59, 2018.

[49] S. M. S. Sadati, E. Jahani, and O. Taylan, "Technical and Economic Analyses for Sizing PV Power Plant With Storage System for METU NCC," 2015.

[50] "Meteonorm Software." [Online]. Available: https://meteonorm.com/. [Accessed: 02-Aug-2020].

[51] L. Lawrie and D. Crawley, "Development of Global Typical Meteorological

Years (TMYx)," 2019. [Online]. Available: http://climate.onebuilding.org. [Accessed: 02-Aug-2020].

[52] "JRC Photovoltaic Geographical Information System (PVGIS) - European Commission." [Online]. Available: https://re.jrc.ec.europa.eu/pvg_tools/en/#TMY. [Accessed: 02-Aug-2020].

[53] T. Huld, R. Müller, and A. Gambardella, "A new solar radiation database for estimating PV performance in Europe and Africa," *Sol. Energy*, vol. 86, no. 6, pp. 1803–1815, 2012.

[54] A. G. Amillo, T. Huld, and R. Müller, "A new database of global and direct solar radiation using the eastern meteosat satellite, models and validation," *Remote Sens.*, vol. 6, no. 9, pp. 8165–8189, 2014.

[55] M. Geiger, L. Diabaté, L. Ménard, and L. Wald, "A web service for controlling the quality of measurements of global solar irradiation," *Sol. Energy*, vol. 73, no. 6, pp. 475–480, 2002.

[56] D. G. Erbs, S. A. Klein, and J. A. Duffie, "Estimation of the diffuse radiation fraction for hourly, daily and monthly-average global radiation," *Sol. Energy*, vol. 28, no. 4, pp. 293–302, 1982.

[57] A. Sanchez-Lorenzo, J. Calbó, and M. Wild, "Global and diffuse solar radiation in Spain: Building a homogeneous dataset and assessing their trends," *Glob. Planet. Change*, vol. 100, pp. 343–352, 2013.

[58] C. C. Turrado, M. López, F. S. Lasheras, B. A. Gómez, J. L. Rollé, and F. J. Juez, "Missing Data Imputation of Solar Radiation Data under Different Atmospheric Conditions," *Sensors*, vol. 14, pp. 20382–20399, 2014.

[59] E. F. M. Abreu, P. Canhoto, V. Prior, and R. Melicio, "Solar resource assessment through long-term statistical analysis and typical data generation with different time resolutions using GHI measurements," *Renew. Energy*, vol. 127, pp. 398–411, 2018.

[60] "AXITEC AC-250P/156-60S." [Online]. Available: https://www.axitecsolar.com/data/solarpanels_documents/DB_60zlg_AXIplus SE_poly_power_MiA_US.pdf. [Accessed: 13-May-2020].

[61] L. P. Swiler and G. D. Wyss, "A User's Guide to LHS: Sandia's Latin Hypercube Sampling Software," 1998.

[62] M. Cambell, "The Drivers of the Levelized Cost of Electricity for Utility-Scale Photovoltaics," SUNPOWER, 2008.

[63] S. B. Darling, F. You, T. Veselka, and A. Velosa, "Assumptions and the levelized cost of energy for photovoltaics," *Energy Environ. Sci.*, vol. 4, no. 9, pp. 3133–3139, 2011.

[64] "OpenEI | Transparent Cost Database." [Online]. Available:

https://openei.org/apps/TCDB/#blank. [Accessed: 14-Jul-2020].

[65] C. A. Gueymard and S. M. Wilcox, “Spatial and temporal variability in the solar resource: Assessing the value of short-term measurements at potential solar power plant sites,” in *38th ASES National Solar Conference 2009, SOLAR 2009*, 2009, vol. 5, no. June, pp. 3026–3053.

[66] M. Lave, W. Hayes, A. Pohl, and C. W. Hansen, “Evaluation of global horizontal irradiance to plane-of-array irradiance models at locations across the United States,” *IEEE J. Photovoltaics*, vol. 5, no. 2, pp. 597–606, 2015.

APPENDICES

A. SAM simulation results of temperature, GHI, POA, AEP and LCOE using different TMY and satellite-based datasets with different transposition models used (Isotropic, HDKR, Perez). Statistical indices are also shown.

Transposition model			Isotropic			HDKR			Perez		
Dataset	Temperature (℃/yr)	GHI (kWh/m2/yr)	POA (kWh/m2/yr)	AEP (MWh/yr)	LCOE (USD/kWh)	POA (kWh/m2/yr)	AEP (MWh/yr)	LCOE (USD/kWh)	POA (kWh/m2/yr)	AEP (MWh/yr)	LCOE (USD/kWh)
TMY2-Meteonorm	19.7	1811.89	1957.49	1523.77	0.141	2004.08	1557.65	0.138	2042.88	1585.67	0.135
deviation of TMY from P50 (%)	-1.01	-8.70	-9.69	-11.41	12.89	-9.89	-11.56	13.08	-9.64	-11.32	12.76
TMYx.2004-2018	17.9	1880.1	2032.67	1589.08	0.135	2082.53	1624.98	0.132	2115.20	1648.33	0.130
deviation of TMY from P50 (%)	-10.05	-5.26	-6.23	-7.62	8.25	-6.37	-7.74	8.39	-6.45	-7.81	8.47
PVGIS-TMY (2007-2016)	19.7	1954.73	2133.71	1698.17	0.126	2189.69	1739.05	0.123	2223.39	1763.55	0.121
deviation of TMY from P50 (%)	-1.01	-1.50	-1.57	-1.28	1.29	-1.55	-1.26	1.28	-1.66	-1.37	1.39
PVGIS-SARAH	Temperature (℃/yr)	GHI (kWh/m2/yr)	POA (kWh/m2/yr)	AEP (MWh/yr)	LCOE (USD/kWh)	POA (kWh/m2/yr)	AEP (MWh/yr)	LCOE (USD/kWh)	POA (kWh/m2/yr)	AEP (MWh/yr)	LCOE (USD/kWh)
2005	19.3	2005.80	2176.53	1735.6	0.123	2231.66	1776.3	0.121	2268.43	1803.29	0.119
2006	19.5	1974.91	2137.68	1703.2	0.126	2192.16	1743.62	0.123	2229.91	1771.22	0.121
2007	19.7	1989.99	2184.08	1740.19	0.123	2242.97	1783.44	0.120	2279.13	1809.66	0.118
2008	19.9	2024.99	2211.28	1760.59	0.122	2270.10	1804.02	0.119	2307.67	1831.25	0.117
2009	19.9	1971.29	2125.85	1687.79	0.127	2178.17	1726.24	0.124	2216.77	1754.43	0.122
2010	20.6	2000.47	2177.78	1725.82	0.124	2234.71	1767.08	0.121	2272.61	1794.54	0.119
2011	19.5	1985.66	2176.39	1730.98	0.124	2234.52	1773.22	0.121	2270.66	1799.35	0.119
2012	19.8	1958.54	2123.20	1680.78	0.127	2177.15	1719.69	0.125	2213.88	1746.22	0.123
2013	20.0	1993.22	2167.63	1720.12	0.125	2224.11	1761.31	0.122	2260.95	1788.01	0.120
2014	20.0	1984.52	2168.36	1721.01	0.124	2226.07	1762.63	0.122	2263.13	1789.35	0.120
2015	20.1	1972.33	2149.67	1697.74	0.126	2206.01	1738.24	0.123	2242.53	1764.34	0.121
2016	20.3	1849.40	1974.00	1546.37	0.139	2017.70	1578.03	0.136	2054.27	1604.67	0.133
POA/GHI	–	–	1.09	–	–	1.11	–	–	1.13	–	–
min	19.3	1849.40	1974.00	1546.37	0.122	2017.70	1578.03	0.119	2054.27	1604.67	0.117
max	20.6	2024.99	2211.28	1760.59	0.139	2270.10	1804.02	0.136	2307.67	1831.25	0.133
st.dev.	0.36	43.60	60.38	54.73	0.0043	64.42	57.77	0.0044	64.47	57.80	0.0042
mean	19.88	1975.93	2147.70	1704.18	0.126	2202.94	1744.49	0.123	2239.99	1771.36	0.121
COV (%)	1.82	2.21	2.81	3.21	3.44	2.92	3.31	3.56	2.88	3.26	3.50
P90	19.34	1871.23	2003.84	1573.26	0.136	2049.59	1606.36	0.134	2086.19	1632.98	0.131
P75	19.5	1971.29	2125.85	1687.79	0.127	2178.17	1726.24	0.124	2216.77	1754.43	0.122
P50	19.9	1984.52	2167.63	1720.12	0.125	2224.11	1761.31	0.122	2260.95	1788.01	0.120
P25	20.0	1993.22	2176.53	1730.98	0.124	2234.52	1773.22	0.121	2270.66	1799.35	0.119
P10	20.26	2004.74	2182.82	1739.27	0.123	2241.32	1782.01	0.120	2277.83	1808.38	0.118

B. Computing sample example of stochastic simulation in SAM software.

#	Sky Diffuse Model	Weather Files	AC Wiring Loss (%)	DC Wiring Loss (%)	Connection & Diodes Loss (%)	Module Mismatch Loss (%)	Nameplate Loss (%)	Temperature Correction Model	Self-shading model
1	HDKR	2005.csv	1.00677	1.76329	0.555047	2.27482	3.30452	NOCT	Thin film
2	Perez	2009.csv	1.0336	2.25686	0.517775	1.95549	3.19197	Heat transfer	Thin film
3	Isotropic	2014.csv	1.1346	1.21063	0.488541	2.20349	2.83668	Heat transfer	Standard
4	HDKR	2005.csv	1.17583	1.99724	0.423304	2.09567	2.79037	Heat transfer	Standard
5	HDKR	2005.csv	1.1163	2.04943	0.430098	2.01423	3.71634	NOCT	None
6	Perez	2013.csv	0.98252	1.71942	0.579054	2.50639	3.28744	Heat transfer	Standard
7	Perez	2010.csv	0.867895	2.21192	0.522913	2.32979	2.67337	Heat transfer	Thin film
8	HDKR	2012.csv	1.05007	2.06122	0.562842	2.12675	2.98828	Heat transfer	None
9	Isotropic	2005.csv	0.935981	1.62907	0.552045	1.71181	3.38354	Heat transfer	None
10	Perez	2008.csv	0.750419	2.32789	0.406574	2.31341	3.58773	NOCT	None
11	Isotropic	2011.csv	0.848805	2.25078	0.44677	2.04614	3.01686	NOCT	Thin film
12	Isotropic	2013.csv	0.86879	1.43576	0.481454	2.34398	2.54125	NOCT	Thin film
13	Perez	2011.csv	0.876918	2.30207	0.497143	1.13595	3.18105	Heat transfer	Standard
14	HDKR	2015.csv	1.08413	1.88648	0.485451	1.75994	2.48086	NOCT	Thin film
15	HDKR	2008.csv	1.15647	2.5654	0.540458	1.81516	3.41922	NOCT	None
16	HDKR	2011.csv	1.02653	2.10412	0.543414	1.88023	3.09078	Heat transfer	Thin film
17	HDKR	2012.csv	1.05846	1.91731	0.520772	2.07238	3.20312	NOCT	None
18	HDKR	2010.csv	1.22811	1.96714	0.491545	1.51128	3.14855	Heat transfer	Standard
19	HDKR	2015.csv	0.931554	2.31824	0.514792	2.08802	3.06497	NOCT	None
20	Isotropic	2016.csv	0.697413	1.75257	0.525117	1.80014	3.23528	NOCT	Standard
21	HDKR	2011.csv	0.856385	2.12451	0.464565	2.21365	3.5111	Heat transfer	None
22	HDKR	2009.csv	1.12968	1.79616	0.414024	2.62409	2.12824	NOCT	None
23	Perez	2014.csv	0.98583	2.00296	0.609107	1.99205	3.33062	NOCT	Standard
24	Isotropic	2007.csv	1.03932	1.64847	0.408087	1.94141	2.80573	Heat transfer	Thin film
25	Isotropic	2010.csv	1.2817	2.34674	0.314831	2.25229	3.45837	NOCT	Thin film
26	Perez	2012.csv	1.19409	1.94561	0.364741	1.7237	3.06918	NOCT	None
27	Isotropic	2010.csv	0.859242	1.9036	0.532686	1.87243	2.89961	NOCT	None
28	Perez	2006.csv	1.07975	1.97896	0.511608	2.36199	3.29097	NOCT	None
29	Isotropic	2015.csv	1.25129	1.87793	0.461309	2.14081	3.5694	Heat transfer	Thin film
30	HDKR	2012.csv	0.722297	1.9376	0.504659	2.06488	2.21293	NOCT	None
31	HDKR	2006.csv	0.890822	1.57942	0.52887	1.69535	2.97619	NOCT	Thin film
32	Perez	2014.csv	0.883931	2.16887	0.595937	2.19265	2.99461	NOCT	Thin film
33	HDKR	2014.csv	0.947579	2.07844	0.559469	2.25297	3.48622	Heat transfer	Standard
34	HDKR	2010.csv	0.921175	1.77441	0.396845	2.42457	2.88351	NOCT	Standard
35	Isotropic	2011.csv	1.06493	1.86438	0.509493	1.82239	2.40433	NOCT	Standard
36	Perez	2006.csv	1.31067	2.54471	0.581494	1.68612	2.30576	NOCT	Standard
37	Perez	2012.csv	1.05473	2.28567	0.498619	2.22632	2.58036	NOCT	Standard
38	Perez	2007.csv	1.06717	2.26567	0.495313	2.37516	2.76097	Heat transfer	None
39	Isotropic	2009.csv	0.954283	1.80387	0.478555	1.73768	3.25956	Heat transfer	Thin film
40	Perez	2008.csv	1.12406	2.23714	0.5093	2.176	3.66556	Heat transfer	None
41	Perez	2015.csv	0.838074	2.03635	0.377995	1.97991	2.74662	Heat transfer	Standard
42	HDKR	2005.csv	0.621051	1.81887	0.479652	1.89274	3.43718	NOCT	Standard
43	Perez	2016.csv	1.14123	1.94943	0.456277	1.64001	2.69105	NOCT	None
44	HDKR	2005.csv	0.910512	2.01352	0.537461	2.16395	3.16016	Heat transfer	Thin film
45	Isotropic	2014.csv	0.988782	1.37443	0.393599	2.59138	2.77736	Heat transfer	None

46	Isotropic	2015.csv	1.09754	2.36984	0.576235	2.38905	2.96388	Heat transfer	Standard
47	HDKR	2016.csv	1.10153	1.69776	0.450176	2.17441	2.91649	NOCT	Thin film
48	Isotropic	2010.csv	1.10688	1.86997	0.48326	1.78165	3.78382	NOCT	Thin film
49	Perez	2015.csv	0.950244	2.05474	0.388069	1.75035	2.88912	Heat transfer	Standard
50	HDKR	2009.csv	1.09487	2.40056	0.566563	1.96329	2.73387	NOCT	None
51	Isotropic	2016.csv	0.96134	2.15218	0.50315	1.91574	3.27179	NOCT	Thin film
52	HDKR	2005.csv	0.944447	2.43848	0.51575	1.83183	3.48368	NOCT	Standard
53	Isotropic	2013.csv	0.929752	1.49748	0.535066	2.1565	3.00398	Heat transfer	Thin film
54	HDKR	2008.csv	1.38554	1.91136	0.46786	1.88623	2.55961	NOCT	Thin film
55	Isotropic	2008.csv	1.2148	2.11583	0.590014	1.84336	2.59759	NOCT	None
56	Perez	2010.csv	1.14823	1.57086	0.400653	1.35032	2.61842	NOCT	None
57	HDKR	2007.csv	0.999041	1.67202	0.641404	2.19672	4.12102	NOCT	Thin film
58	HDKR	2006.csv	1.07561	2.03003	0.616442	1.59741	2.7669	Heat transfer	Standard
59	HDKR	2014.csv	1.01247	2.45908	0.546778	2.05752	2.85938	NOCT	Standard
60	HDKR	2011.csv	0.993229	1.81323	0.489328	2.29578	3.3559	NOCT	Thin film
61	Isotropic	2011.csv	0.81498	1.74191	0.784723	1.99275	3.23703	Heat transfer	Standard
62	Perez	2007.csv	0.899168	2.16338	0.334488	1.76988	3.13335	Heat transfer	None
63	Isotropic	2007.csv	1.04364	2.6268	0.493549	1.44012	2.65949	Heat transfer	None
64	Perez	2014.csv	0.81738	1.5465	0.529444	1.60474	1.94632	NOCT	Standard
65	HDKR	2014.csv	0.656679	2.52175	0.58622	2.14012	3.11776	Heat transfer	Standard
66	Isotropic	2013.csv	1.00868	2.01554	0.441513	2.08028	2.63175	Heat transfer	Standard
67	Isotropic	2009.csv	1.16407	1.8973	0.443106	2.53536	3.37814	Heat transfer	None
68	Isotropic	2014.csv	1.09034	2.18994	0.550409	1.93661	2.63965	Heat transfer	Standard
69	Isotropic	2012.csv	1.30018	1.95743	0.452351	1.83519	3.79333	NOCT	Standard
70	HDKR	2005.csv	0.916435	2.06951	0.469523	1.906	2.38244	NOCT	Thin film
71	Perez	2016.csv	0.906831	2.08459	0.436868	1.97603	3.55146	Heat transfer	Thin film
72	Perez	2013.csv	1.01777	2.14751	0.474712	1.61733	2.95249	NOCT	Standard
73	Perez	2011.csv	0.976487	1.4702	0.43918	2.02263	3.03043	NOCT	Thin film
74	Isotropic	2008.csv	0.96831	2.11012	0.37396	2.10199	2.44656	NOCT	None
75	Perez	2009.csv	1.15004	1.98894	0.459203	2.8008	2.71788	Heat transfer	Thin film
76	HDKR	2009.csv	0.922696	2.20657	0.500129	1.56621	3.40147	NOCT	None
77	Perez	2010.csv	0.979978	1.51444	0.629836	1.73393	3.64448	NOCT	Thin film
78	HDKR	2006.csv	0.941242	1.72607	0.564781	2.30583	3.16175	Heat transfer	None
79	Perez	2006.csv	0.884325	1.71073	0.605014	1.92507	2.87028	NOCT	Thin film
80	Isotropic	2015.csv	1.04612	2.71393	0.640516	2.49099	1.99425	Heat transfer	None
81	Perez	2013.csv	1.23332	1.85889	0.506092	2.00055	3.33545	Heat transfer	Thin film
82	Perez	2015.csv	0.807335	2.041	0.352652	1.65197	4.00545	Heat transfer	None
83	Perez	2008.csv	0.898033	1.97449	0.569675	2.44436	2.81878	Heat transfer	Thin film
84	Perez	2016.csv	1.07064	1.82914	0.471973	1.85812	2.50489	Heat transfer	Standard
85	Isotropic	2008.csv	0.971783	2.28991	0.422085	1.9512	2.16833	Heat transfer	Thin film
86	Isotropic	2012.csv	1.02183	2.22935	0.418764	1.66355	3.6139	Heat transfer	Thin film
87	HDKR	2008.csv	1.11094	1.92593	0.521672	2.11209	2.83871	Heat transfer	Standard
88	HDKR	2007.csv	1.20724	1.78687	0.622117	1.48847	2.93699	Heat transfer	Standard
89	HDKR	2013.csv	0.786011	2.41605	0.425439	2.26349	2.35745	NOCT	Standard
90	Isotropic	2009.csv	0.962103	1.60101	0.465051	1.92158	3.05345	Heat transfer	None
91	Isotropic	2016.csv	1.18794	2.35605	0.545625	2.40389	3.91502	NOCT	Standard
92	Perez	2006.csv	1.0237	1.84347	0.598629	2.01581	2.28503	Heat transfer	None
93	HDKR	2012.csv	1.00126	1.83896	0.572208	2.11605	2.92719	Heat transfer	None
94	Perez	2007.csv	1.17846	2.13549	0.671208	1.79166	3.04312	NOCT	Thin film
95	Isotropic	2007.csv	0.798621	1.64301	0.556309	1.55267	3.10889	Heat transfer	None
96	Perez	2013.csv	0.757926	2.09223	0.447563	1.8597	3.09433	NOCT	Standard
97	Isotropic	2009.csv	0.825653	2.19597	0.457539	1.40595	2.53177	Heat transfer	None
98	Perez	2015.csv	0.776882	2.18223	0.431367	2.04279	3.21476	Heat transfer	Thin film
99	Isotropic	2007.csv	1.03595	1.68243	0.536022	2.03562	2.45849	NOCT	None
100	Isotropic	2016.csv	0.832596	2.48964	0.476941	2.23722	2.69705	Heat transfer	Standard